Design and modelling of the limaçon positive displacement gas expander

Truong H. Phung

Supervisor: Associate Professor Ibrahim A. K. Sultan

School of Engineering and Information Technology

Faculty of Science and Technology

Federation University Australia – Mount Helen Campus

University Drive, Mount Helen, Victoria 3350

A thesis submitted for the degree of

Doctor of Philosophy in Mechanical Engineering

Ballarat, Victoria, Australia 2017

Abstract

The limaçon positive displacement technology has been featured in a number of patents over the last 100 years. The technology offers a two-lobe rotor that slides and rotates in a rounded cavity so as to create a pair of variable-volume chambers suited for fluid processing. As such, it can be employed to manufacture gas expanders to extract work from low-grade heat or other heat resources. Positive displacement gas expanders are applied to small-scale power generation plants which can be used for a number of applications such as to improve the energy efficiency of existing thermal processes.

This thesis features work undertaken to develop models to inform and enhance the design process such that an optimised limaçon machine is produced. The models developed in the thesis efficiently predict and characterise the performance of the limaçon gas expander irrespective of the working fluid used or the phase transformation that takes place during the working of the expander. The models developed are multiphysics in nature as they incorporate the vibration analysis of the apex seals with the thermodynamical differential description of the working medium together with the dynamical characterisation of an electro-mechanical control valve fitted to regulate the amount of fluid allowed into the working chamber.

Chapter 1 starts with a problem statement that addresses the questions which the author aims to answer upon the completion of this project. The chapter offers a detailed background on the limaçon technology and where it falls in relation to other fluid processing machines. Chapter 1 is also a literature review which spans such aspects as:

- types of fluid processing machines investigated in literature,
- types of cycles that can be utilised for work extraction,
- the mechanisms that can be used to produce the limaçon motion and

- various two-phase flow models.

Chapter 2 presents the design process of a new limaçon machine embodiment proposed in this thesis and referred to as the limaçon-to-circular machine. In this chapter, the formulation of the rotor and housing profiles, the radial clearance, the rotor-housing interference, and the volumetric relations have been investigated. A constraint stochastic optimisation approach has been employed in order to produce optimum dimensions for a limaçon-to-circular machine based on certain geometric requirements and machine's working conditions specified by the designer.

Chapter 3 investigates the geometry and vibration of limaçon machine apex seals. The chapter sets out by defining the rotor modified apex geometry, apex seal dimension and geometry, location of the seal in the seal groove, and the relationship between the seal, groove, and machine housing. Then descriptions are given for the motion of apex seal relative to the grooves and the machine housing under the dynamic loading from the seal spring and various contact and pressures forces acting on the seal. The problem is nonlinear in nature and a dynamical multi-degree of freedom one which features complex motion patterns and intricate seal-surroundings interactions. Also in Chapter 3, the seal-groove relative positions have been categorised into cases based on the seal-groove back-contact and front-contact types. Case studies to verify the accuracy of the seal dynamic response model has been investigated and detailed in this chapter.

In Chapter 4, the thermodynamic performance of the limaçon-to-circular machine with the effect of apex seal dynamics and dynamic response of inlet valve has been investigated. This chapter presents a model to calculate the angular positions of the leading and trailing edges of the rotor, the cross-sectional areas of the working chambers, and the velocities of fluid flow through the inlet and discharge ports. The model can be slightly altered to account for different machine embodiments and different working

fluids used. The effect of the changing phase of working fluid on the performance of the limaçon machine has also been taken into account whereby the phase changes have been considered not only in the working chambers during the machine operation but also in relation to the flow through the inlet and discharge ports. The example presented at the end of Chapter 4 proves the validity of the proposed models and their suitability to describe and characterise the working of limaçon gas expanders.

Chapter 5 details the conclusions which this thesis work has produced and offers an insight into future research projects which have been flagged by the work presented in the thesis

Acknowledgement

Firstly, I would like to express my sincere gratitude to my supervisor, Associate Professor Dr Ibrahim A. K. Sultan, for his continuous support, patience, motivation, and immense knowledge. His invaluable guidance, comments, suggestions, and constructive criticisms have helped me in not only my research but also writing papers and this thesis. I could not have imagined having a better supervisor and mentor for my PhD journey.

I would also like to take the opportunity to thank my wife Tam T.M. Tran for her continued patience, understanding, and support throughout my research, writing this thesis and life in general.

Declaration of authorship

I, Truong H. Phung, declare that this thesis titled, “Design and modelling of the limaçon positive displacement gas expander” and the work presented in it is my own. I confirm that:

- This work was done wholly or mainly while in candidature for a research degree at Federation University Australia.
- Where any part of this thesis has previously been submitted for a degree or any other qualification at Federation University Australia or any other institution, this has been clearly stated.
- Where I have consulted the published work of others, this is always clearly attributed.
- Where I have quoted from the work of others, the source is always given. With the exception of such quotations, this thesis is entirely my own work.
- I have acknowledged all main sources of help.

Signed ..... Supervisor signed.....

Date ..... Date .....

Table of contents

List of figures

List of tables

Nomenclatures

CHP : Combined Heat and Power system

CHP-ORC : Combined heat and power system with organic Rankine cycle

ORC : Organic Rankin Cycle

TFC : Trilateral Flash Cycle or Triangle Flash Cycle or Triangle Cycle

SPSA : Simultaneous Perturbation Stochastic Optimisation

RPM : Revolution per minute

Chapter 1: Introduction*

The global drive of using energy more effectively and efficiently has fuelled the ever-increasing effort to obtain energy from low-grade heat resources by the research sector as well as the industry. Typically, in order to extract work from available heat resources, fluid processing machines (or expanders), which may include rotary or reciprocating embodiments, are utilised. However, for the specific case of work extracting applications from low-grade heat sources, positive displacement expanders are preferred due to their ability to operate at reasonably low speeds and handle relatively small mass flow rate (Lemort, Quoilin, Cuevas, & Lebrun, 2009).

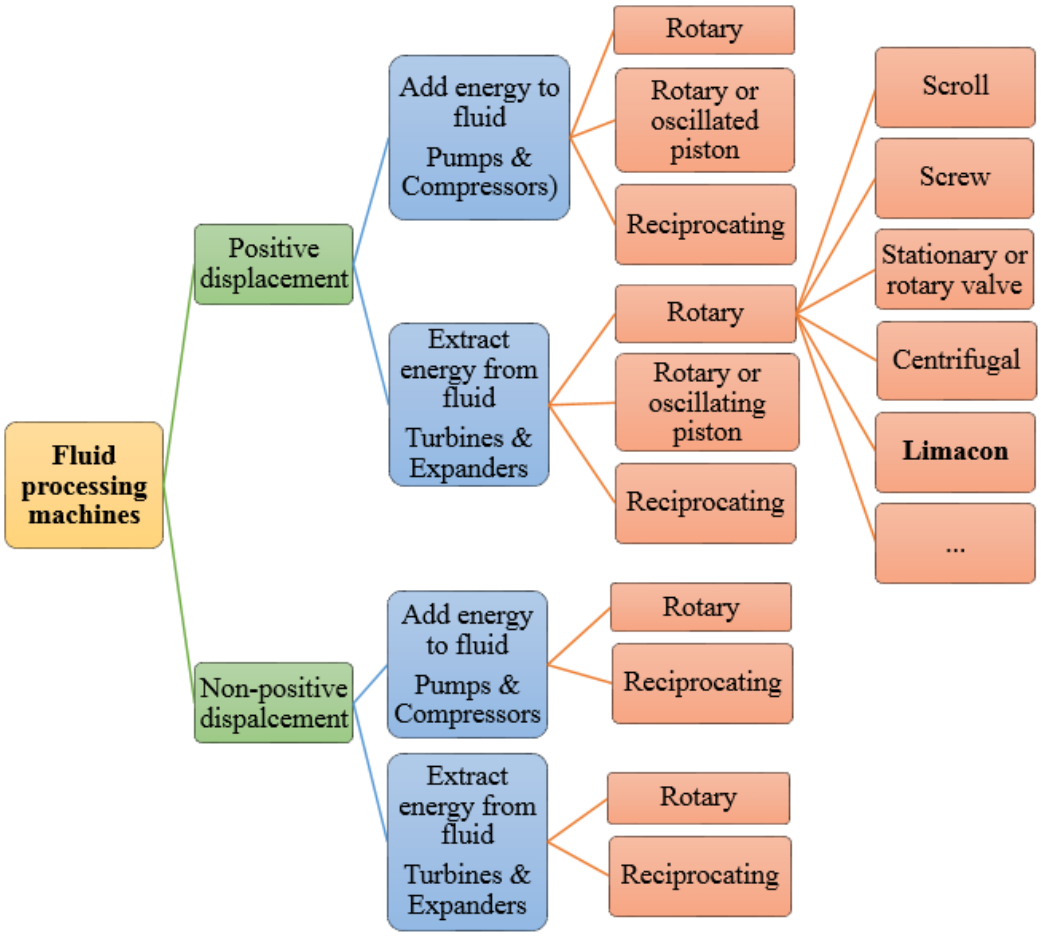

Figure 1-1: Fluid processing machines hierarchy

* Sections 1.3, 1.4, and 1.5 of this chapter have been published as a book chapter (Phung, Sultan, & Boretti, 2016)

The fluid processing machines can be divided into two main categories: positive displacement machines and turbomachines (also referred to as non-positive displacement machines); they may be categorised as volume type and velocity type fluid processing machines as well (Qiu, Liu, & Riffat, 2011). Within each of those two types, fluid processing machines are further divided into two sub-categories: one of which adds energy to the working fluids (i.e.: pumps and compressors) while the other extracts energy from the working fluids (i.e.: turbines and expanders). In each sub-category, those machines are further split into reciprocating and rotary branches. A fluid processing machinery hierarchy is depicted in Figure 1-1. Hence, it is obvious that the limaçon expanders and compressors investigated in this project belong to the rotary branch, nested under positive displacement machine type, which extracts energy from the working fluids.

One huge advantage of the positive displacement rotary machines over the reciprocating, oscillated piston and radial piston machines, Figure 1-3 and Figure 1-4, is that they have far less stationary and moving parts (Warren & Yang, 2013; Rose & Yang, 2014; Picard, Tian, & Nishino, 2015; Picard, Tian, & Nishino, 2015). This advantage makes them lightweight, less complex in terms of the number of components, and more compact in terms of physical size. Some examples of these rotary machines are the roots,

Figure 1-2: A root, a Wankel and a limaçon machine

Sources: powderbulksolids.com, cgproducts.net, and Sultan A. Ibrahim

Wankel machines, and limaçon machines, which are shown in Figure 1-2. Of particular note is the well-known Wankel rotary engine, which consists of much fewer parts than the conventional piston engine. However, the unique housing-rotor arrangement of this machine requires accurate and sophisticated manufacturing methods, and more complex side and apex sealing arrangements. Thus far, Mazda is the only company known to put this Wankel engine design to mass-production and utilise for passenger car manufacturing (Mazda Motor Corporation, 2014).

Figure 1-3: Axial (rotary) piston pump
Source: http://img.directindustry.com

Limaçon expanders, despite the weight and size advantages they offer over the other rotary designs, to a certain extent share the complexity in housing and rotor manufacturing as well as sealing arrangements with the Wankel engines. However, with the advancement of additive manufacturing, the development and fabricating of limaçon machines will be much simpler, more accurate, and more cost-efficient.

Figure 1-4: Radial engines
Source: sherline.com

The limaçon machine's housing and rotor are based on the limaçon curve (snail curve or limaçon of Pascal curve shown in Figure 1-5), which has the form of $r = b + a\cos\theta$ or $r = b + a\sin\theta$ in the polar coordinates (r, θ); the values of the limaçon parameters a and b determine the shape of the curve. The $r = b + a\cos\theta$ curve takes the x-axis as its mirror line, while the $r = b + a\sin\theta$ curve takes the y-axis as a mirror line. The profiles of the limaçon

housing and rotor can be defined by allowing a chord, p_1p_2, with length 2L, to rotate and slide on a so-called base circle of radius r, as shown in Figure 1-6.

The working fluid, which is used to expand and transfer work to the machine's shaft, can be in either of the following forms: gas, liquid, or two-phase (where liquid and gas phases coexist) (Sultan & Schaller, 2011). The same fluid will also be used in a closed cycle to carry heat from the boiler or evaporator to the expander to be processed.

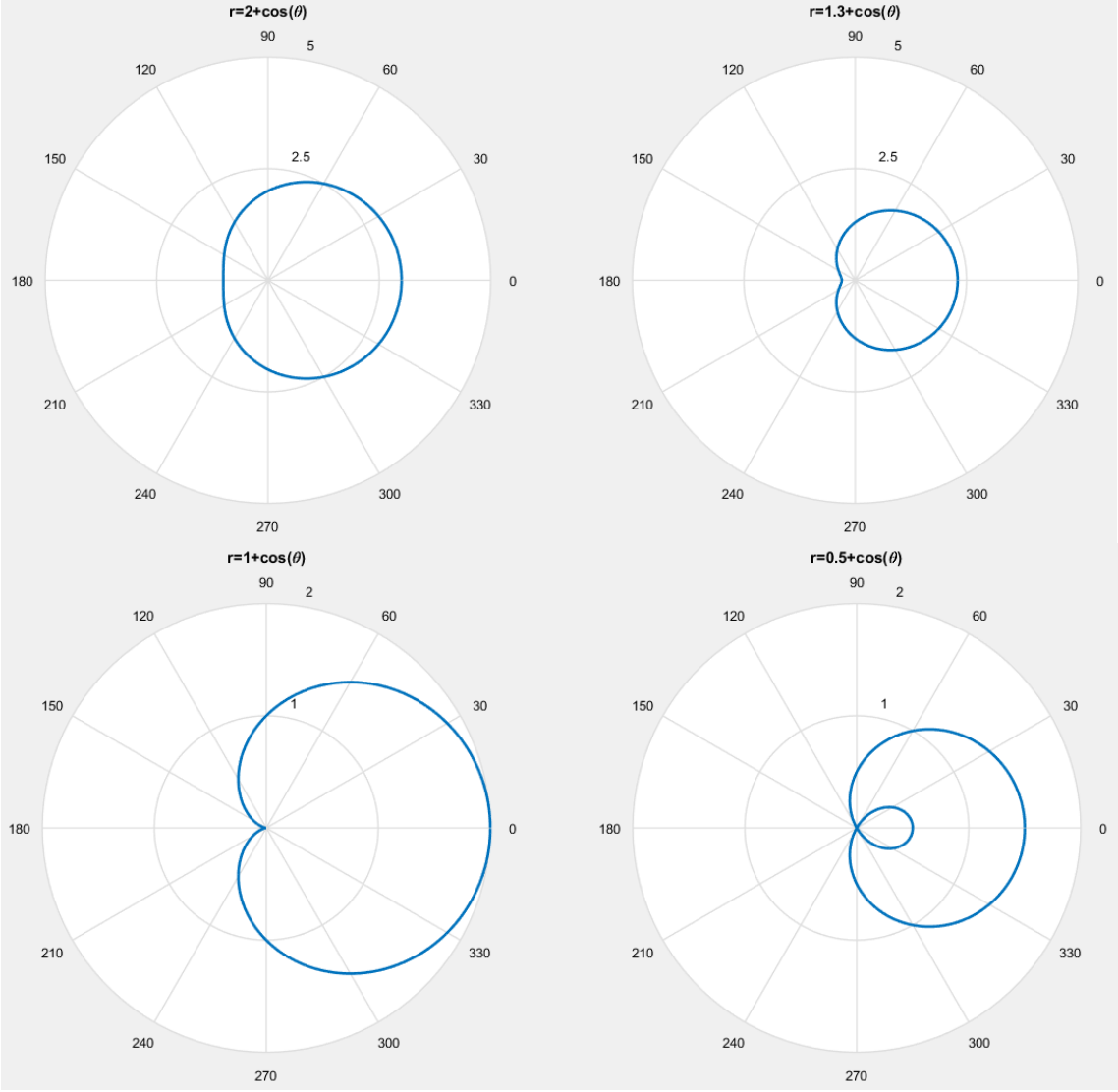

Figure 1-5: Limaçon curve family

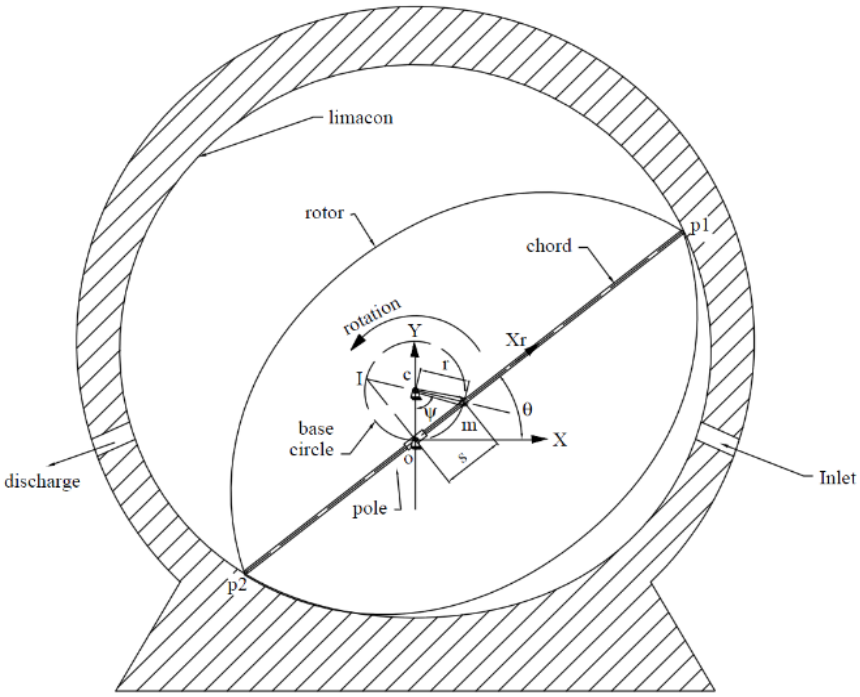

Figure 1-6: A limaçon machine
(Sultan, 2005)

1.1. Problem statement and research questions

The limaçon technology in comparison with other energy conversion technologies such as turbine, rotary, reciprocating piston, rotary piston, and rotary vane, is more compact in size, which can readily be designed to run at relatively low speed, and is capable of handling small mass flow rate. Additionally, the limaçon machines are capable of operating in two-phase flow conditions that can in fact damage non-positive displacement machines. Despite all the advantages offered by this technology, the unavailability of necessary manufacturing expertise to accurately machine the limaçon housing and rotor profiles had in the past deprived limaçon technology from gaining the publicity that it deserved. However, the global drive of using existing energy resources effectively and efficiently in conjunction with the rapid advancement of manufacturing technology will definitely boost industry and research interests in the limaçon technology.

This project is aimed to optimise the flow of single-phase and/or multiphase high-pressure working fluids through the inlet and outlet ports of limaçon expanders, the positions of the ports, the geometry of the ports, and the flow of fluids inside the expanding chamber. The work in this project will further investigate various embodiments of limaçon machines in terms of the mechanical characteristic and thermal dynamic performance. The effect of apex seal and its performance under dynamic load from the housing, seal spring, as well as the pressure difference from different machine's chambers will also be examined. The optimisation process will be applied in the context of small to medium scale power-generation-plants such as CHP (Combined Heat and Power) systems or waste-heat recovery systems. The micro power-generation-plants that utilise limaçon technology can significantly reduce the emission footprint to as close as zero when solar power is integrated. Such system not only can generate electricity for domestic use but also can provide hot water service as well as space heating. Additionally, such plants are capable of utilising low-grade thermal resources, which previously has been overlooked or disregarded. As suggested by the literatures (Chen, Goswami, & Stefanakos, 2010; Fukuta & Yanagisawa, 2009; Hung, Shai, & Wang, 1997; Lemort, Quoilin, Cuevas, & Lebrun, 2009; Lemort, Lebrun, & Quoilin, 2010; Persson, 1990; Sutan, 2012), the overall efficiency of those micro power-generation systems depends considerably on the performance of the expanders.

This project will attempt to answer the following questions:

- Is it possible to employ different rotor and/or housing profiles (i.e.: circular curve) while still maintaining the limaçon motion between the rotor and housing for different limaçon machines' embodiments?
- Is it possible to optimise the expanders' embodiments, geometries, porting, and manifolds to maximise the machine's overall efficiency?

- How will the apex seals, the seal-groove and seal-housing relative motion, and the seals' performance affect the overall efficiency of the limaçon machines?
- Will the incorporation of inlet valve affect the performance of limaçon machine?

1.2. Methodology and research goals

The key objective of this project is to develop a limaçon expander suitable and efficient enough to be built into CHP or waste-heat recovery systems to generate mechanical or electrical power. The limaçon expander extracts the power from the working fluid by allowing that fluid to go through an expansion process, which converts the internal energy of the working fluid into the motion of the rotor. With all that in mind, this project will be carried out in the following phases:

- Investigating different types of mechanisms that produce the limaçon motion
- Exploring different housing-rotor embodiments with the view of proposing a more practical, more efficient and easier to manufacture paradigm
- Investigate the apex seal motion and the effect of sealing on the machine performance
- Developing the geometric and thermodynamic model for the proposed paradigm and hence use this model for optimisation purposes. Consider the effect of inlet valve to the machine's thermodynamic performance
- Optimising the machine geometry and port angle and position for the best volumetric and thermodynamic performance

The outcome of the optimisation models in the above phases will depend on the working fluid properties as well as the inlet and outlet conditions.

1.3. Literature review

As has been mentioned above, the focus of this project is the limaçon technology, limaçon machines, and their applications especially in CHP and waste-heat recovery systems; therefore, the literature will also be mainly focused on these particular categories. In addition to that, various cycles that can utilise for power extracting, the optimisation procedure, and two-phase flow modelling will also play crucial roles and will be studied. Different types of gas expanders, other than limaçon, which have previously been and are currently being utilised in CHP or waste-heat recovery processes, together with their disadvantages, advantages, and efficiencies will be as well considered. This project aims to utilise the potentially higher efficiency and lower manufacturing cost of the limaçon expanders over other technologies in the power recovery practice.

1.3.1. Types of gas expanders and their roles in thermodynamic cycles

Over the years, various gas expander designs have been developed for power generation applications in general and waste-heat recovery in particular. In the context of this project, the focus is drawn towards the expanders which are more suitable for small-scale heat and power extracting applications such as: axial piston expanders, reciprocating piston expanders, rolling piston expanders, revolving vane expanders, screw expanders, scroll expanders, and limaçon expanders to name only a few. The chart shown in Figure 1-7 had been constructed by Persson (1990) to map out how various expander designs perform based on their shaft speed and flow capacity. The figure can be considered as a rough guide for the selection of expander type for further design and evaluation.

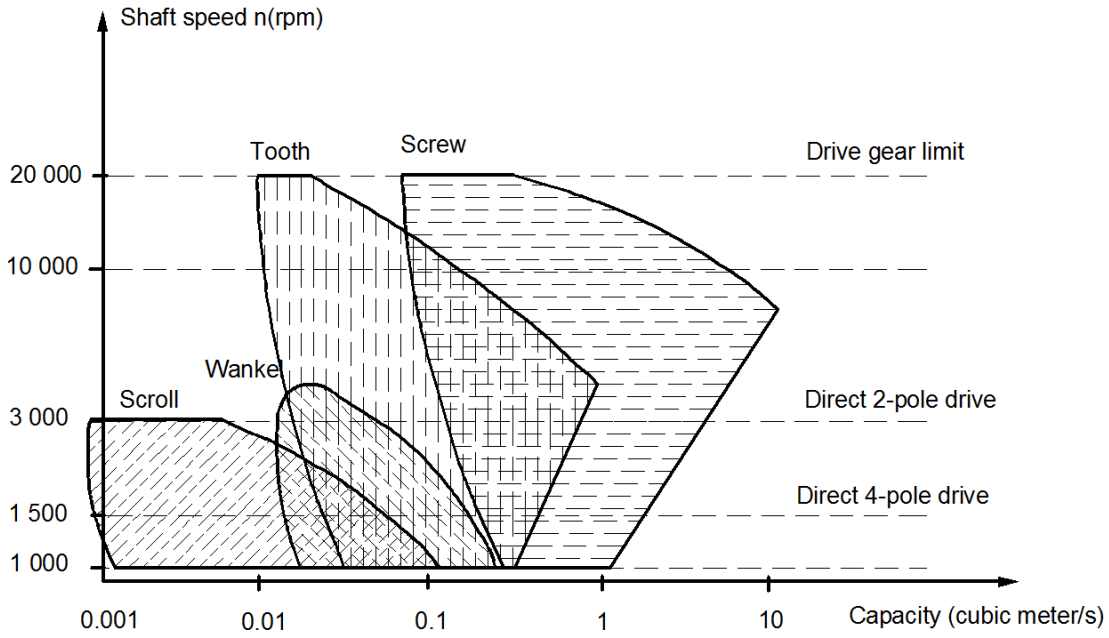

Figure 1-7: Example of a common performance map of different geometry concepts (Persson, 1990)

1.3.1.1. *Reciprocating piston expanders*

One of the most common type of expanders, which has been widely utilised, is the reciprocating piston machine; such a conventional design is featured in the crank-slider mechanism employed for car engines, and reciprocating compressors. Over the years, researchers from around the world have focused their attention on different geometric embodiments of the reciprocating piston machines. For instance, Gimstedt (1979), Glavatskaya et al. (2012) and Gridin et al. (1971) who have designed and evaluated single acting piston expanders, on the other hand, Zhang et al. (2007) have been interested in developing the double acting piston expanders. Those research along with much more published studies on the reciprocating technology can give us a sense of the popularity that this reciprocating piston technology has achieved. It has been claimed by the abovementioned authors that the expanders in this category can perform at a broad range of pressure ratios with an isentropic efficiency varies from 50 to 70% (62% in the case of double-acting piston expanders) and a volumetric efficiency ranges from 30 to 60%.

1.3.1.2. *Axial piston expanders*

Grip (2009), has offered a geometrically different variation to the reciprocating piston machine; the axial piston expander design, as shown in Figure 1-8, is claimed to be able to run on biofuel or solar resources and to have the potential to apply to low-temperature Rankine cycle plants. In this design, the traditional reciprocating engine has been rearranged so that the machines' pistons are spaced evenly around the crankshaft and parallel to the shaft axis; similar approach can also be found in the Duke engine, which is proposed by Duke (1997). The axial reciprocating piston expanders' output power, however, is limited to the power range below 1000 kW. Grip argues that although piston expanders suffer from higher mechanical losses, they tend to have lower leakage and high part-load efficiency; piston expanders are preferred in some particular applications due to their capability of operating at low speeds. The unique design of the axial piston machine offers a possibility to significantly reduce the lateral force between the piston and the cylinder liners compared to the conventional reciprocating piston engines. (Grip, 2009)

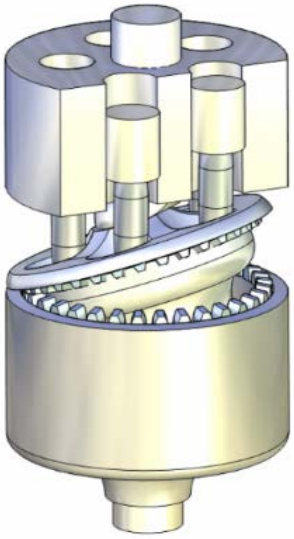

Figure 1-8: An axial piston expander (Grip, 2009)

1.3.1.3. *Rolling piston expanders*

The next type of expander is the rolling piston expander, which has been designed and analysed by Li et al. (2009); the authors have also claimed that this type of expander can replace the throttling valve in the CO_2 cycle of refrigeration and air-conditioning systems. The expander is used to recover power during the CO_2 expansion process, hence, improve the system efficiency. The output work or energy generated by the expander can

be fed back to the system as a second-stage compressor or utilised to drive other mechanisms, machines, or applications.

Zheng et al. (2013) have put much effort to carry out experiments in which a rolling piston expander has been utilised in a low-temperature organic Rankine cycle to generate electricity. The proposed expander, shown in Figure 1-9, can operate between 350 and 800 revolutions per minute (rpm) with a maximum power output of 0.35 kW and a maximum isentropic efficiency of 43.3% when the temperature of the heat source is below 90°C.

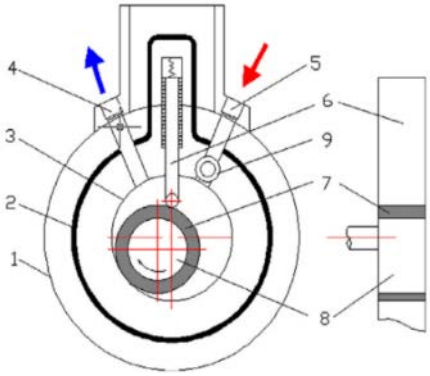

Figure 1-9: Structure of a rolling piston expander (Zeng et al., 2013).

1. Shell. 2. Sealing ring. 3. Cylinder. 4. Discharge port. 5. Inlet port. 6. Sliding vane. 7. Rolling piston. 8. Eccentric rotor. 9. Control valve.

1.3.1.4. *Rotary-vane and Revolving-vane expanders*

Amongst the potential expander concepts, the rotary-vane expanders have been developed and used for years in either waste-heat recovery or improving the process efficiency. Those expanders may include single-acting and double-acting expanders, which have inlet and outlet ports arranged symmetrically in the elliptical cylinder, the vane slots and vanes are located on the rotor, as shown in Figure 1-10. Rotary-vane expander received a significant amount of attention from researchers and manufacturers due to their simple structure and their simplicity in manufacturing compared to other types of expanders. The calculated volumetric and isentropic efficiencies of these machines vary from 20% to 70% and from 20% to 40%, respectively. With different operational

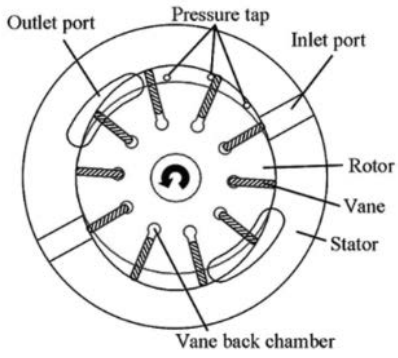

Figure 1-10: Sectional view of a double-acting rotary-vane expander (Fukuta et al., 2009).

speeds, gap clearance values, and eccentricity ratios, the experimental values of rotary-vane expanders have been reported to be as high as 70% for volumetric efficiency and as high as 37% for isentropic efficiency (Fukuta & Yanagisawa, 2009; Yang, Peng, Sun, Guo, & Xing, 2009; Yang, Peng, Sun, Guo, & Xing, 2009; Jia X. , Zhang, Yang, & Peng, 2009). Additionally, according to Jia et al. (2010), by introducing high-pressure gas into the vane slot, the isentropic efficiency of this machine may reach 45%.

Subiantoro and Ooi (2009; 2010) have reportedly designed and developed revolving vane (RV) expanders with an average power production of 650 W and mechanical efficiencies of 96.5% and 95.7% for RV-type I, and RV-type II respectively. Depicted in Figure 1-11 are the four variants of RV expanders, which have different allocations for the drive and driven components. With RV-type I and RV-type II, the rotors act as the drive components; while with RV-type Ia and RV-type IIa, the drive components are actually the machines' cylinders.

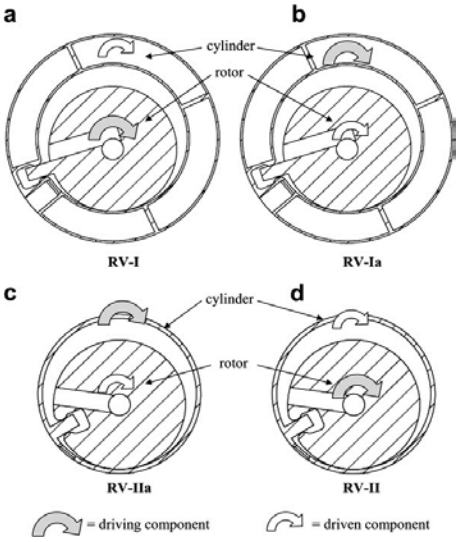

Figure 1-11: Four variants of revolving vane (RV) expanders (Subiantoro & Ooi, 2010)

1.3.1.5. *Screw and scroll expanders*

Screw expanders (helical rotor expanders), and scroll expanders, shown in Figure 1-12 and Figure 1-13, have been receiving considerable attention from researchers in the field of positive displacement machinery. Examples may be sought in the works of Wang, Wu, Ma, Liu, and Yu (2011), Tamura, Taniguchi, Sasaki, Yoshida, Sekiguchi, and Yokigawa

Figure 1-12: A screw expander (Smith, Stosic, & Kovacevic, 2005)

(1997), Bowman (United States Patent No. 4412796, 1983), and House (1976) who have designed and carried out experiments on both single and double screw expanders. Meanwhile, Wang, Peterson, and Herron (2009), Lemort, Quoilin, Cuevas, and Lebrun (2009), and Xiaojun, Liansheng, Yuanyang, and Pengcheng (2004) have put their thoughts to scroll expanders. In the aforementioned papers, the authors have theoretically and experimentally explored the performance of screw and scroll expanders in the Combined Heat and Power (CHP), micro-CHP, work-recovery, and waste-heat recovery systems.

Peterson, Wang, and Herron (2008), in their publication, have built and tested a small-scale regenerative cycle, which utilised moderate-grade heat source (150-400^{o}C). They experimented with a regenerative Rankine cycle using a scroll expander, which produced 256 W of gross power. The author argued that, despite the lower than expected efficiency, the project was successful as an exploratory study of using scroll expander in small power generation plants. The authors also revealed that the proposed scroll expander suffered from excessive leakage; in fact, leakage is known to be the major unresolved problem with all scroll expanders in particular and rotary machine in general. This leakage problem significantly affects the volumetric, thermal efficiencies, the quality of recovered work of these expanders. Such quality of recovered work and other performance parameters of the scroll expanders have been previously addressed by Xiaojun, Liansheng, Yuanyang, Pengcheng, and Shu (2004) in their paper.

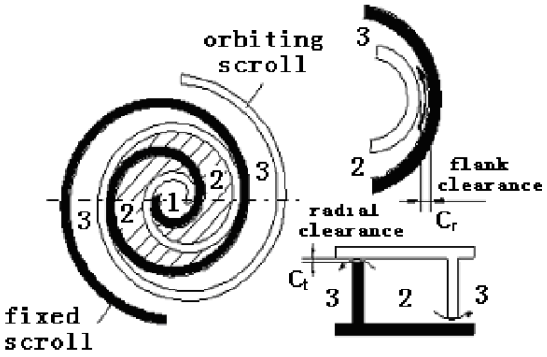

Figure 1-13: A scroll expander (Xiaojun, Liansheng, Yuanyang, & Pengcheng, 2004)

1.3.1.6. *Turboexpanders*

The turbomachines can be used as gas expanders in power extracting applications. This type of machine has also received much attention from researchers all over the world; specifically, Ghosh, Seshaiah, Sahoo, and Sarangi (2005) have developed a design procedure for the main components of turbo expanders for cryogenic applications. These components are turbine wheel, nozzle, diffuser, shaft, brake, compressor, and bearing. Additionally, Hou, Zhu, and Chen (2004) experimented with different types of foil bearings for the turbo expanders, while Kucerija (United States Patent No. 5003782, 1991) and McClure (United States Patent No. 2529880, 1950) have had their turbo expander designs patented. In general, turbo expanders have received substantial attention from researchers in low-grade heat recovery.

Further to the expander, the type of theoretical cycle employed in the power generating process may affect the power output delivered by the expander. In the next sections, different theoretical cycles will be explored.

1.3.2. The Rankine cycle

Firstly, it is essential to review the Carnot cycle before going to the details of Rankine cycle. The Carnot cycle is a theoretical and reversible thermodynamic cycle proposed by Nicolas Leonard Sadi Carnot nearly two centuries ago. This is the most efficient cycle; the concept of which can be based on to build systems that can convert thermal energy to work or power. In reality, however, Carnot cycle is considered impractical (Sun, Chen, Chen, & Wu, 1997; Cheng, 2000) due to its exceptionally slow isothermal heat transfer process.

The concept proposed by Carnot has been employed to develop more realistic power generation cycles, one of which is the Rankine cycle. A basic Rankine cycle is made up of four main components: a pump, a boiler or an evaporator, an expander, and a

condenser. Rankine cycle utilises a working fluid to transfer thermal energy from one component to the other and employs an expander to extract work from the working fluid. Fluids that belong to one of the three groups, wet fluids, dry fluids, and isentropic fluids, may be utilised in the medium-scale and large-scale Rankine cycles. With the case of micro Rankine cycle power plants, the power generation process can also make use of organic fluids (refrigerants or hydrocarbons, e.g.: R134a, R234a, R410a to name only a few); such plants are often referred to as “Organic Rankine Cycles power plant” (Tchanche, Pétrissans, & Papadakis, 2014).

There are two main types of Rankine cycles, which are readily available to put to use i.e.: single fluid Rankine cycle and binary fluids Rankine cycle. A single fluid Rankine cycle utilises only one working fluid in the work-extracting process; different fluid states determined by the amount of energy they contain - saturated, superheated, transcritical or supercritical - can be used. The state of the working fluid then determines the name of the particular Rankine cycle i.e.: superheated Rankine cycle, supercritical Rankine cycle. Single fluid Rankine cycles are often less complex and have fewer components than the binary cycles. The binary Rankine cycles, on the other hand, with the purpose of increasing the output efficiency, have been developed with more than one working fluid loops. The Maloney and Robertson cycle, the Kalina cycle, the Uehara cycle, and the Goswami cycle depicted in Figure 1-14 are some members of the binary Rankine cycle category (Tchanche, Pétrissans, & Papadakis, 2014).

A basic single fluid Rankine cycle with four stages of change depicted by a T-s diagram (temperature-entropy diagram) is shown in Figure 1-15. In stage 1-2, the working fluid in liquid form is pressurised and transferred to the boiler by a feed pump, this stage requires power supplied for the pump (work-in, W-in). Stage 2-3 takes place in a boiler

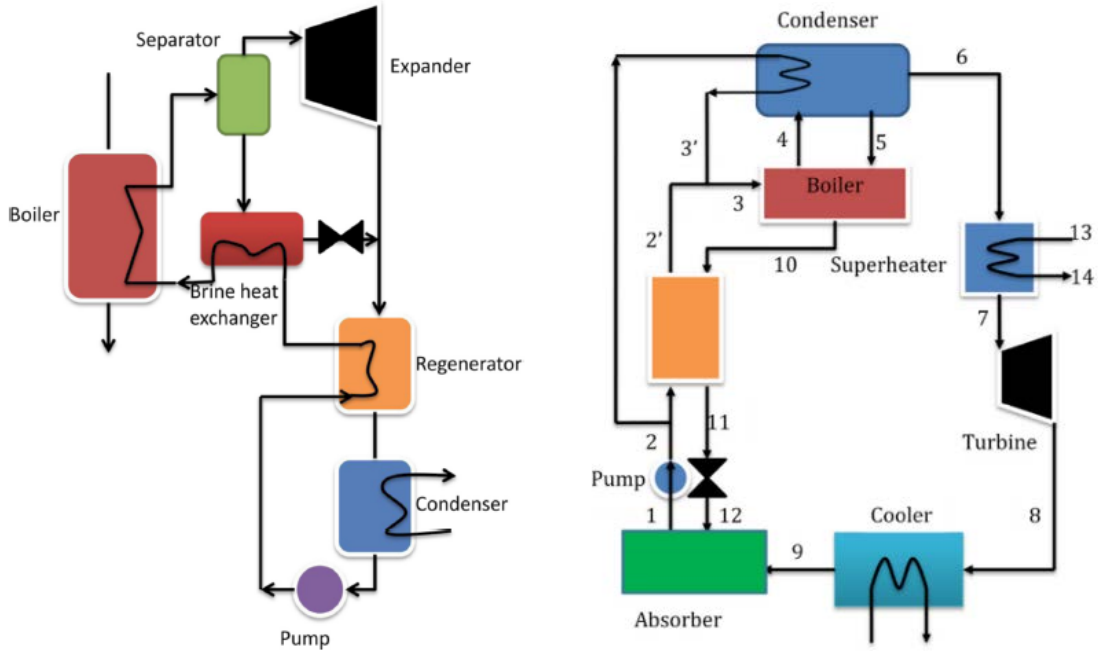

Figure 1-14: The Kalina and Goswami cycles (Tchanche, Pétrissans, & Papadakis, 2014)

(heat exchanger) or a series of boilers where heat is added to the working fluid to bring it to a higher energy stage (heat-in, Q-in). Then in stage 3-4, the fluid is expanded in an expander or a series of expanders. The expander helps converting the internal energy of the working fluid to mechanical work (work-out, W-out). Lastly, in stage 4-1, the excess heat is rejected (heat-out, Q-out) via the heat exchanger(s) to bring the fluid back to its liquid form. In this form, the fluid can easily be transported to the boiler again by the feed pump. The cycle then can be repeated to provide a continuous flow of work at the expander's shaft. The four-stage cycle is summarised as follows:

- 1-2: Liquid pressurised in a feed pump (W-in)
- 2-3: Continuous heat addition to the working fluid in a boiler or heat exchanger (Q-in)
- 3-4: Isentropic (constant entropy) expansion of the working fluid in an expander(s) (W-out)
- 4-1: Continuous heat rejection in a condenser (Q-out)

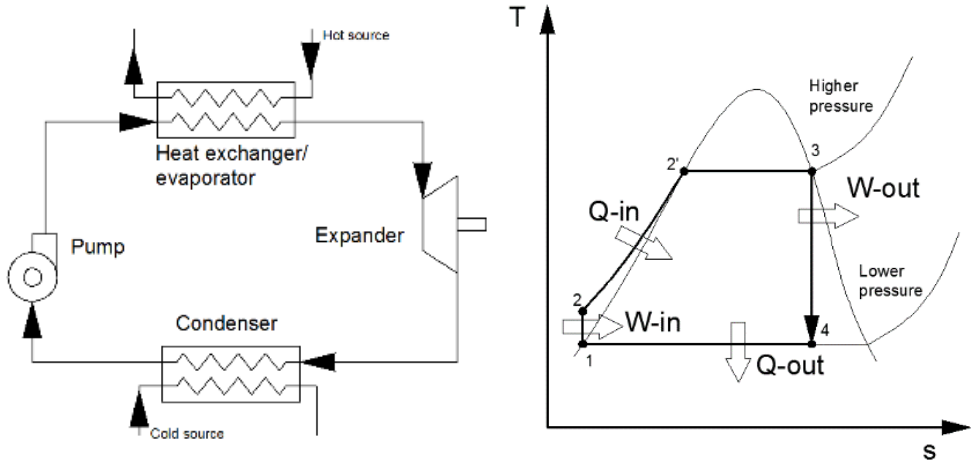

Figure 1-15: A basic Rankine cycle

Rankine cycle is employed in most of the current thermal power plants, which mainly burn fossil fuels to produce necessary heat; Rankine cycle-based plants can also make use of heat from other thermal energy resources such as biomass, biofuels, geothermal, solar thermal, and waste-heat. In recent years, the ever-increasing demand for renewable energy and efficient energy usage has become the main drive of research effort in improving the efficiency of existing power systems and utilising low-grade or waste heat. Hung, Shai, and Wand (1997), Gao, Liu, He, Xu, Wu, and Li (2012), Chen, Lundqvist, Johanson, and Platell (2006), Quoilin, Aumann, Grill, Schuster, Lemort, and Spliethoff (2011) are some of the researchers who have put much effort into waste-heat recovery systems with the applications of different types of expanders i.e.: scroll, screw, and rolling piston. (Tchanche, Pétrissans, & Papadakis, 2014; Guo, Du, Yang, & Yang, 2014; Hung, Shai, & Wang, 1997; Wang H. , et al., 2011; Gao, et al., 2012; Chen, Lundqvist, Johanson, & Platell, 2006; Quoilin, et al., 2011).

1.3.3. The Trilateral Flash Cycle

As described by Smith (1993), an ideal Trilateral Flash Cycle or Triangle Flash Cycle (TFC), which is a modification of the ideal Carnot cycle - composed of three processes, two of which are the same as the Carnot cycle namely the isentropic expansion to produce

work, and the isothermal heat rejection to the cooling medium. It is obvious that the ideal TFC would have a lower thermal efficiency compared to the ideal Carnot cycle using the same hot and cold reservoirs. DiPippo (2007) in a publication on thermal efficiency for geothermal binary plants has compared the efficiencies of a Carnot cycle with an ideal TFC and a practical TFC using the same hot source temperature of 150^{o}C. DiPippo (2007) also referred to some recent attempts to build machines that approach the ideal TFC and argued that the ideal TFC is unachievable. In fact, a more realistic and irreversible version of the TFC, depicted in Figure 1-16, should often be considered.

Steffen, Löffler, and Schaber (2013), Fischer (2011), and Zamfirescu and Dincer (2008) revealed that TFC is amongst the three processes known for the conversion of low-temperature and waste heat resources to energy: the ORC, the Kalina cycle and the TFC. With its ability to recover most of the heat from the heat source, the TFC can easily outperform the ORC and the Kalina cycle. Additionally, with purposefully selected inlet temperatures at various points of the plant, it has been proven that the exergy efficiency for power production of the TFC, which is the ratio of the net power output to the incoming exergy flow of the heat carrier, is from 14% to 20% higher than that of the ORC. In addition, the total efficiency of the TFC, which is the ratio of all the outgoing

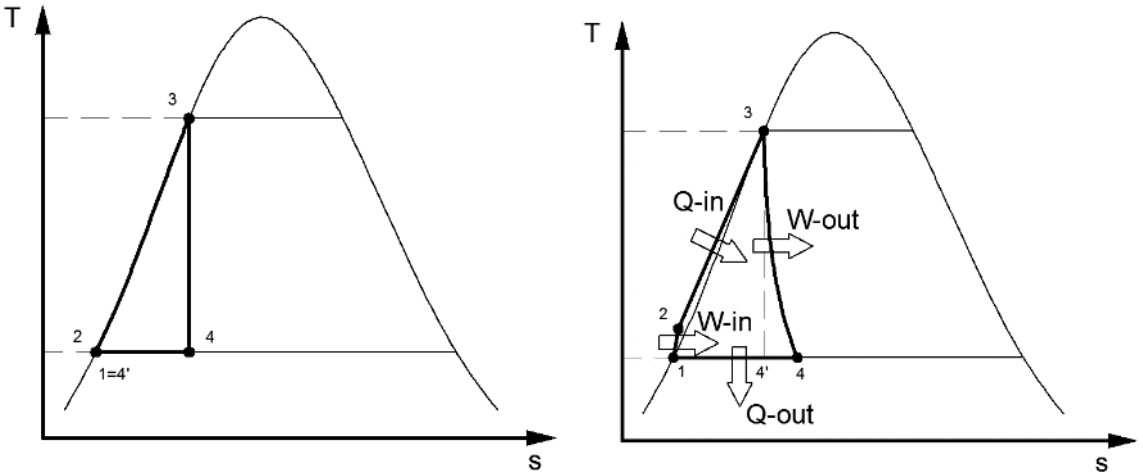

Figure 1-16: The ideal and practical Trilateral Flash Cycle (TFC)

exergy flows to all incoming exergy flows, is from 1% to 9% higher than the ORC's in most cases. Moreover, Zamfirescu et al. (2008) have demonstrated that with certain setups and at given temperatures the calculated exergy efficiency of the TFC could be twice as much of the ORC's. However, TFC is a rather new technology that will need further research and development (Zamfirescu & Dincer, 2008; Fischer, 2011; Steffen, Löffler, & Schaber, 2013).

1.3.4. Micro-CHP and CHP-ORC systems

According to Qiu, Liu, and Riffat (2011), expanders can be categorised as dynamic or velocity type, and displacement or volume type. Within these two main types, various designs with different output efficiency have covered a wide range of output power ranging from 1 kW to 50 kW, which falls within the realm of small-scale CHP systems. Additionally, Qiu et al. (2011) have also introduced and evaluated the performance of four different types of expanders such as turbine expander, screw expander, scroll expander, and air motors used as expanders for household applications.

In turbine expanders, the velocity of the working fluid in the vapour (gas) phase at high temperature and pressure drives the blades, which in turn drive the output shaft; the work can be used directly from the shaft or can be transformed to electrical power by the generators (alternators). Turbine type expanders are generally used when the output power greater than 50 kW is required. With the lower output power, turbine expander is less preferred because the efficiency of such expander deteriorates gradually with the decrease of output power, and an unacceptably low efficiency reached at the output power of 10 kW. Additionally, small size turbines are costly to make which prevents them from being utilised in small-scale power generation plants. (Qiu, Liu, & Riffat, 2011).

Another choice of expanders for small-scale organic Rankine cycle CHP systems is the screw expander; this type of expander utilises the meshing of a male and one or more

female rotors. As the rotors rotate, the volume trapped between the rotors and the machine housing or casing changes, high-pressure working fluid is allowed to enter the space between the rotors and casing on one end and discharge through the other. During the process, the working fluid expands and transfers its energy to the rotors of the expander. However, screw expanders are not widely used due to the difficulty in sealing the working fluid within the expanding chamber (Qiu, Liu, & Riffat, 2011).

CHP-ORC systems using scroll expanders have been successfully simulated and experimented by Lemort & Quoilin et al. (2009; 2010), and Wang et al. (2010). Wang et al. (2010) revealed that the efficiency of a scroll based ORC system, which uses R134a as a working fluid may exceed 70% over a wide range of rotor speeds and expansion ratios. Additionally, the CHP-ORC systems, which use scroll expander, are suitable for the output power range of 0.1 to 1 kW.

Vane type expanders can also be employed for CHP-ORC as has been featured in the work of Aoun (2008) who has reported an isentropic efficiency of 80% at 800rpm using refrigerant R11 as working fluid. On the other hand, the corresponding efficiency figures reported for the vane expanders vary from 50-55% within a speed range of 800 to 850 rpm. However, the efficiency figure reported by Aoun does not agree with the well-known fact that vane type expanders suffer from serious leakage problem. This problem has been highlighted by the comment of Qiu et al. (2011) that the rotational speed of a vane expander considerably influences the pressure and flow rate limit of the working fluid.

Interestingly, R11 and R113, which were employed for experimental evaluation of expanders as reported in many publications, have been phased out by the Montreal protocol (United Nation Environment Programme, 1987) as gases that deplete the ozone layer.

1.4. Limaçon of Pascal curve and Limaçon expanders

1.4.1. The limaçon curve from a mechanical point of view

With the recent development of manufacturing and the advancement in the 3D (three-dimensional) printing technology, the fabrication of the limaçon housing and rotor has never been more feasible. As previously mentioned, the polar coordinates form of the limaçon curve can be described as follows:

$$r = b + a\cos\theta \quad [1\text{-}1]$$

or

$$r = b + a\sin\theta \quad [1\text{-}2]$$

Such formulas in the polar coordinate can be transformed to the Cartesian coordinates by applying the two following equations:

$$\begin{cases} x = r\cos\theta \\ y = r\sin\theta \end{cases} \quad [1\text{-}3]$$

When the machine is in motion, the rotor chord, p_1p_2, rotates and slides about the pole, o; the housing limaçon is formed by the traces of the apex, p_1 (or p_2). Two coordinates XY and X_rY_r are attached to the housing and rotor respectively; The XY frame stays stationary with the housing while the X_rY_r frame rotates with the rotor chord, p_1p_2. The distance from the centre point, m, of the chord, p_1p_2, to the pole, o, is called the sliding distance, s, which is formulated as follows:

$$s = 2r\sin\theta \quad [1\text{-}4]$$

where r is the radius of limaçon base circle; θ represents the angle rotated by the chord, p_1p_2, measured in the right-hand sense from the X-axis to the X_r-axis. The radial distance,

R_h, of the housing measured from the pole, o, to the apex along the chord, p_1p_2, can be expressed as:

$$R_h = 2r \sin\theta + L$$

[1-5]

where L is half of the rotor chord length or half of the distance between p_1 and p_2 (as shown in Figure 1-6 earlier in this document). Applying [1-3] to [1-5], the machine housing can be expressed as:

$$\begin{cases} x_h = r \sin 2\theta + L \cos\theta \\ y_h = r - r \cos 2\theta + L \sin\theta \end{cases}$$

[1-6]

or

$$\begin{cases} x_h = L[b \sin 2\theta + \cos\theta] \\ y_h = L[b(1 - \cos 2\theta) + \sin\theta] \end{cases}$$

[1-7]

where $b = \frac{r}{L}$ is the limaçon aspect ratio. The value of b has to be less than 0.25 in order to ensure that the limaçon profile is dimple and loop-free. A number of limaçon machine embodiments have been proposed since Wheildon (1896) was awarded a patent on a novel rotary engine design. Despite the fact that these embodiments employ different mechanical drives (mechanisms), they all follow the same kinematical constrains imposed by the equations [1-4], [1-5], [1-6], and [1-7]. As such, they all feature the similar profiles for the rotor and for the housing, and exhibit the same volumetric and thermodynamic characteristics. However, these embodiments can be differentiated in terms of their distinctive mechanical characteristics such as durability, dynamic force and vibration, manufacturability as well as ease of maintenance.

1.4.2. The port area calculation

To calculate the port areas for the limaçon machine, Sultan and Schaller (2011) have proposed a concept in which the two vectors R_l and R_t are used to define the port leading and trailing edges, respectively (Figure 1-17).

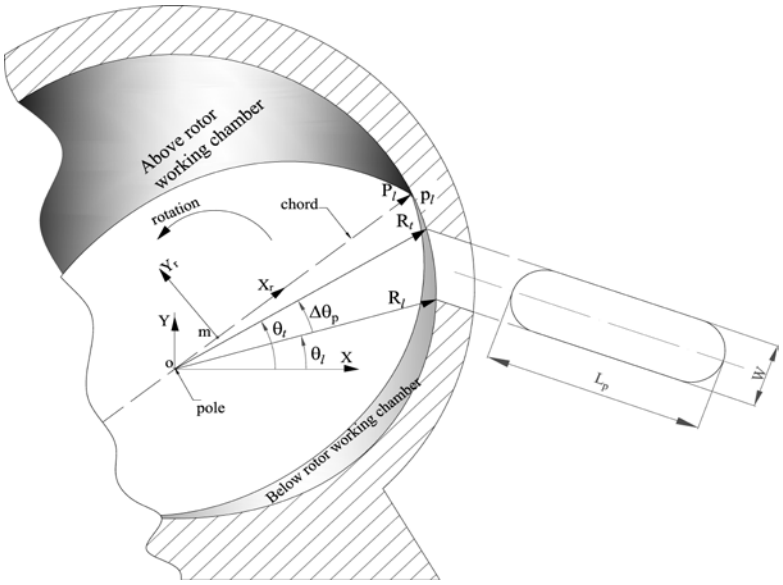

Figure 1-17: Ports geometric particulars (Sultan & Schaller, 2011)

This concept can be applied to both inlet and discharge ports. The port edges vector can be defined as:

$$R_l = L(2b\sin\theta_l + 1)\hat{R}_l \quad and \quad R_t = L(2b\sin\theta_t + 1)\hat{R}_t \qquad [1\text{-}8]$$

where θ_l and $\theta_t = \theta_l + \Delta\theta_p$ are the angular locations of the leading and trailing edges,

$\hat{R}_l = \begin{bmatrix}\cos\theta_l \\ \sin\theta_l \\ 0\end{bmatrix}$, and $\hat{R}_t = \begin{bmatrix}\cos\theta_t \\ \sin\theta_t \\ 0\end{bmatrix}$ are unit vectors directed from the pole, o, to the leading and trailing edges, respectively

The port length, L_p, constrained by the rotor depth, H; the port width, W, can be calculated from the two edge vectors as follow:

$$W = |R_t - R_l|$$

[1-9]

If the ports take the semi-circular shape, as shown in Figure 1-7, the port area, A_f, can be calculated as:

$$A_f = L_p W - W^2\left(1 - \frac{\pi}{4}\right)$$

[1-10]

The relationship between the rotor apices and the port edges can be represented by the two leading and trailing vectors $\mathbf{P}_l$ and $\mathbf{P}_t$ as follows:

$$\boldsymbol{P}_l = L(2b\sin\theta + 1)\widehat{\boldsymbol{X}}_r \quad and \quad \boldsymbol{P}_t = L(2b\sin\theta - 1)\widehat{\boldsymbol{X}}_r$$

[1-11]

Hence, the relative locations between the rotor leading-apex with the port edges can be defined by the two scalar quantities s_l and s_t as follows:

$$s_l = \left(\widehat{\boldsymbol{R}}_l \times \widehat{\boldsymbol{X}}_r\right) \cdot \left(\widehat{\boldsymbol{X}}_r \times \widehat{\boldsymbol{Y}}_r\right) \quad and \quad s_t = \left(\widehat{\boldsymbol{R}}_t \times \widehat{\boldsymbol{X}}_r\right) \cdot \left(\widehat{\boldsymbol{X}}_r \times \widehat{\boldsymbol{Y}}_r\right)$$

[1-12]

where the unit vectors of the X_rY_r frame $\widehat{\boldsymbol{X}}_r$ and $\widehat{\boldsymbol{Y}}_r$ are given as:

$$\widehat{\boldsymbol{X}}_r = \begin{bmatrix}\cos\theta \\ \sin\theta \\ 0\end{bmatrix} \quad and \quad \widehat{\boldsymbol{Y}}_r = \begin{bmatrix}-\sin\theta \\ \cos\theta \\ 0\end{bmatrix}$$

[1-13]

Therefore, Sultan and Schaller (2011) suggest that the instantaneous value of the port area, A_p, can be determined by:

$$for\ s_l \geq 0 \begin{cases} if\ s_t \geq 0 \Rightarrow A_p = A_f \\ if\ s_t < 0 \Rightarrow A_p = \left(\frac{W_l}{W}\right) A_f \end{cases}$$

[1-14]

and $$for\ s_l < 0 \begin{cases} if\ s_t \leq 0 \Rightarrow A_p = 0 \\ if\ s_t > 0 \Rightarrow A_p = \left(\frac{W_t}{W}\right) A_f \end{cases}$$ [1-15]

where the leading-edge width and the trailing edge width are expressed as $W_l = |\boldsymbol{P}_l - \boldsymbol{R}_l|$, and $W_t = |\boldsymbol{P}_t - \boldsymbol{R}_t|$ respectively.

1.4.3. The limaçon mechanisms

This section will feature a number of mechanisms, which have been proposed by designers to produce the limaçon motion and create the profile suitable for fluid processing. In every design mentioned below, it is important to identify the elements of the mechanism, namely:

- the rotor chord, which is the centre line of the rotor or the line that connects the two rotor apices
- the chord centre point, m
- the limaçon base circle
- the pole, o
- the instantaneous centre, I.

The pole, o, and the centre point, m, should always stay attached to the base circle so that the chord rotates at half of the angular velocity of the centre point, m, about the base circle centre. The instantaneous centre, I, should also fall on the base circle and is diametrically opposite to the centre point, m. (Sultan, 2005)

1.4.3.1. *The cam-assisted limaçon mechanism*

The cam-assisted limaçon mechanism depicted in Figure 1-18 has first been introduced by Wheildon (1896). In this concept, the lateral axis of the rotor is attached to the drive shaft at the pole, o. The two flat-face cam followers are perpendicularly attached

to the chord and allowed to slide on a stationary circular cam. During motion, the centre point, m, stays on the base circle; the diameter of which is the distance between the centre of the stationary circular cam and the chord centre, m, when the chord is at its lowest horizontal position. As previously mentioned, the instantaneous centre of the mechanism will always fall on the base circle at a point which is diametrically opposite to the chord centre, m. (Sultan, 2005)

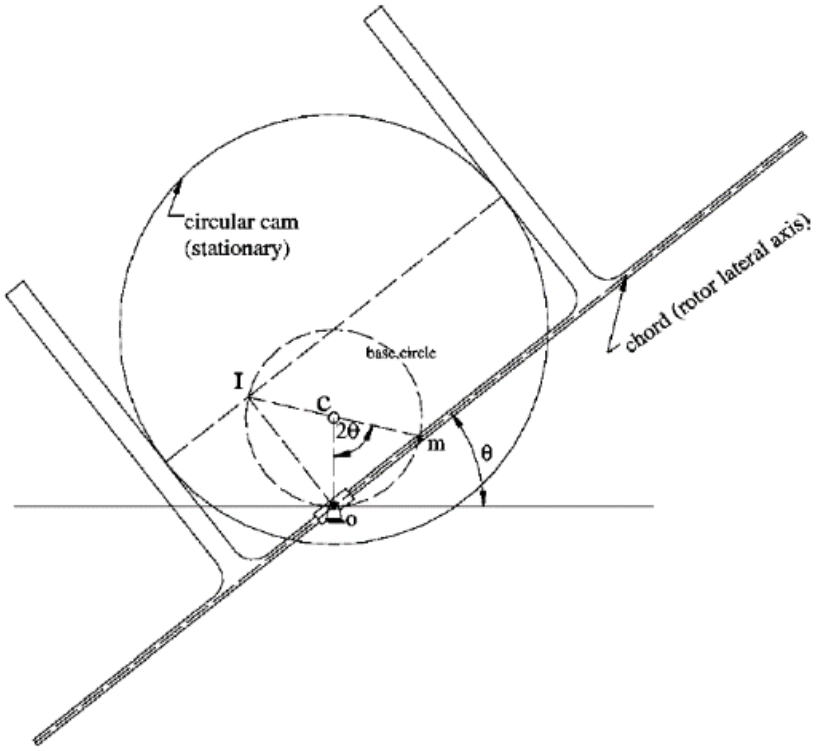

Figure 1-18: The cam-assisted limaçon mechanism (Sultan, 2005)

1.4.3.2. *The double slider limaçon mechanism*

Figure 1-19 represents a double slider mechanism proposed by Feyens (1927), and Frager and Menard (1954). Originally, Planche (1920) introduced a similar mechanism in which round pins are utilised instead of the sliders. The double slider mechanism will certainly produce limaçon motion as the pole, o, and the chord centre, m, would always remain attached to the base circle. The diameter of the base circle is equal to the distance

between the two slider pivots; and the drive or driven shaft is connected to the slider at the pole, o. This mechanism is also able to produce two compression-expansion cycles per shaft revolution. (Sultan, 2005)

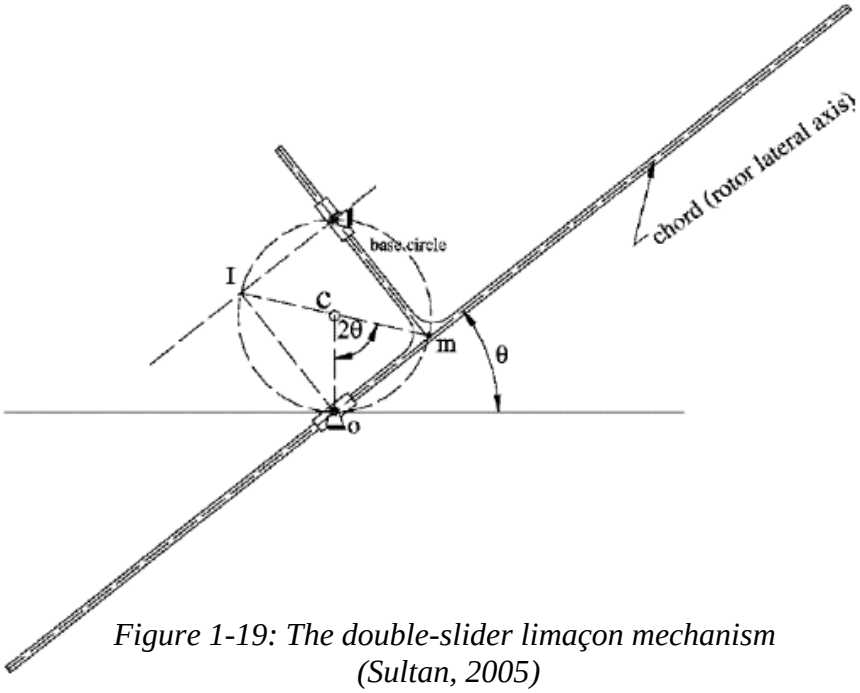

Figure 1-19: The double-slider limaçon mechanism (Sultan, 2005)

1.4.3.3. *The epicycloidal gear system*

Planche (1920) proposed a mechanism, shown in Figure 1-20, which employed an epicycloidal gear system to produce the limaçon motion for fluid processing applications. The epicycloidal gear train utilised by Planche consists of a stationary gear and a ring gear of a diameter doubles that of the stationary gear. A crank is used to connect the centre of the ring gear to the centre of the driveshaft to ensure that the angular velocity of the chord is half that of the driveshaft. Obviously, the base circle of this system is the pitch circle of the stationary gear. Although this mechanism produces the desired limaçon motion, the constraints imposed by the combined effects of the aspect ratio $\left(b = \frac{r}{L} \leq 0.25\right)$ and the mechanical nature of gear design are likely to reflect themselves on the overall machine dimensions. Consequently, the limaçon machine made of

epicycloidal gear mechanism will be bulkier compared to the limaçon machines that employ other mechanisms. (Sultan, 2005)

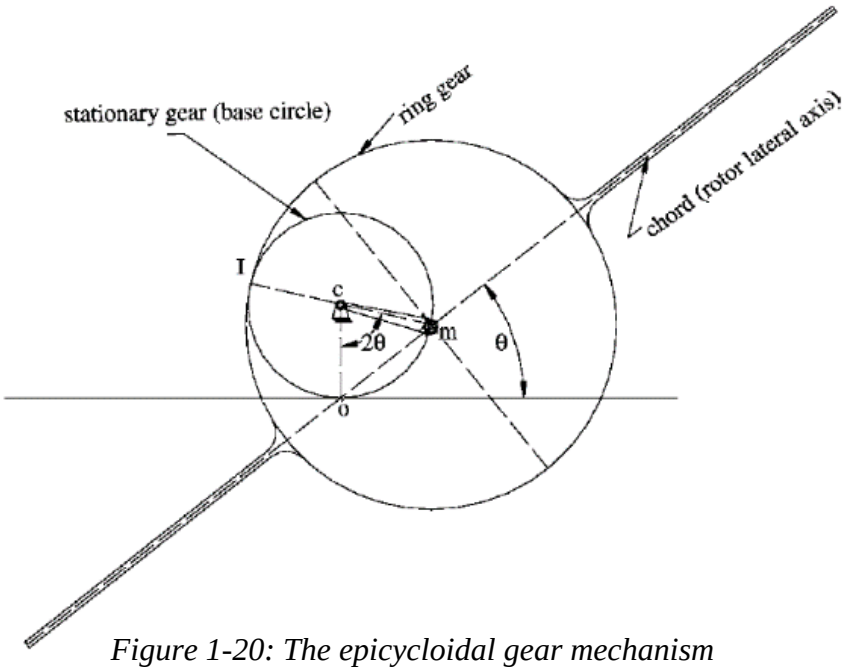

Figure 1-20: The epicycloidal gear mechanism (Sultan, 2005)

1.4.4. Comparison between limaçon mechanisms

Each of the above-mentioned mechanism has its advantages and disadvantages. As for the case of the cam-assisted and the double slider mechanisms (United States Patent No. 553086, 1896; US Patent No. 1340625, 1920; US Patent No. 1802887, 1931; US Patent No. 3029741, 1954), both can produce two compression-expansion cycles every revolution of the drive shaft. Due to the nature of their sliding motion, however, these two mechanisms are likely to produce a considerable amount of heat and hence, require sophisticated bearing and lubrication design, which may influence their mechanical efficiency. Not to mention that the cam-assisted and the double slider mechanisms have to be manufactured to high levels of accuracy to ensure the roundness, parallelism, and/or perpendicularity between different components. The epicycloidal-gear mechanism of Planche (US Patent No. 1340625, 1920), on the other hand, employed the rolling motion to its design to accomplish much better mechanical efficiency and simplicity.

Nevertheless, the epicycloidal-gear mechanism can only produce one compression-expansion cycle per driveshaft revolution. Table 1-1 presents the comparison between those abovementioned limaçon mechanisms.

Table 1-1: Pros and cons of different limaçon mechanisms

	The cam-assisted mechanism	The double-slider mechanism	The epicycloidal gear
Pros	- Can perform two compression-expansion strokes per shaft revolution (2:1). - Higher volume flow rate.	- Can perform two compression-expansion strokes per shaft revolution (2:1). - Higher volume flow rate	- Utilised rolling motion, hence better mechanical efficiency. - Can utilise the technology developed for the Wankel engine.
Cons	- Produce a significant amount of heat due to the use of sling motion on flat surfaces. - Has to be manufactured to relatively high accuracy levels.	- Produce heat due to sliding motion on flat surfaces. Mechanical efficiency can be increased by introducing proper bearing and lubrication design. - Has to be manufactured to high accuracy levels	- Can only produce one compression-expansion stroke per shaft revolution (1:1). - Lower volume flow rate

1.4.5. Works on limaçon technology and limaçon gas expanders

Despite the fact that limaçon technology has been developed over a century ago i.e.: the rotary engine by Wheildon (United States Patent No. 553086, 1896), it has not received the attention it deserved either from the research community or from industry. Recently, however, Sultan has drawn attention to this technology by developing the mathematical and design models to describe the working of such machines (2005, 2006, 2008 & 2011). Sultan also argued that the unavailability of the necessary technology to manufacture accurate limaçon housing and rotor profile had held back the progress in this area. Sultan has published various papers on limaçon-to-limaçon and circolimaçon machines, while Phung and Sultan have investigated the limaçon-to-circular machines and submitted a paper for publication (Phung & Sultan).

1.5. Two-phase working-fluid flow modelling

In two-phase flow, the interaction between different phases of working fluids such as mixing, evaporating and condensation makes it complicated to calculate the fluid properties. Those interactions are the reasons for a "semi-empirical" approach, which uses the simplified models in accordance with the correlations between phases, to be adopted. There are three basic models for two-phase fluid flow: the homogeneous model, the separated flow model, and the flow pattern model. The homogeneous model is the simplest method to use although its accuracy is limited; to get a more accurate solution, the separated flow model can be employed; however, the calculation process may be complicated due to the semi-empirical nature of the solution. The flow pattern model is the most recent approach to solving two-phase flow problems and its accuracy is gradually being refined (Fairhurst, 1983).

1.5.1. Homogenous model

According to Fairhurst (1983), the homogeneous model assumes that the two-phase fluid can be represented by a single–phase fluid with its properties derived from those of the two-phase following the below assumptions:

- Equal flow velocities for liquid and gas phases
- Thermodynamic equilibrium has been established between the phases.

Hence, with the homogeneous model, the properties of the two-phase fluid can be represented as follows:

$$\frac{1}{\rho_h} = \frac{x}{\rho_g} + \frac{1-x}{\rho_l} \quad [1\text{-}16]$$

and

$$\frac{1}{\mu_h} = \frac{x}{\mu_g} + \frac{1-x}{\mu_l} \quad [1\text{-}17]$$

and $$u_h = u_l = u_g = \frac{\dot{m}}{A\rho_h}$$ [1-18]

where ρ_h, ρ_g, and ρ_l are densities of the homogenous model, density of the gas phase, and density of the liquid phase respectively.

μ_h, μ_g, and μ_l are viscosities of the homogenous model, viscosity of the gas phase, and viscosity of the liquid phase respectively.

u_h, u_g, and u_l are velocities of the homogenous model, velocity of the gas phase, velocity of the liquid phase respectively.

$\dot{m}$ is the working fluid mass flow rate

x is the dryness fraction

A is the flow cross-section area

(Fairhurst, 1983; Shin, Iwata, & Ikohagi, 2003; Wang, Wang, & Chen, 2001).

The friction factor of the two-phase flow can be obtained by substituting the homogeneous fluid properties to a Moody diagram such as one given in Figure 1-21. Alternatively, Haaland formula, $\frac{1}{\sqrt{f}} = -1.8\log\left(\left(\frac{\epsilon}{3.7D}\right)^{1.11} + \frac{6.9}{Re}\right)$, can be used to calculate friction factor, f, explicitly; or Colebrooke equation, $\frac{1}{\sqrt{f}} = -2.0\log\left(\frac{\epsilon}{3.7D} + \frac{2.51}{Re\sqrt{f}}\right)$, can be utilised to find friction factor, implicitly (Cengel & Ghajar, 2011; Munson, Rothmayer, Okiishi, & Huebsch, 2013). In those two equations, $f, \epsilon, D, and\ Re$ are respectively the friction factor, surface roughness, diameter, and Reynolds number.

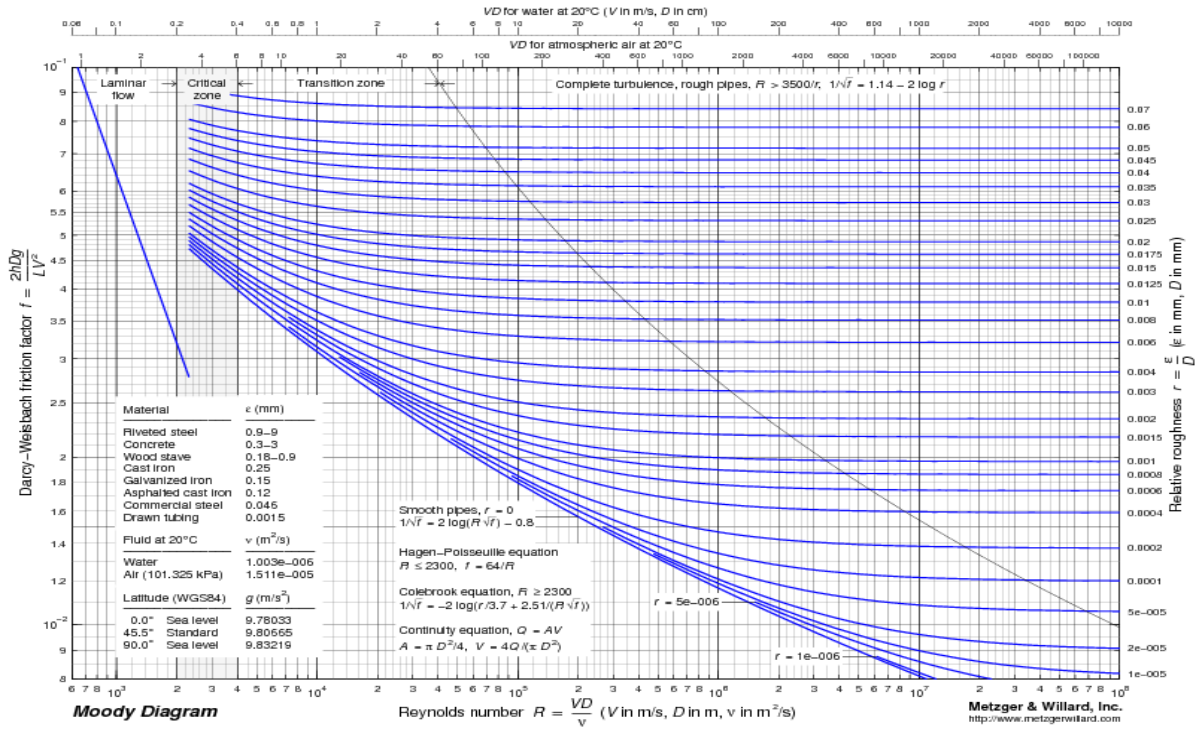

Figure 1-21: Moody chart
(Davis, 2008)

1.5.2. The separated flow model

The separated flow model assumes that the two phases are separated and each one is governed by its own set of equations, which correspond to its phase; Fairhurst (1983) in his paper mentioned that it is crucial to have "a knowledge of the frictional interactions between the phases and the flow cross-section occupied by each phase". With this model, the observed information is usually employed to determine the two-phase quantities at the regions of interest. Such quantities are otherwise not easily measured and usually unknown. The separated flow model also assumes that the thermodynamic equilibrium is achieved between phases and each phase has a constant velocity. Hence, the total flow is the flow of the liquid phase. The two-phase frictional gradient may be expressed in terms of the calculated single-phase gradient multiplied by a two-phase multiplier (Fairhurst, 1983; Lockhart & Martinelli, 1949; G.Iaccarino, A.Ooi, P.A.Durbin, & M.Behnia, 2003; Banerjee & Chan, 1980).

1.5.3. The flow pattern model

The flow pattern model assumes that the two-phase flow exists in one of the several configurations for which the basic equations of fluid mechanics can be solved. With this method, the knowledge of a particular flow regime must be obtained by visual observation or some other sophisticated technique (Fairhurst, 1983; Kawahara, Chung, & Kawaji, 2002; McQuillan & Whalley, 1985).

Chapter 2: Geometry of the rotary limaçon machines*

2.1. Introduction

Belongs to the rotary machine category, the limaçon machine shares the advantage of having less component and better power to weight ratio compared to other types of machines (Amrouche, Erickson, Park, & Varnhagen, 2014; Picard, Tian, & Nishino, 2015; Picard, Tian, & Nishino, 2015). In addition, limaçon machine is the positive displacement type, which can handle relative small mass flow and operate in both single and two-phase flow conditions.

Limaçon-to-limaçon and circolimaçon are the two current embodiments, which have been developed and investigated in terms of design, geometric optimisation, and thermodynamic performance by Sultan (2006; 2006; 2007). The housing of the limaçon-to-limaçon machine is manufactured to the limaçon curve; the rotor lobes are constructed of sections of the limaçon curves that are mirrored image of each other about the rotor chord. With the case of the circolimaçon machine, both the housing and rotor are manufactured to the circular curve. This chapter will present a new limaçon machine design. The new embodiment is referred to as the limaçon-to-circular machine in which the limaçon housing profile still takes the limaçon curve while the rotor lobes take the circular shape.

In the following sections of this chapter, the background of the limaçon machines, and the geometries, constructions, workings as well as the performance of limaçon-to-limaçon, circolimaçon, and the limaçon-to-circular machines will be presented. The focus

* Section 2.4 of this chapter has been submitted to Journal of Mechanical Design (ASME) for publication

will be drawn towards the new design limaçon-to-circular machine in the very last section of this chapter.

2.2. Limaçon-to-limaçon machines

As aforementioned, both housing and rotor of the limaçon-to-limaçon machine are manufactured to the limaçon curve. Sultan (2006) has utilised the mechanism shown in Figure 2-1 to generate such a curve. The mechanism consists of a chord, p_1p_2, whose length is $2L$, and a pole, o, on and about which the chord is allowed to slide and rotate. The midpoint of the chord, m, divides the chord into two equal sections of length L and m stays kinematically attached to a limaçon base circle of radius r and centre point c. The pole, o, is the lowest point of the base circle along the Y axis as shown in Figure 2-1.

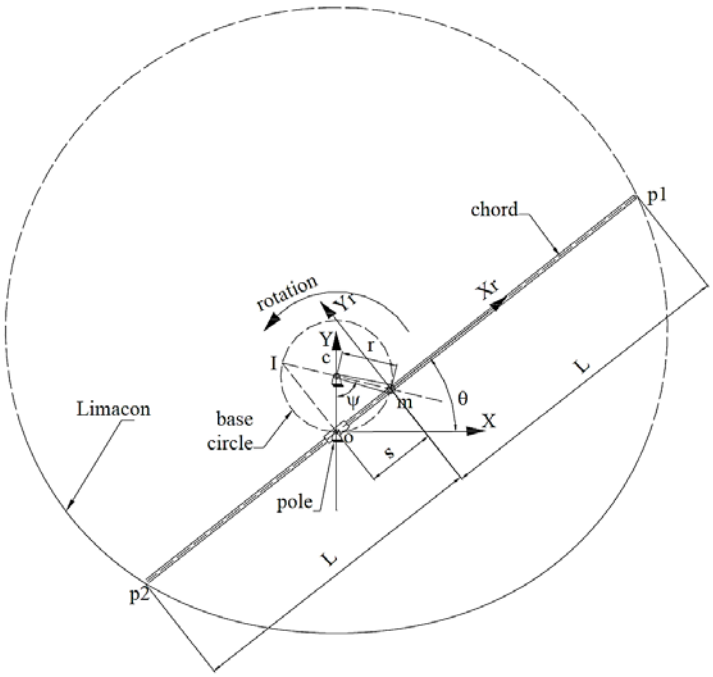

Figure 2-1: A limaçon mechanism
(Sultan, 2006)

As the chord performs its motion, the limaçon curve can be constructed by the traces of point p_1 (or p_2). During the chord motion, the sliding distance, s, between the pole, o, and the midpoint, m, changes with the angle, θ, rotated by the chord. The angle θ is

measured between the X and X_r directions in a right-hand sense. Hence, the sliding distance, s, on the rotor chord can be expressed as a function of θ as follows:

$$s = 2rsin\,\theta \tag{2-1}$$

in which r is the radius of the limaçon base circle.

Subsequently, the radial distance of the limaçon housing, R_h, can be formulated as follows:

$$R_h = 2r\sin\theta + L \tag{2-2}$$

The radial distance, R_h, can also be expressed in the Cartesian coordinates as follows:

$$\begin{cases} x = r\sin 2\theta + L\cos\theta \\ y = r - r\cos 2\theta + L\sin\theta \end{cases} \tag{2-3}$$

The machine rotor has a two-lobe construction, each lobe is the mirrored image of the other about the rotor chord. The rotor lobe is also manufactured to the limacon curve; the same method of curve formation as the machine housing is employed. In order to ensure smooth running condition and prevent housing-rotor interference, the length of the rotor chord is reduced by a small clearance value, C. As such, the rotor profile can be formulated as below:

$$R_r = 2r_r\sin\theta_r + (L - C) \tag{2-4}$$

where θ_r varies from π to 2π. The rotor radial distance, R_r, is measured from the midpoint, m, which is also referred to as the moving pole or the pole of the moving frame. The formulation of R_r can also be written in the Cartesian coordinate as:

$$\begin{cases} x_r = r_r \sin 2\theta_r + (L - C)\cos\theta_r \\ y_r = r_r - r_r \cos 2\theta_r + (L - C)\sin\theta_r \end{cases}$$

[2-5]

One important aspect that prevents the limacon curve from having loops and dimples is the aspect ratio, b. The value of b is defined as the ratio between the radius of the limacon base circle, r, and the half rotor chord length, L; such a value has to be below 0.25 $\left(b = \frac{r}{L} < 0.25\right)$. (Sultan, 2006)

2.3. Circolimaçon machines

Sultan (2008) pointed out that the cost incurred and the technology required to accurately manufacture housings and rotors for the limaçon-to-limaçon machines might go beyond the means of some manufacturers. Moreover, for the applications and systems that require small and low-efficient machines, the hefty price tag may be difficult to absorb. Hence, Sultan (2008) has introduced a modification of the limaçon-to-limaçon machine, which is referred to as the circolimaçon machine. The profile of the housing and rotor of the circolimaçon machine are circular curves instead of limaçon curves while the relative motion between the machine rotor and housing still follows the limaçon motion.

Sultan (2008) has proposed a design for the circular housing and rotor as shown in Figure 2-2. Similar to the limaçon-to-limaçon machine, the limaçon curve is traced by the apices p_1 or p_2, however, the substitute housing design of radius R_h and centre C_h are as follows:

$$R_h^2 = Z^2 + (L - C + s + d)^2 - 2Z(L - C + s + d)\cos\psi$$

[2-6]

where the centre C_h is made to fall on the Y-axis a distance Z, as shown in Figure 2-2. The distance, $d = -L + C + L\sqrt{1 + 4b^2 \sin^2\theta}$, represents the gap between the original

limaçon housing and it substituted circular housing. The value of d is measured along the X_r-axis from the rotor apex p_1 to the corresponding point on the substituted housing P_h.

The machine rotor lobes take the circular shape of radius $R_r = \sqrt{4k^2r^2 + (L-C)^2}$ and centre C_r. The centre C_r is set to be a distance $2rk$ from the moving pole, m, where the value of k is to be determined by the equation $k = a\left(1 - \frac{C}{L}\right)$ with $a > 1$. The equation to determine the machine rotor can also be expressed in terms of $C, L, a,$ and b as follows:

$$R_r = L\left(1 - \frac{C}{L}\right)\sqrt{1 + 4b^2a^2}$$

[2-7]

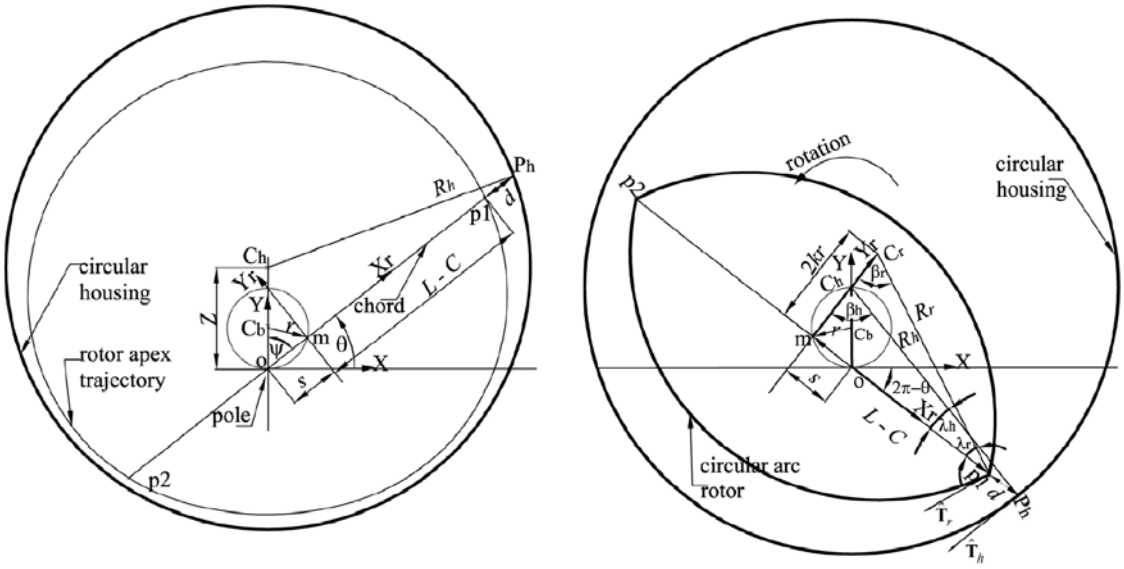

Figure 2-2: The design of the circular housing and rotor
(Sultan, 2006)

In order to justify between cost and manufacturing complexity, a new embodiment of the limacon machine has been proposed. This embodiment is referred to as the limacon-to-circular machine. In the next sections, the mathematical model and geometric aspects of this new design will be presented in details.

2.4. Geometric design of the limaçon-to-circular fluid processing machines*

2.4.1. Abstract

A limaçon machine is a rotary positive displacement device, in which the housing and rotor are constructed of limaçon curves. Previous works have been published to investigate the working of these machines in two embodiments: gas expanders and compressors. This paper presents a theoretical investigation into the potential of modifying the rotor of the limaçon machines to simplify manufacture and reduce production cost. The proposed modification will produce new characteristic for the rotor-housing interaction. An outcome, which motivates the need to obtain new mathematical models to investigate the rotor-housing interference, and describe the volumetric relationships of the new machine.

This paper sets out by introducing a background on the limaçon technology in a simple yet adequate fashion. Rotor-housing inference has been discussed from two different mathematical standpoints. The paper then introduces the volumetric relationship for the proposed modified machine and combines all the models produced in an optimisation endeavour to design the best machine for a given set of operating conditions. Case studies of different fluid processing applications are considered in order to demonstrate the soundness of the proposed modification and models. The outcome of this study confirms the validity of the proposed modification and its potential to produce a limaçon machine with favourable characteristics.

Keywords: Rotary machine, Limaçon-to-circular; limaçon machine; limaçon motion; pump; expander; compressor; positive displacement; SPSA.

Article Type: Research paper.

* This section has been submitted to Journal of Mechanical Design (ASME) for publication

2.4.2. Introduction

Positive displacement machines, especially rotary type, are increasingly gaining attention from energy-efficient, energy-aware, sustainable development organisations as well as from industry and the research sector. Such machines can utilise low-grade thermal energy sources, operate at relatively low speed, and have the capability of handling small mass flow rate. Additionally, positive displacement machines are able to operate in multiphase flow conditions, which can damage non-positive displacement machines. With all the above-mentioned benefits and the advantage of having the fewest components compared to other classes of machines, positive displacement machines can be manufactured to suit compact power generation systems at relatively low cost.

Over the years, different types of rotary positive displacement machines - which include compressors, expanders, and pumps - have been developed and tested. Examples of these are: scroll expanders and compressors by Kim et al. (2011), Oralli et al. (2011) and Georges et al. (2013); vane expander by Jia et al. (2009); revolving vane expander by Subiantoro et al. (2009), and limaçon machines by Sultan et al. (2005, 2006, 2008, 2011) to name only a few. Among those diverse types, limaçon technology seems to receive the least in-depth focus from researchers despite the fact that it is a technology, which has been developed over a century ago (United States Patent No. 553086, 1896). Recently, Sultan (2006 & 2008) has drawn the attention to the limaçon technology by developing mathematical and geometric models to describe their workings. Sultan (2008) argued that the unavailability of the technology needed to machine accurate limaçon rotor and housing had previously inhibited the progress in this area.

Manufacturing technology has now progressed to a point where it is possible to manufacture products with complex geometry albeit at a cost. Hence, Sultan (2008) proposed a modification of the machine housing and rotor profile in which limaçon curves

are replaced by circular ones to reduce the manufacturing cost. With the "circolimaçon" design, the distance separating the rotor apices from the housing varied with the rotor's angular positions. This variation reduces the effectiveness of the apex seals and adversely influences the machine performance. In fact, the apex-housing gap variation results from replacing the limaçon housing by a circular housing, the rotor circular flanks do not contribute to this gap. This understanding motivated the work presented in this paper that aims at maintaining the circular rotor profile while reverting the housing profile back to

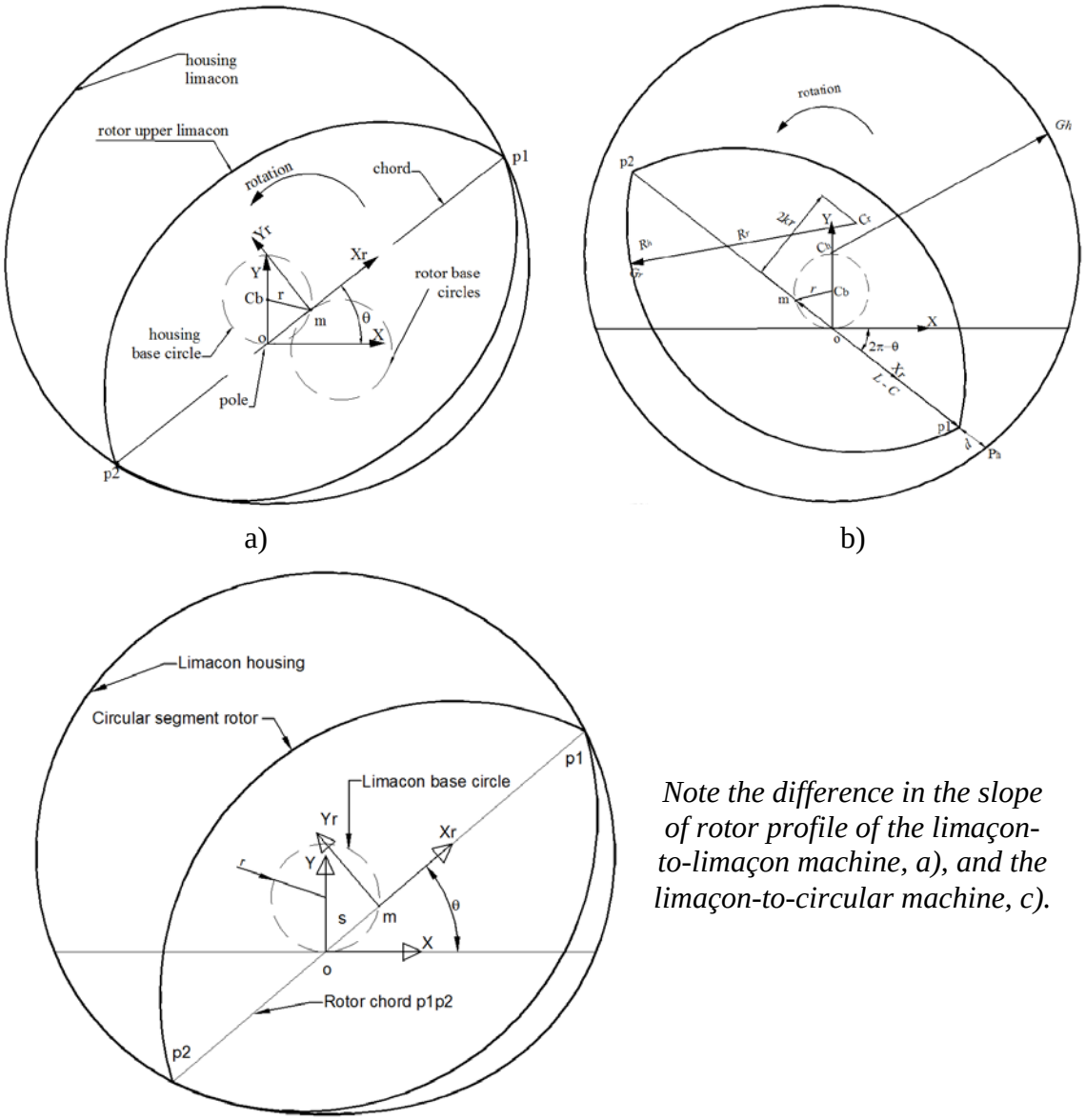

Note the difference in the slope of rotor profile of the limaçon-to-limaçon machine, a), and the limaçon-to-circular machine, c).

Figure 2-3: a) Limaçon-to-limaçon machine, b) Circolimaçon machine, and c) Limaçon-to-circular machine

its limaçon original. Thus, maintaining the favourable sealing characteristic of the limaçon-to-limaçon machine while reducing the cost of manufacturing the rotor flanks. With this concept in mind, this paper attempts to study the new proposed arrangement with the aim of eliminating rotor-housing interference and determining the volumetric characteristic in relation to various machine dimensions and the rotor angular arrangements. The difference between the three machine embodiments is shown in Figure 2-3.

2.4.3. Background on limaçon technology

Limaçon motion can be produced by a class of mechanisms as described by Sultan (2005) who also presented a number of positive displacement machines driven by these mechanisms. In further publications, Sultan suggested that both the rotor and the housing of these machines could be manufactured of either limaçon curves or circular ones, referred to as limaçon-to-limaçon and circolimaçon machines respectively (Sultan,

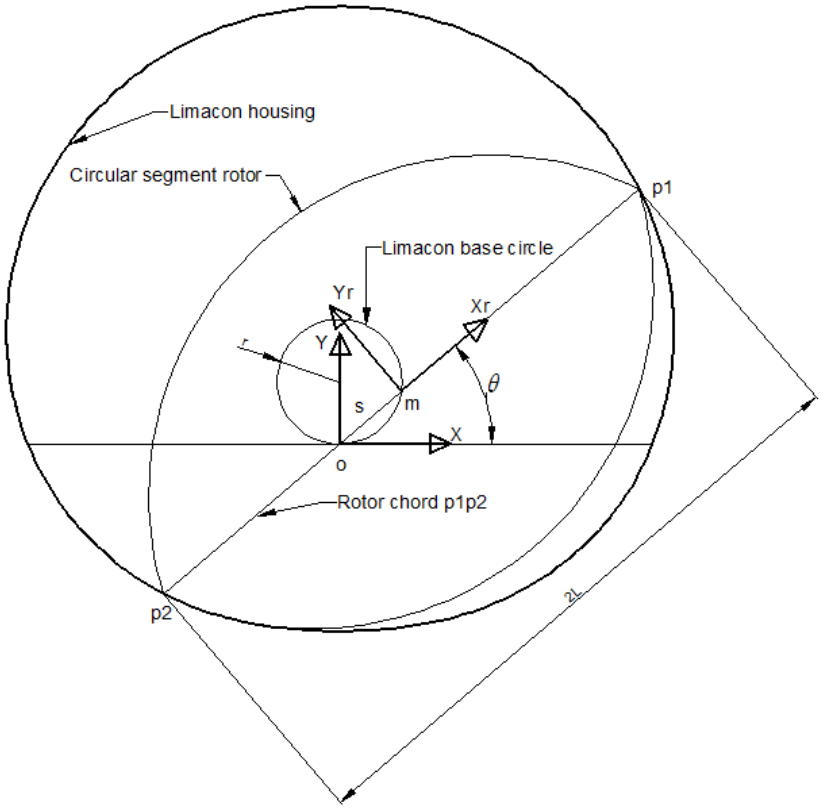

Figure 2-4: Limaçon-to-circular machine arrangement

2006; Sultan, 2008). In this paper, the rotor of the limaçon machine is modified in a way that instead of using the same limaçon profile as the housing, circular segments are utilised in order to achieve favourable thermodynamic induction of saturated liquid suitable for the Trilateral Flash Cycle (TFC) (Fischer, 2011; Steffen, Löffler, & Schaber, 2013).

As shown in Figure 2-4, the chord p_1p_2 of length 2L rotates and slides about the limaçon pole *o*, the housing of limaçon machine is a curve formed by the traces of point p_1 (or p_2). The centre point *m* of the chord p_1p_2 is restricted to move on a stationary circle of radius *r*, this circle be referred to as the base circle of limaçon. Two coordinate systems XY and X_rY_r are introduced; XY is a stationary Cartesian frame attached to the pole *o*, while X_rY_r is attached to the chord p_1p_2 at it centre point *m* and rotates and slides with the chord. The angle $\theta \in [0, 2\pi]$ measured from X to X_r axis is the angle rotated by the chord p_1p_2 as the rotor performs its rotational motion. When the chord is sliding, its centre point *m* slides a distance *s* measured from the pole *o* to the centre of chord m as shown in Figure 2-4, this distance can be written as follows:

$$s = 2r \sin\theta \qquad [2\text{-}8]$$

where *r* is the radius of the limaçon base circle. The radial distance of the housing, R_h, is measured along the chord p_1p_2 from the pole *o* to p_1 when the chord is in motion. This distance can be stated as follow:

$$R_h = 2r\,sin\,\theta + L \qquad [2\text{-}9]$$

Hence, the Cartesian position of point p_1 with respect to the XY coordinate can be expressed as:

$$x = R_h \cos\theta$$

and $$y = R_h \sin\theta$$

[2-10]

Costa et al. (1998) have mentioned that in order for the limaçon curve to be looping and dimple free, the value of limaçon aspect ratio $b = \frac{r}{L}$ has to be less than 0.25. This limit will be employed in this limaçon-to-circular machine. As such, equations [2-10] can be manipulated so that position of point *p1* can be expressed as functions of variables *b* and *L* (the half chord length):

$$x = L(b\sin 2\theta + \cos\theta)$$

and $$y = L[b(1 - \cos 2\theta) + \sin\theta]$$

[2-11]

The limaçon housing of the machine proposed in this paper can be manufactured following the equations [2-11]; the machine rotor consists of two circular segments of radius R, which take the chord, p_1p_2, as the mirror line. The designer can introduce a small clearance, C, between the housing and the rotor to prevent housing-rotor interference; this has been suggested by Sultan (2006). Therefore, half the rotor length, L_r, can be introduced as:

$$L_r = L - C$$

[2-12]

where C has to be calculated using a suitable optimisation procedure.

The housing of the fluid processing machine can be manufactured using equations [2-8], [2-9], [2-10], and [2-11]. The rotor is comprised of a circular segment with a radius $R = \sqrt{(L-C)^2 + (2rk)^2}$ mirrored about the rotor axis X_r. The length of rotor chord is defined in equation [2-12]; and the distance from the centre of the lower circular segment to the rotor chord is $2rk$, where k is a factor employed to facilitate the design process as

detailed below. This is a major change in terms of housing-rotor arrangement. The motion of the rotor itself inside the limaçon housing nevertheless follows the limaçon curve (rotating and sliding motion). In order for the housing-rotor interference not to take place during the rotational motion, design procedures should be incorporated such as the tangent approach and the radial clearance approach used by Sultan (2006).

The procedure proposed in this paper to design limaçon-to-circular machine by applying the tangent approach and the radial clearance approach will be detailed below.

2.4.4. Housing-rotor interference: the tangent method

It is essential for the design of the limaçon-to-circular machine to employ a procedure that can prevent housing-rotor interference while the machine is operating. The tangent method is simple enough to be initially applied. This approach considers the slopes of tangent vectors on the rotor at the apices and the corresponding contact points on the housing. As per Sultan (2006), the lower part of the limaçon housing where $\theta \in [\pi, 2\pi]$ and the corresponding lower lobe of the rotor are subject to housing-rotor interference. Figure 2-5 indicates the unit vector $\hat{T}_r$ tangent to the lower lobe of rotor at the apex p_1 and the corresponding unit vector $\hat{T}_h$ tangent to the housing. The condition for interference to be prevented can be defined as:

$$\left(\hat{T}_r \wedge \hat{T}_h\right).\hat{z} > 0 \qquad [2\text{-}13]$$

which can also be written in terms of the two angles ρ_h and ρ_r shown in Figure 2-4. These two angles can be calculated as in equations [2-14] and [2-15] below:

$$tan\,\rho_h = \frac{2r\,cos\,\alpha}{L - 2r\,sin\,\alpha} \qquad [2\text{-}14]$$

and

$$tan\,\rho_r = \frac{2rk}{L - C} \qquad [2\text{-}15]$$

where $\alpha = \theta - \pi$, as shown in Figure 2-5. Consequently, the condition for housing-rotor interference prevention can be expressed as below:

$$\frac{2rk}{L-C} \geq \frac{2r\,cos\,\alpha}{L-2r\,sin\,\alpha}$$

[2-16]

It is possible to prove that value of α which maximises the right-hand side of expression [2-16] is given by $sin\alpha = 2b$ and $cos\alpha = \sqrt{1-4b^2}$. The expression can be manipulated to produce the following forms with clearance C, half chord length L and b as variables:

$$k > \frac{1-\frac{C}{L}}{\sqrt{1-4b^2}}$$

[2-17]

or $$k = \frac{a(1-C_L)}{\sqrt{1-4b^2}} \text{ with } a > 1 \text{ and } C_L = \frac{C}{L}$$

[2-18]

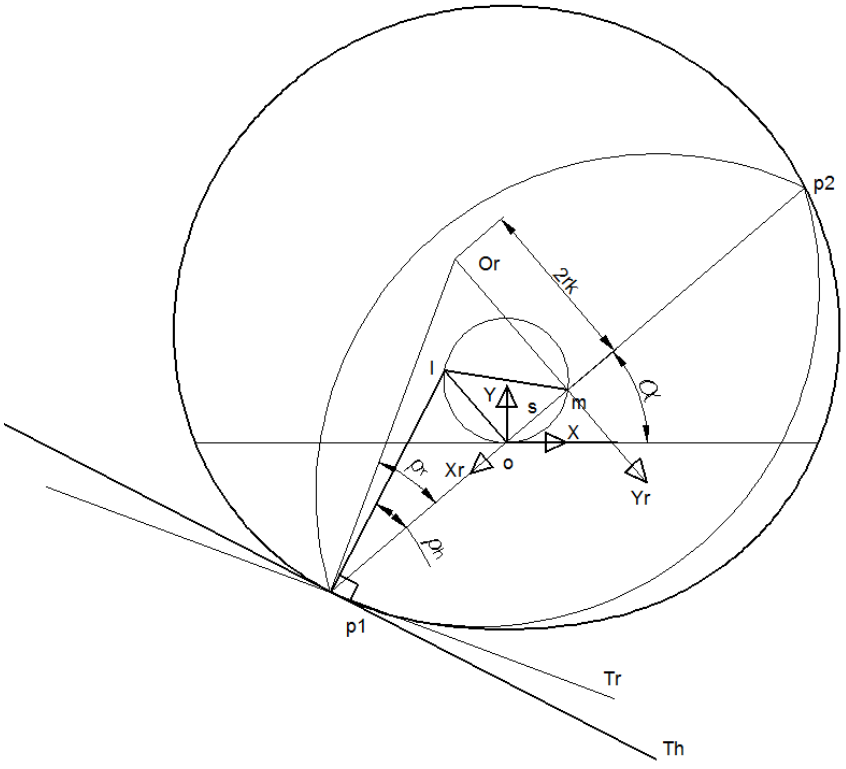

Figure 2-5: Housing-rotor tangent method

The limaçon-to-circular design factor, a, is introduced here as a tool to enable the designer to control the geometrical aspect of the rotor. The value of a is selected by the designer such that it is always greater than one. Also from equation [2-18], the rotor radius R can be manipulated and expressed as $R = (1 - C_L)\sqrt{L^2 + \frac{4r^2a^2}{1-4b^2}}$.

In the next section, the radial clearance problem will be presented.

2.4.5. The housing-rotor radial clearance method

If a sufficiently high value of factor a is employed (e.g.: $a = 1.3$), as shown in the previous section, this will ensure that the interference between housing and rotor will not occur. However, a high value of a may adversely affect the volumetric efficiency of the machine. Consequently, a small value of clearance, C, is introduced to the rotor geometry with the objective of ensuring that a minimum housing-rotor distance, Δ_{min}, is accomplished. As such the problem can be represented as an optimisation endeavour undertaken to calculate the value of C and a to meet certain design requirements. The mathematical formulation of the optimisation problem will feature the calculation of the radial distance, Δ, between any point on the lobe of the rotor and the corresponding point on the housing on the same radial line, R_h, as shown in Figure 2-6. Also in Figure 2-6, the distance from the pole, o, to the lower rotor lobe can be defined as z; $\beta = [0, \pi]$ is the angle between the rotor chord and z; $o_r o = \sqrt{s^2 + (2.r.k)^2}$ is the distance from the centre of rotor lobe to the pole o; γ represents the angle between $o_r o$ and the rotor chord. Hence, the rotor lobe radius R can be expressed as:

$$R^2 = [s^2 + (2rk)^2] + z^2 - 2z\sqrt{s^2 + (2rk)^2}\, cos(\gamma + \pi - \beta) \quad [2\text{-}19]$$

or

$$R^2 = s^2 + (2rk)^2 + z^2 + 2z(s\, cos\, \beta + 2rk\, sin\, \beta) \quad [2\text{-}20]$$

From equation [2-20] the rotor radial distance, z, can be calculated as shown below, note that only the positive root is selected:

$$z = -(s\cos\beta + 2rk\sin\beta) + \sqrt{R^2 - (s\sin\beta - 2rk\cos\beta)^2}$$

[2-21]

The value R_h given in equation [2-9] can also be expressed as:

$$R_h = L + 2r\,sin(\theta + \beta)$$

[2-22]

which may be re-written in terms of $s, r, \alpha = \theta - \pi$, and β as given below:

$$R_h = L - s\,cos\,\beta - 2r\,cos\,\alpha\,sin\,\beta$$

[2-23]

The radial distance from the pole o to any point on the lower rotor lobe is expressed in equation [2-21]; hence, the housing–rotor radial clearance, Δ, can be evaluated as:

$$\Delta = R_h - z$$

[2-24]

With $R = \sqrt{(L-C)^2 + (2rk)^2}$, it is possible to express the radial clearance, Δ, as below:

$$\Delta = L - 2r\cos\alpha\sin\beta + 2rk\sin\beta - \sqrt{(L-C)^2 + (2rk)^2 - (s\sin\beta - 2rk\cos\beta)^2}$$

[2-25]

The limaçon aspect ratio, b, can also be applied to equation [2-25] to yield:

$$\Delta = L\left[1 - 2b\cos\alpha\sin\beta + 2bk\sin\beta - \sqrt{(1-C_L)^2 + (2bk)^2 - (2b\sin\alpha\sin\beta - 2bk\cos\beta)^2}\right]$$

[2-26]

In order to calculate the required values of $C_L, \alpha, and\ \beta$ to achieve the minimum radial clearance Δ_{min} assigned by the designer, the following system of nonlinear equations has to be solved simultaneously:

$$\begin{cases} \Delta - \Delta_{min} = 0 \\ \partial\Delta/\partial\alpha = 0 \\ \partial\Delta/\partial\beta = 0 \end{cases}$$

[2-27]

The above system of equations can be solved for the angles α and β at which the radial clearance Δ is at its minimum value. This system has been manipulated to produce the following outcome:

$$\Delta_{min} = L\left[1 - 2b + 2bk - \sqrt{(1 - C_L)^2 + (2bk)^2}\right]$$

[2-28]

where k is a function of the factor a as shown in equation [2-18].

The volumetric relations of the limaçon-to-circular machine are conveyed in the following section.

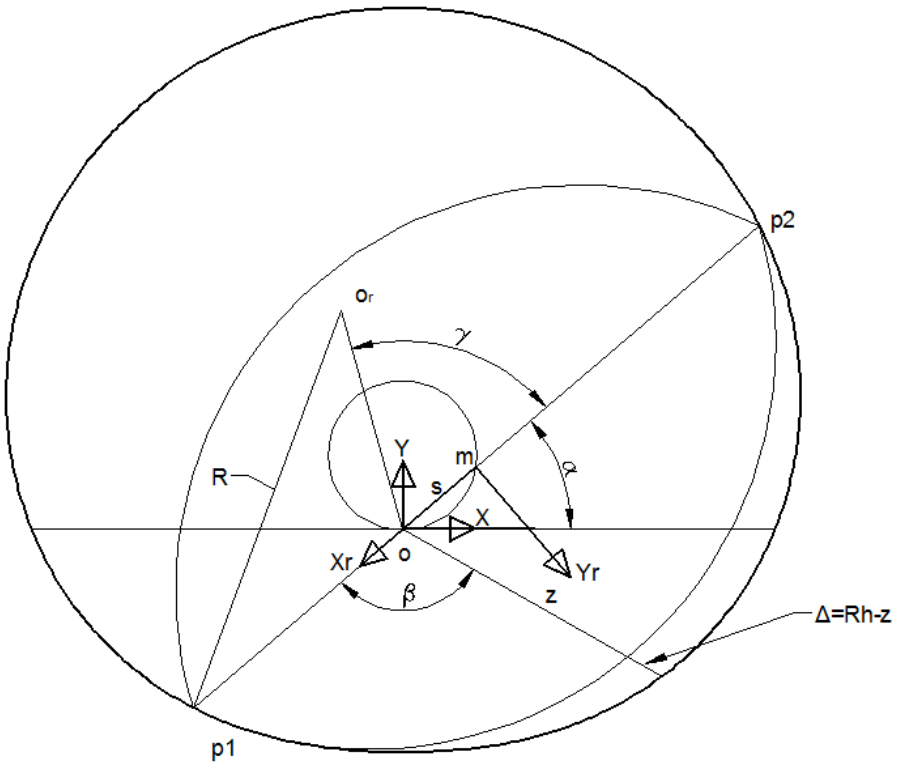

Figure 2-6: Housing-rotor radial clearance

2.4.6. The volumetric relations

The geometry previously described in Figure 2-4 can be used to obtain the volumetric relationship of the limaçon-to-circular machine. The cross-sectional area of the housing above the rotor chord, A_h, suggested by Sultan (2005) is as follows:

$$A_h = \left(r^2 + \frac{L^2}{2}\right)\pi + 4rL\cos\theta \quad [2\text{-}29]$$

or

$$A_h = L^2\left[\left(b^2 + \frac{1}{2}\right)\pi + 4b\cos\theta\right] \quad [2\text{-}30]$$

The rotor area, A_r, can be calculated by the following expressions:

$$A_r = [(L-C)^2 + (2rk)^2]\varphi - (L-C)2rk \quad [2\text{-}31]$$

or

$$A_r = L^2(1-C_L)\left[\tan^{-1}\frac{\sqrt{1-4b^2}}{2ab}\left(1 + \frac{4a^2b^2}{1-4b^2}\right) - \frac{2ab}{\sqrt{1-4b^2}}\right] \quad [2\text{-}32]$$

where $\varphi = \tan^{-1}\frac{L-C}{2rk}$ or $\varphi = \tan^{-1}\frac{\sqrt{1-4b^2}}{2ab}$. Then the net area between the housing and rotor, A_{net}, can be calculated by subtracting A_r from A_h as follows:

$$A_{net} = L^2\left\{\left[\left(b^2 + \frac{1}{2}\right)\pi + 4b\cos\theta\right] - (1-C_L)\left[\tan^{-1}\frac{\sqrt{1-4b^2}}{2ab}\left(1 + \frac{4a^2b^2}{1-4b^2}\right) - \frac{2ab}{\sqrt{1-4b^2}}\right]\right\} \quad [2\text{-}33]$$

The rotor and housing depth H, which is measured perpendicular to the XY coordinate, can be set as $H = hL$, where, the multiplication factor, h, can be selected by the designer. The volume V_{net} between the housing limaçon and rotor can be expressed as:

$$V_{net} = A_{net}H \quad [2\text{-}34]$$

The volumetric ratio, R_{vol}, which is described as the minimum chamber volume to the maximum chamber volume, has a critical impact on the efficiency of the positive displacement machine, particularly when gas is used as a working fluid. This volumetric ratio, R_{vol}, can be expressed in terms of the ratio of net chamber area when the angle $\theta = \pi$ to the net chamber area when $\theta = 0$:

$$R_{vol} = \frac{V_{net|\theta=\pi}}{V_{net|\theta=0}} \quad [2\text{-}35]$$

From equations [2-33] and [2-35], R_{vol} can be expanded as follows:

$$R_{vol} = \frac{\left[\left(b^2 + \frac{1}{2}\right)\pi - 4b\right] - \left(1 - \frac{C}{L}\right)\left[\tan^{-1}\frac{\sqrt{1-4b^2}}{2ab}\left(1 + \frac{4a^2b^2}{1-4b^2}\right) - \frac{2ab}{\sqrt{1-4b^2}}\right]}{\left[\left(b^2 + \frac{1}{2}\right)\pi + 4b\right] - \left(1 - \frac{C}{L}\right)\left[\tan^{-1}\frac{\sqrt{1-4b^2}}{2ab}\left(1 + \frac{4a^2b^2}{1-4b^2}\right) - \frac{2ab}{\sqrt{1-4b^2}}\right]} \quad [2\text{-}36]$$

An important design criterion for a positive displacement machine is the volume of working fluid expected to be induced into the working chamber during the suction stroke, V_{ind}, which can be calculated as:

$$V_{ind} = V_{net|\theta_{cut\_off}} - \mu V_{net|\theta=0} \quad [2\text{-}37]$$

Where $\theta_{cut\_off} \in [0, \pi]$ is the angle at which the inlet port of the machine is closed. The fluid left in the working chamber from the previous cycle will have its effect onto the intake volume of the machine, this effect is taken care of by the clearance volume factor, μ, in equation [2-37]. The value of μ can be assigned by the designer to match expected compressibility, valve losses and leakage. In less conservative designs, μ can be defined as the ratio between the average fluid density of the discharge and induction strokes as below (Sultan, 2008):

$$\mu = \frac{\rho_{out}}{\rho_{in}}$$

[2-38]

An optimisation procedure and some case studies for the limaçon-to-circular machine will be demonstrated in the following section.

2.4.7. Background on stochastic approximation

The optimisation process in this paper employs the use of the simultaneous perturbation stochastic approximation (SPSA) method introduced and detailed by Spall (1987, 1992, 1998, 2000), and since being refined (Bartkute & Sakalauskas, 2007; Spall, 2012; Wang, 2013). Such a method has been used in a wide range of publications such as tidal modelling (Altaf, Heemink, Verlaan, & Hoteit, 2011), automation, computing and control (Abdulsadda & Iqbal, 2011; Cao, 2011), and design (Sultan, 2007). The goal of this approach is to minimise a scalar-valued loss function, $\Lambda(\Phi)$, in relation to a design vector, Φ. The measured value of the loss function available at any value of Φ may be expressed as follow:

$$\mathrm{F}(\Phi) = \Lambda(\Phi) + \text{noise}$$

[2-39]

From an initial guess value of Φ, the iteration process takes place following the approximation of the gradient $\mathrm{G}(\Phi) = \frac{\partial \Lambda(\Phi)}{\partial \Phi}$. Additionally, it is assumed that $\Lambda(\Phi)$ is a differentiable function of Φ and the minimum point Φ_0 corresponds to the zero point of the gradient $\mathrm{G}(\Phi_0) = 0$.

With the above understanding, the SPSA procedure starts at $k = 0$ with a guess design vector $\widehat{\Phi}_0$ (the $\widehat{\ }$ symbol represents estimates) and a given set of five non-negative parameters, $\Psi, \Omega, A, \Psi_s, and\ \omega_s$. The values of $\Psi_s\ and\ \omega_s$ have been suggested by Spall as 0.602 and 0.101 respectively, and the value of A is one-tenth the number of iterations

allowed by the user. The remaining two parameters, Ψ *and* Ω, are selected to match a given application. The gain sequences Ψ_k *and* ω_k are calculated at iteration step number k using the following equations:

$$\Psi_k = \frac{\Psi}{(A+k+1)^{\Psi_s}} \quad [2\text{-}40]$$

and

$$\omega_k = \frac{\Omega}{(k+1)^{\omega_s}} \quad [2\text{-}41]$$

At each iteration, an n-dimensional perturbation vector D_k is generated where each of its components is randomly assigned the value of ± 1 using a binary Bernoulli distribution. As such, vector D_k can be expressed as:

$$D_k = \pm 1 \; with \; probability \; of \; \frac{1}{2}$$

To this end, two measurements of the loss function at $\hat{\Phi}_k$ can be obtained as $F(\hat{\Phi}_k + \omega_k D_k)$ *and* $F(\hat{\Phi}_k - \omega_k D_k)$. Hence, the gradient of the loss function with respect to the vector $\hat{\Phi}$ can be written as:

$$G(\hat{\Phi}_k) = \frac{F(\hat{\Phi}_k+\omega_k D_k)-F(\hat{\Phi}_k-\omega_k D_k)}{2\omega_k} \begin{bmatrix} D_{k1}^{-1} \\ D_{k2}^{-1} \\ \cdots \\ D_{kn}^{-1} \end{bmatrix} \quad [2\text{-}42]$$

where D_{ki} is the i^{th} component of the D_k vector. At the end of iteration k, the estimated value $\hat{\Phi}_k$ is replaced by $\hat{\Phi}_{k+1}$ by using the follow equation:

$$\hat{\Phi}_{k+1} = \hat{\Phi}_k - \psi_k \hat{G}_k(\hat{\Phi}_k) \quad [2\text{-}43]$$

In the next section, the SPSA approach is used to optimise the design process of the limaçon-to-circular machine where an objective function will be established to encompass the desired performance characteristic

2.4.8. The optimisation method

The optimisation procedure is undertaken to ensure that the designed machine will meet certain geometric requirements. These requirements are minimum clearance required by the designer to suit a specific application, Δ_{min_req}; a required volumetric ratio, R_{vol_req} and a required induce volume, V_{ind_req}. The design vector which will realise these requirements include L, a, b and C_L. The expected outcome of the optimisation procedure is that the achieved values of $\Delta_{min}, R_{vol}, and\ V_{ind}$ are related to their corresponding required values as follows:

$$\begin{cases} \Delta_{min} - \Delta_{\min\_req} > 0 \\ R_{vol\_req} - R_{vol} > 0 \\ V_{ind} - V_{ind\_req} > 0 \end{cases}$$

[2-44]

The manner in which the variable design parameters affect $\Delta_{min}\ and\ R_{vol}$ is shown in Figure 2-7. It is obvious that the settings of factors a and b affect the values of $R_{vol}\ and\ \Delta_{min}$ considerably.

The integration of the above inequalities into the optimisation process will introduce slack variables d, R and v, as follows:

$$\begin{cases} d = \Delta_{min} - \Delta_{\min\_req} \\ R = R_{vol\_req} - R_{vol} \\ v = V_{ind} - V_{ind\_req} \end{cases}$$

[2-45]

Equations [2-45] can also be expressed in terms of zero-valued functions as follows:

$$\begin{cases} F_{\Delta} = \left(\Delta_{min} - \Delta_{min\_req} - d\right)^2 \\ F_R = \left(R_{vol} - R_{vol_{req}} + R\right)^2 \\ F_V = \left(V_{ind} - V_{ind_{req}} - v\right)^2 \end{cases}$$

[2-46]

To this end, the design vector Y can be constructed as $Y = [L \quad a \quad b \quad C_L \quad d \quad R \quad v]^T$. Functions of $\Delta_{min}, R_{vol}, and\ V_{ind}$ in equation [2-46] can then be incorporated into an overall zero-valued objective function, E, as given below:

$$E = w_1 F_{\Delta} + w_2 F_R + w_3 F_V$$

[2-47]

where $w_1, w_2,$ and w_3 are the weighting factors assigned to highlight the significance of the various terms in the objective function, E. The values of these weighting factors can be selected by the designer based on the type of limaçon machine and its working conditions. By way of an example, w_1 will be given higher values than w_2 and w_3 for

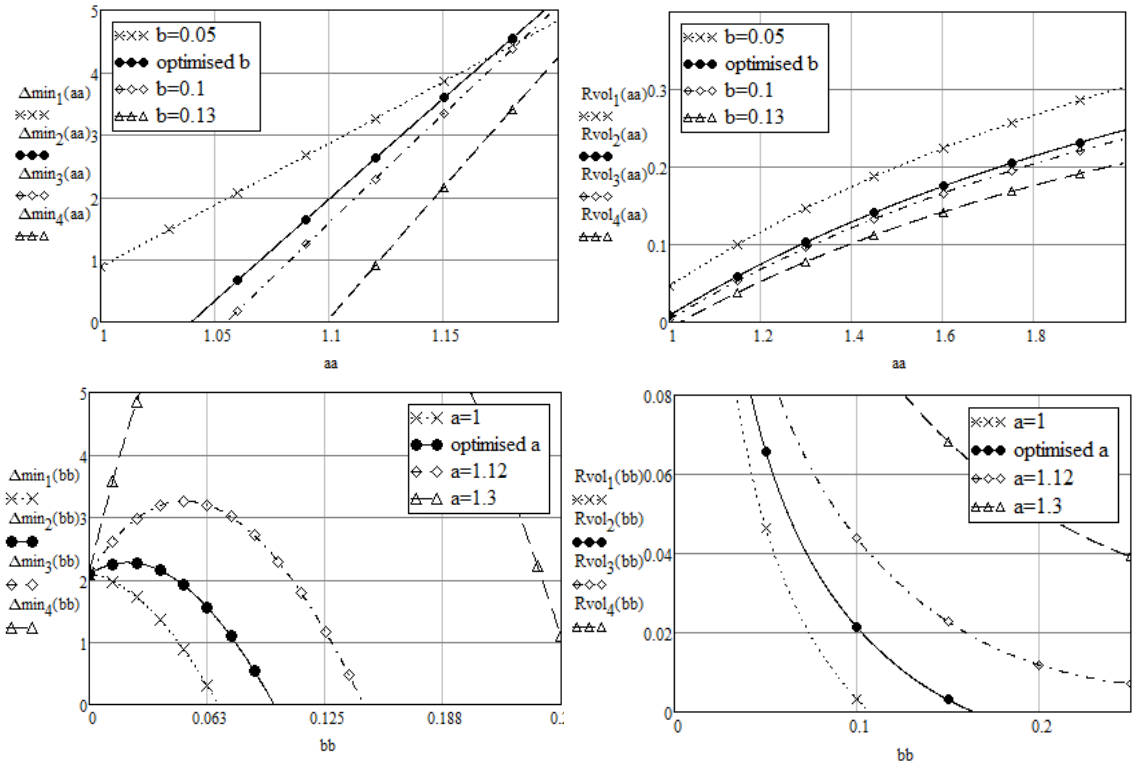

Figure 2-7: The effect of factors a and b on radial clearance and volumetric ratio

cases where the machine is designed to handle gaseous fluids. On the other hand w_3 will be given higher values for pumps which are expected to handle liquid where the flow rate is of particular importance. In cases where space limitation impose size constrains on the design, w_2 is given higher values to ensure that the produced machine falls within specified dimensions.

Applying the SPSA approach to this specific problem, at iteration k the updated values Y_{k+1} can be expressed as:

$$Y_{k+1} = Y_k - \Psi_k \frac{E(Y_k+\omega_k D_k)-E(Y_k-\omega_k D_k)}{2\omega_k} \begin{bmatrix} D_{k_1}^{-1} \\ D_{k_2}^{-1} \\ \dots \\ D_{k_n}^{-1} \end{bmatrix}$$

[2-48]

In case of an entry number j, Y_{k+1}^j of Y_{k+1} falls outside its allowable domain, an adjustment process has been introduced as suggested by Kothandaraman et al. (2005) to re-assign this entry to its the nearest boundary value. The process can be expressed mathematically as follows:

$$Y_{k+1}^j = \begin{cases} Y_{min}^j & if \quad Y_{k+1}^j < Y_{min}^j \\ Y_{max}^j & if \quad Y_{k+1}^j > Y_{max}^j \end{cases}$$

[2-49]

2.4.9. Numerical illustrations

The design procedure presented above is employed in this section to calculate limaçon-to-circular machine dimensions (half rotor length, L, designing factor, a, aspect ratio, b, and ratio C_L) which will correspond to the desired performance characteristics ($\Delta_{min}, R_{vol}, and\ V_{ind}$). A measured constrain impose in all designs is $b \in (0,0.25]$.

In order to validate the design model presented in this paper, case studies of such machine in different operating conditions have been established and fed to the optimisation process.

Case study 1: This case study features a limaçon-to-circular compressor with $H = hL$ where $h = 1.5, \mu = 5, \theta_{cut\_off} = \pi, \Delta_{\min\_req} \geq 0.2\ mm, R_{vol\_req} \leq 0.03, V_{ind\_req} \geq 1.056 \times 10^7\ mm^3$. The above data has been fed to the design and optimisation procedure to obtain the required results: half chord length $L = 222.688\ mm$, designing factor $a = 1.052$, aspect ratio $b = 0.09$, the ratio $C_L = 9.385 \times 10^{-3}$, induce volume $V_{ind} = 1.032 \times 10^7\ mm^3$, volume metric ratio $R_{vol} = 0.027$ and minimum radial clearance $\Delta_{min} = 0.395\ mm$.

Figure 2-8 shows how the value of the objective function steadily diminished during the iterative procedure.

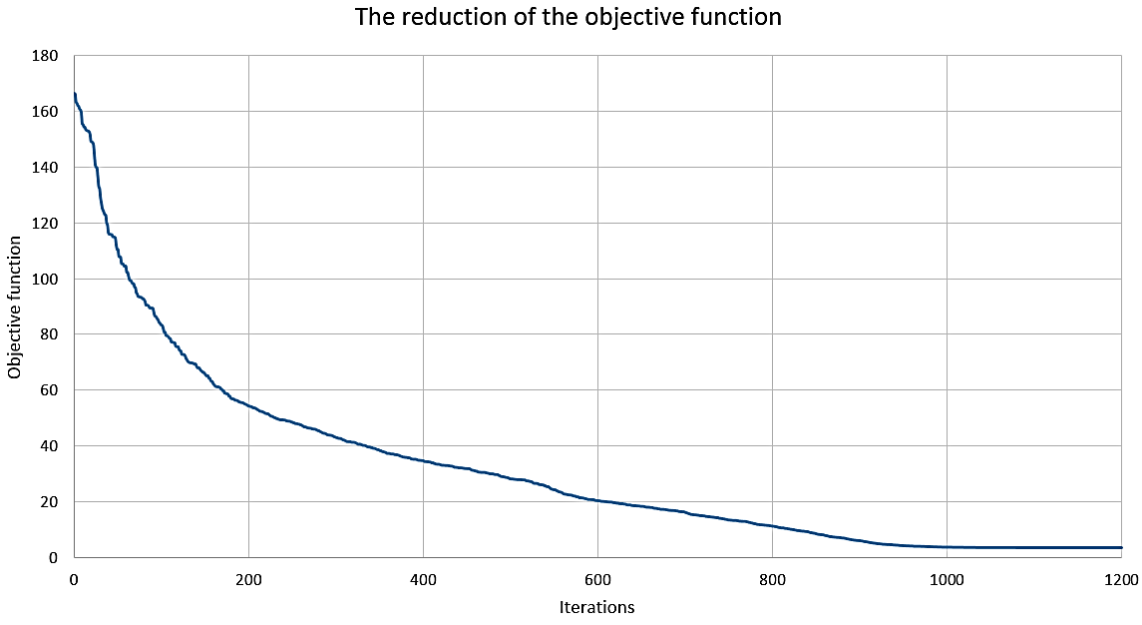

Figure 2-8: The reduction of the objective function E during iterations

Case study 2: This case study features a limaçon-to-circular expander with $H = hL$ where $h = 1.5,\ \mu = \frac{1}{6},\ \theta_{cut\_off} = \frac{5\pi}{6},\ \Delta_{\min\_req} \geq 0.2\ mm,\ R_{vol\_req} \leq 0.03,\ V_{ind\_req} \geq$

$1.056 \times 10^7\ mm^3$. The above data has been fed to the design and optimisation procedure to obtain the required results: half chord length $L = 194.177\ mm$, designing factor $a = 1.142$, aspect ratio $b = 0.127$, the ratio $C_L = 2.87 \times 10^{-3}$, induced volume $V_{ind} = 0.9848 \times 10^7\ mm^3$, volume metric ratio $R_{vol} = 0.024$ and minimum radial clearance $\Delta_{min} = 0.793\ mm$.

Case study 3: This case study features a limaçon-to-circular pump with $H = hL$ where $h = 1.112$, $\mu = 1.15$, $\theta_{cut\_off} = \pi$, $\Delta_{\min\_req} \geq 0.2\ mm$, $R_{vol\_req} \leq 0.03$, $V_{ind\_req} \geq 1.056 \times 10^7\ mm^3$. The above data has been fed to the design and optimisation procedure to obtain the required results: half chord length $L = 204.169\ mm$, designing factor $a = 1.149$, aspect ratio $b = 0.141$, the ratio $C_L = 3.674 \times 10^{-3}$, induced volume $V_{ind} = 1.245 \times 10^7\ mm^3$, volume metric ratio $R_{vol} = 0.024$ and minimum radial clearance $\Delta_{min} = 0.592\ mm$.

Table 2-1: Limaçon-to-circular machine case studies

Results obtained for case studies $\Delta_{min\_req} \geq 0.2\ mm, R_{vol\_req} \leq 0.03, V_{ind\_req} \geq 1.056 \times 10^7\ mm^3$			
	Case 1: Compressor	Case 2: Expander	Case 3: Pump
h	1.5	1.5	1.112
μ	5	1/6	1.15
$\theta_{cut_{off}}(rad)$	π	$5\pi/6$	π
$L(mm)$	222.688	194.177	204.169
a	1.052	1.142	1.149
b	0.09	0.127	0.141
C_L	9.385 x 10^{-3}	2.87 x 10^{-3}	3.674 x 10^{-3}
$V_{ind}(mm^3)$	1.032 x 10^7	0.9848 x 10^7	1.245 x 10^7
R_{vol}	0.027	0.024	0.024
$\Delta_{min}(mm)$	0.395	0.793	0.592

2.4.10. Conclusion

This paper presents a background on the rotary positive displacement machines, which are based on the limaçon technology. A modification has been proposed for the rotor design with the aim of simplifying manufacture and reducing the production cost. This proposed modification results in new rotor-housing interactions, which require an in-depth geometric modelling in relation to rotor-housing interference and volumetric characteristics. The rotor-housing interference has been discussed using two mathematical approaches: a tangent based technique, and a radial clearance based method. Moreover, an optimisation procedure has been employed to calculate the optimum dimensions for the machine to meet certain operational requirements. The outcome of the study confirms the validity of the proposed modification and the suitability to describe the geometric characteristics of the new machine. This was highlighted by the three case studies presented at the end of the paper. Future work planned on this topic will feature the inclusion of the thermodynamical behaviour of the working fluid and the effects of various geometric parameters on the machine performance.

2.4.11. Nomenclatures

SPSA : Simultaneous Perturbation Stochastic Approximation

TFC : Trilateral Flash Cycle

p_1 and p_2 : points on the rotor chord

L : half rotor width

C : housing-rotor clearance

C_L : the ratio of $\frac{C}{L}$

L_r : half the rotor width with clearance C

r : radius of limaçon base circle

a : the limaçon-to-circular machine design factor (selected by designer)

b : the limaçon ratio of r/L

XY : stationary coordinate located at pole o

X_rY_r : coordinate attached to rotor

s : sliding distance measured along X_r

θ : angle rotated by rotor measured from X_r to X axis

R_h : radial distance from pole o to limaçon housing

z : radial distance from pole o to rotor lobe

T_r : tangent to the rotor at the apex

T_h : correspondent tangent to the limaçon housing

ρ_h : angle between X_r and radius of curvature at the contact point on the housing

ρ_r : angle between X_r and the radius of the rotor lobe

R : radius of the rotor lobe

Δ : radial clearance between housing and rotor

Δ_{min} : minimum radial clearance introduced by the designer

A_h : cross-section area of the housing

A_r : cross-section area of the rotor

A_{net} : area between limaçon housing and rotor

R_{vol} : volumetric ratio

V_{ind} : induced volume

H : housing and rotor depth

μ : clearance volume factor

ρ_{out} : average discharge density

ρ_{in} : average intake density

References

Abdulsadda, A., & Iqbal, K. (2011). An improved SPSA algorithm for system identification using fuzzy rules for training neural networks. International Journal Of Automation And Computing, 8(3), 333-339. doi: 10.1007/s11633-011-0589-x

Altaf, M., Heemink, A., Verlaan, M., & Hoteit, I. (2011). Simultaneous perturbation stochastic approximation for tidal models. Ocean Dynamics, 61(8), 1093-1105. doi: 10.1007/s10236-011-0387-6

Amrouche, F., Erickson, P., Park, J., & Varnhagen, S. (2014). An experimental investigation of hydrogen-enriched gasoline in a Wankel rotary engine. International Journal Of Hydrogen Energy, 39(16), 8525-8534. doi: 10.1016/j.ijhydene.2014.03.172

Bartkutė, V., & Sakalauskas, L. (2007). Simultaneous perturbation stochastic approximation of nonsmooth functions. European Journal Of Operational Research, 181(3), 1174-1188. doi: 10.1016/j.ejor.2005.09.052

Cao, X. (2011). Preliminary Results on Non-Bernoulli Distribution of Perturbations for Silmultaneous Perturbation Stochastic Optimisation. Proceedings of the American Control Conference, 2669-2670. doi: 10.1109/ACC.2011.5991550

Costa, S. I. R., Grou, M. A., Figueiredo, V. (1999). Mechanical curves - a kinematic Greek look through the computer. Int. J. Math. Edu. Sci. Technol., 30(3), 459–469.

Fischer, J. (2011). Comparison of trilateral cycles and organic Rankine cycles. Energy, 36(10), 6208-6219. doi: 10.1016/j.energy.2011.07.041

Georges, E., Declaye, S., Dumont, O., Quoilin, S., & Lemort, V. (2013). Design of a small-scale organic Rankine cycle engine used in a solar power plant. International Journal Of Low-Carbon Technologies, 8(suppl 1), i34-i41. doi: 10.1093/ijlct/ctt030

Jia, X., Zhang, B., Yang, B., & Peng, X. (2009). Study of a Rotary Vane Expander for the Transcritical CO2 Cycle—Part II: Theoretical Modeling. HVAC&R Research, 15(4), 689-709. doi: 10.1080/10789669.2009.10390858

Kim, H., Kim, W., Kim, H., & Kim, S. (2011). Applicability of scroll expander and compressor to an external power engine: Conceptual design and performance analysis. International Journal Of Energy Research, 36(3), 385-396. doi: 10.1002/er.1809

Kothandaraman, G., & Rotea, M. (2005). Simultaneous-Perturbation-Stochastic-Approximation Algorithm for Parachute Parameter Estimation. Journal Of Aircraft, 42(5), 1229-1235. doi: 10.2514/1.11721

Oralli, E., Tarique, M., Zamfirescu, C., & Dincer, I. (2011). A study on scroll compressor conversion into expander for Rankine cycles. International Journal Of Low-Carbon Technologies, 6(3), 200-206. doi: 10.1093/ijlct/ctr008

Phung, T. H., & Sultan, I. A. (n.d.). Geometric design of the limaçon-to-circular fluid processing machine.

Picard, M., Tian, T., & Nishino, T. (2015). Predicting Gas Leakage in the Rotary Engine—Part I: Apex and Corner Seals. Journal Of Engineering For Gas Turbines And Power, 138(6), 062503. doi: 10.1115/1.4031873

Picard, M., Tian, T., & Nishino, T. (2015). Predicting Gas Leakage in the Rotary Engine—Part II: Side Seals and Summary. Journal Of Engineering For Gas Turbines And Power, 138(6), 062504. doi: 10.1115/1.4031874

Spall, J. C. (2012). Stochastic Optimisation. J. Gentle, W. Härdle, and Y. Mori (Eds.), Handbook of Computational Statistics: Concepts and Methods (2nd ed.) (pp.173-201). Heidelberg: Springer-Verlag.

Steffen, M., Löffler, M., & Schaber, K. (2013). Efficiency of a new Triangle Cycle with flash evaporation in a piston engine. Energy, 57, 295-307. doi: 10.1016/j.energy.2012.11.054

Subiantoro, A., & Tiow, O. (2009). Introduction of the Revolving Vane Expander. HVAC&R Research, 15(4), 801-816. doi: 10.1080/10789669.2009.10390865

Sultan, I. (2005). The Limaçon of Pascal: Mechanical Generation and Utilization for Fluid Processing. Proceedings Of The Institution Of Mechanical Engineers, Part C: Journal Of Mechanical Engineering Science, 219(8), 813-822. http://dx.doi.org/10.1243/095440605x31698

Sultan, I. (2006). Profiling Rotors for Limaçon-to-Limaçon Compression-Expansion Machines. Journal Of Mechanical Design, 128(4), 787-793. http://dx.doi.org/10.1115/1.2202877

Sultan, I. (2007). A surrogate model for interference prevention in the limaçon-to-limaçon machines. Engineering Computations, 24(5), 437-449. http://dx.doi.org/10.1108/02644400710755852

Sultan, I. (2008). A Geometric Design Model for the Circolimaçon Positive Displacement Machine. Journal Of Mechanical Design, 130(6), 062307. http://dx.doi.org/10.1115/1.2901143

Sultan, I., & Schaller, C. (2011). Optimum Positioning of Ports in the Limaçon Gas Expanders. Journal Of Engineering For Gas Turbines And Power, 133(10), 103002. doi: 10.1115/1.4003195

Wang, Q. (2013). Optimisation with discrete simultaneous perturbation stochastic optimisation using noisy loss function measurements. PhD Thesis, Baltimore, Maryland.

Wheildon, W. M. (1896). Rotary Engine. United States Patent No. 553086.

Chapter 3: On the apex seal analysis of limaçon positive displacement machines*†

3.1. Abstract

Rotary machines, and limaçon machines in particular, offer a better power to weight ratio compared to reciprocating machines; however, leakage due to improper apex and side sealing have prevented rotary machines from thriving. In this paper, a modelling approach is presented to analyse the vibration of apex seal during the machine operation and the power loss caused by the seal friction. The seal and spring are modelled as a spring-mass system in which the seal deformation is negligible. The seal-groove relative positions have then been categorised into nine different possible cases based on the number of contact points between the seal and the seal groove. A case study has been presented to demonstrate the reliability of the model.

Keywords: Rotary machine; limaçon-to-circular; limaçon; circolimaçon; limaçon motion; pump; gas expander; compressor; positive displacement; seal; apex seal; seal vibration

Article type: research paper

3.2. Introduction

In fluid processing machines, leakage through gaps separating different machine components is a major problem which adversely impacts machine performance. In rotary machines, leakage occurs mainly through the rotor-housing clearance and side gaps. Amrouche et al. (2014) argue that sealing problem is a major disadvantage of the rotary

* A more in-detail version of Sections 3.5.3 and 3.5.4 of this chapter had been presented at Sydney ACAM 9 (November 2017) conference and published (Phung & Sultan, 2017).
† The seal dynamics model section of this chapter has been submitted to Mechanism and Machine Theory journal for publication.

engines. In order to prevent fluid leakage, limaçon rotary machines are equipped with apex seals and side seals. During machine operation, variable forces from the pressure differential between the working chambers, combined with the elastic, inertial and frictional effects, excite vibratory modes into the seals. The resulting vibration or "lift-off" and "poor contact" has been noticed by Matsuura, Terasaki, and Watanabe (1978) who investigated the behaviour of apex seal against the housing surface. Seal vibration will vary the loading pattern between the seal, seal groove and the machine housing which will result in power loss due to friction. On the other hand, Pennock and Beard (1997) considered that the friction between the side seal and the machine rotor is insignificant and can be ignored. The authors then went on to investigate the effect of crankshaft speed fluctuations on apex seal forces and concluded that this effect is also insignificant. Of note is that Pennock and Beard (1997) did not include the gas pressure difference in their study but suggested that such a problem along with different machine starting conditions should be further investigated.

The work by Handschuh and Owen (2010) suggested that the power loss of rotary machines is drastically affected by the crankshaft rotational speeds and the friction drag coefficient of the apex seal. The seal and rotary machine performance have been investigated from the viewpoint of lubrication and the trajectory of the seal's centre of mass (Drogosz, 2011; Zhang, Liu, Zuo, & Zhang, 2017). These authors concluded that the increase of the rotor rotational speed is likely to decrease the range of maximum to minimum oil film thickness and will decrease the apex seal vibration amplitude. An outcome which reduces the wear of seal and housing surface.

From a different perspective, Warren and Yang (2013) have proposed a deviation-function method for designing the rotary machine based on the apex seal geometry. The authors suggest that this approach will help improve the sealing capability and

effectiveness which would impact the machine performance favourably. On top of that, the newly designed housing reduces forces on apex seal and reduces the wear of the seal and the housing surfaces. Knowing that the apex seal is prone to damage and failure, Rose and Yang (2014) took on the challenge of redesigning the seal. They presented two approaches, a wider apex seal and a multi-apex-seal, designed to provide more stable configurations and improve seal effectiveness.

In the aforementioned literature, the focus had been drawn towards the Wankel engine. In the present paper, however, the limaçon-machine apex seal linear and angular vibrational modes, as well as the dynamic forces acting on the seals from the housing and the seal groove will be investigated. Additionally, the influence of the instantaneous pressure values present in the upper (above the rotor) and lower (below the rotor) working chambers will be duly taken into account. The first attempt at modelling the dynamic performance of limaçon machine apex seals has been based on rigid body dynamics as reported in the work by Phung and Sultan (2017). The current paper, however, presents a more sophisticated formulation where the seal contact with surroundings has been modelled as spring-damper system. As such, a nonlinear three degree of freedom vibration model is constructed and solved numerically using Euler method as the numerical example given at the end of the paper will demonstrate.

3.3. Background on the limaçon positive displacement machines

Belongs to the rotary positive displacement machine category, the limaçon machine has gained its name from the unique motion of the machine rotor inside the housing; such motion always follows the limaçon curve (also referred to as Pascal's snail or snail curve), which can be produced by a number of mechanisms, some of which have been described to a reasonable level of detail by Sultan (2005). In further work by Sultan (2006; 2008) and Phung et al. (2016) it was pointed out that the rotor and housing of limaçon machines

can be manufactured to either limaçon or circular curves; hence, the names: limaçon-to-limaçon machines (Sultan, 2005; Sultan, 2006; Sultan, 2007), circolimaçon machines (Sultan, 2008), and the limaçon-to-circular machines (Phung, Sultan, & Boretti, 2016).

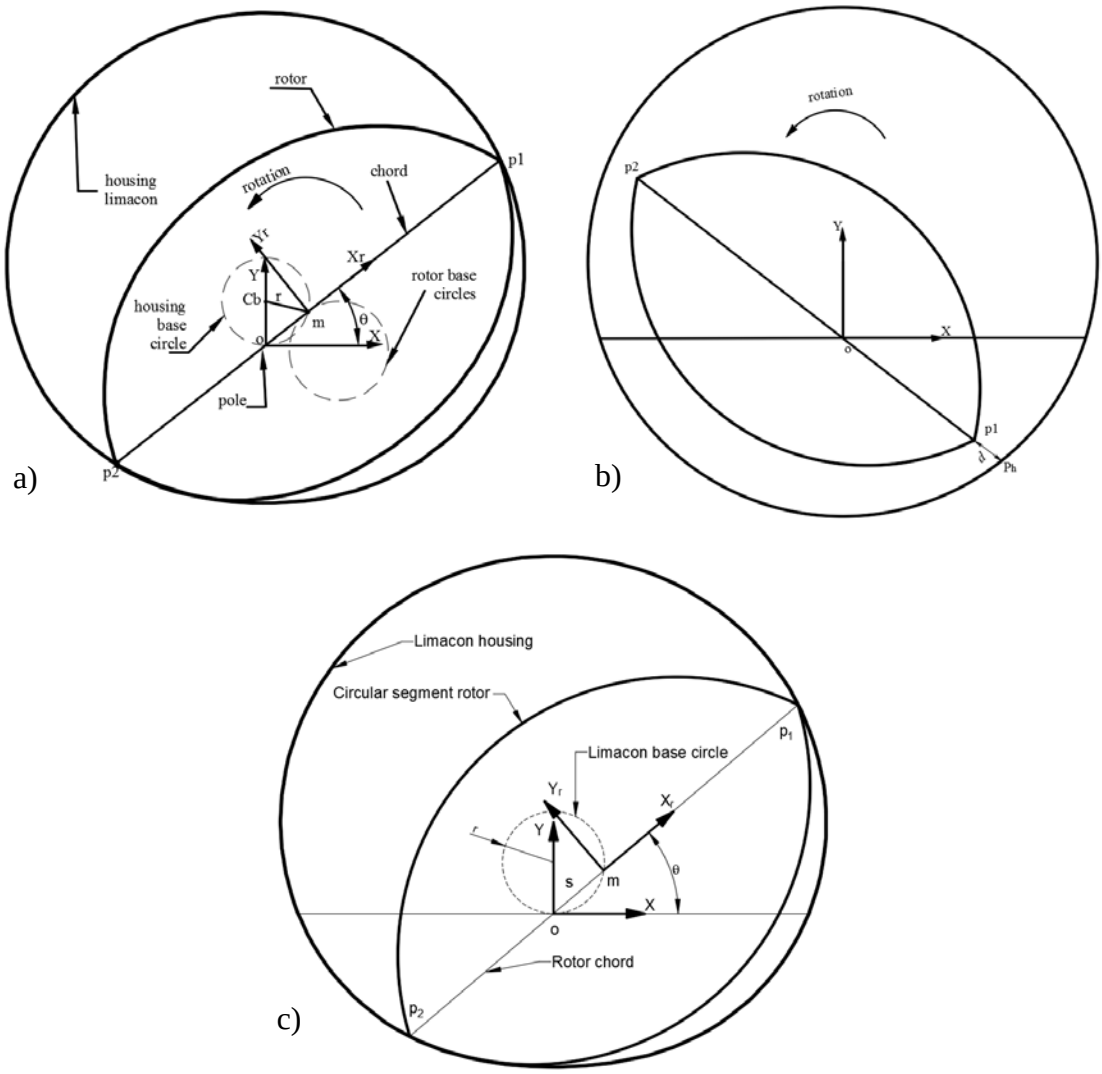

Figure 3-1: Limaçon machine embodiments
Note how the rotor profiles differ in each embodiment:
a) Limaçon-to-limaçon machine, b) Circolimaçon machine, c) Limaçon-to-circular machine

As shown in Figure 3-1, the three machine embodiments share some similar operational characteristics. The rotor chord, p_1p_2, of length $2L$ rotates and slides about the limaçon pole, o. As for the cases of the limaçon-to-limaçon and the limaçon-to-circular machines, the housings are the curves formed by the traces of point p_1 $(or\ p_2)$,

namely limaçon curve, while the housing of the circolimaçon is a circular curve. The machines' rotor takes the two-lobe form. The two lobes are mirrored images of each other in which each lobe is manufactured to either limaçon or circular curves. The centre point of the rotor chord, m, is restricted to move on a stationary circle of radius r, this circle is referred to as the limaçon base circle. A stationary Cartesian frame X_oY_o is introduced and attached to the pole o; at the same time, a rotating frame X_rY_r is attached to the rotor chord, p_1p_2, at its centre point, m, as shown in Figure 3-1. The rotor angular displacement, $\theta \in [0,2\pi]$, is the angle rotated by the chord as the rotor performs its rotational motion, this angle θ is measured from the X_o-axis to X_r-axis in the anticlockwise direction. When the chord is sliding, its centre point, m, slides a distance s as a function of the rotor angular displacement, θ, with respect to the pole, o. This sliding distance can be formulated as follows (Sultan, 2005; Sultan, 2008):

$$s = 2r \sin\theta \qquad [3\text{-}1]$$

The radial distance of the housing, R_h, measured from the pole, o, to the apex, p_1, can be expressed as:

$$R_h = 2r \sin\theta + L \qquad [3\text{-}2]$$

which can also be described in the Cartesian coordinates, X_oY_o, as:

$$\begin{cases} x_{p_1} = R_h \cos\theta = r \sin 2\theta + L \cos\theta \\ y_{p_1} = R_h \sin\theta = r(1 - \cos 2\theta) + L \sin\theta \end{cases} \qquad [3\text{-}3]$$

In order for the limaçon curve to be looping and dimple free, Costa et al. (1998) explained that the limaçon aspect ratio $b = \frac{r}{L}$ has to be less than 0.25, $\left(b = \frac{r}{L} \leq 0.25\right)$.

By employing the definition of limaçon aspect ratio to the limaçon machine, equation [3-3] can be manipulated to produce:

$$\begin{cases} x_{p_1} = L(b\sin 2\theta + \cos\theta) \\ y_{p_1} = L[b(1-\cos 2\theta) + \sin\theta] \end{cases} \quad [3\text{-}4]$$

During the machine operation, any radial clearance introduced between the two apices, p_1 and p_2, on the rotor chord and their corresponding points on the housing will allow working fluid to escape from the higher-pressure chamber to the lower-pressure chamber, which can inversely affect the machine performance. As such, the rotor apices can be equipped with grooves so that apex seals can be mounted to prevent leakage and improve the machine's efficiency.

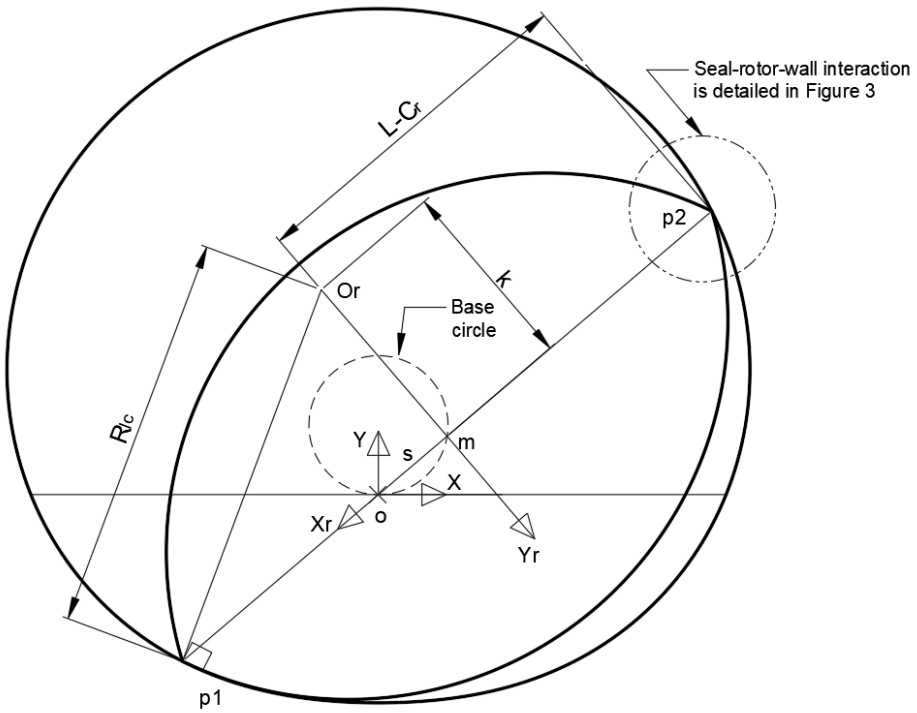

Figure 3-2: Radius of the lower rotor lobe R_{lc} of the circolimaçon and limaçon-to-circular machines

Whilst the radial distance from the rotor centre point to the lobe of the limaçon-to-limaçon machine varies as per equation [3-2], for the circolimaçon and the limaçon-to-

circular machines, the centre point, O_r, of each rotor circular lobe is placed on the Y_r-axis at a distance k, from the pole m, set by the designer. As such, the radius, R_{lc}, of the rotor lobe is calculated, as suggested by Figure 3-2, as follows

$$R_{lc} = \sqrt{(L - C)^2 + (k)^2}$$

[3-5]

In the following sections, the forces and pressures, as well as the motion of the seal will be investigated.

3.4. Apex seal kinematics model formulation

The apex seal is modelled as a simple spring-mass-damper system in which the seal is positioned inside a groove measured W_g in width. A spring is attached to the inner end of the groove and one end of the seal; the other end of the seal pushes against the housing. The cross-sectional area of the seal is almost rectangular with one rounded end, dimensions and geometry of which is depicted in Figure 3-3. The seal width and height are denoted W_s and d_s, respectively. With the case of limaçon-to-limaçon machine, the truncation distance, z, can be calculated as:

$$z = L - (r \sin 2\theta_0 + L \cos \theta_0)$$

[3-6]

where θ_0 is the constant angle between the rotor axis and a line connecting the rotor centre point to edge point 3, which is shown in Figure 3-3. The angle θ_0 can be derived from the limaçon equation [3-3] or [3-4] as follows:

$$\theta_0 = \sin^{-1}\left(-\frac{L}{4r} + \sqrt{\frac{L^2}{(4r)^2} + \frac{W_g}{4r}}\right) = \sin^{-1}\left(-\frac{1}{4b} + \sqrt{\frac{1}{(4b)^2} + \frac{W_g}{4Lb}}\right)$$

[3-7]

With the case of the circolimaçon and the limaçon-to-circular machines, where the rotor lobes are manufactured of circular arcs, the truncation, z, can be calculated as:

$$z = L - C_r - \sqrt{{R_{lc}}^2 - \left(k + \frac{W_g}{2}\right)^2}$$

[3-8]

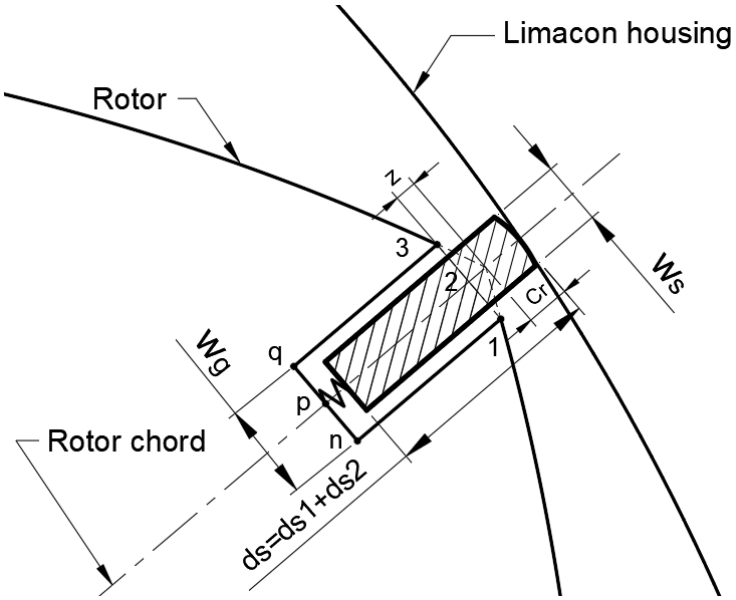

Figure 3-3: Apex seal geometry and dimensions

Let k_s be the seal spring stiffness, and k_w be the equivalent stiffness of the wall of the machine housing $(k_w \gg k_s)$; and let I be the instantaneous centre as shown in Figure 3-4. Of note is that local deformation at the seal-housing contact point has been taken into account in the equivalent stiffness coefficient, k_w. Given that the initial deflection of the seal spring, δ_s, is known at the rotor radial displacement $\theta = 0$; λ measures the angle between the rotor chord, p_1p_2, (as shown in Figure 3-1a) and a line that connects the correspondent point of p_1 on the housing to the instantaneous centre, I (which is shown in Figure 3-4). If μ_1 was the coefficient of friction between the housing and the seal, the initial forces exerted by the machine housing and the spring on to the seal can be calculated as:

$$\begin{cases} F\cos\lambda\,(1-\mu_1\tan\lambda) = k_w\delta_w \\ F_s = k_s\delta_s \end{cases}$$

[3-9]

where $\lambda = \tan^{-1}\left(\frac{2r\cos\theta}{2r\sin\theta+L}\right)$. At the position $\theta = 0$, $\lambda = \lambda_0 = \tan^{-1}\left(\frac{2r}{L}\right)$

δ_w and δ_s are the initial deflections of the housing wall and the spring, respectively. Initially $k_s\delta_s = k_w\delta_w$

Prior to the formulation of seal kinematics, some reasonable approximations need to be made. The first approximation is that the seal cross-sectional area is considered to be constant (rigid or no deformation) due to the fact that the seal deformation is much smaller than the clearances and seal's dimensions change under applied forces. Secondly, all forces acting on the seal, rotor, and housing are considered two-dimensional, which means that none of the forces is acting along the axial direction (perpendicular to the page).

It is also important to point out that the angular and linear variables of the seal cannot be geometrically related; hence, to find those variables, one must solve systems of differential equations.

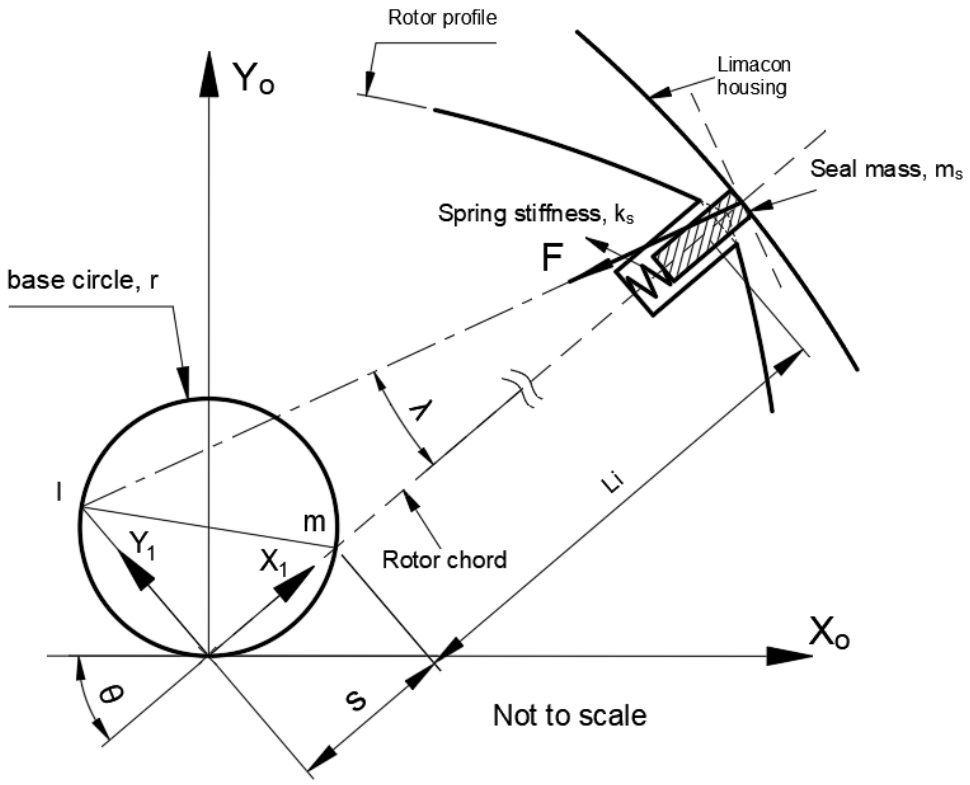

Figure 3-4: Kinematics of apex seal

3.5. A model for seal dynamics

In this section, the contacts between the apex-seal and seal-groove, the seal and machine-housing, and the seal and seal-spring are modelled as spring-mass-damper systems as detailed in Figure 3-5. In Figure 3-5, the groove-attached XY frame and its origin, O_g, is defined at the initial position of a seal-attached frame, X_sY_s whose origin, C, is the centre of gravity of the seal. During the rotational motion of the rotor, the origin, C, of the X_sY_s frame is displaced from its initial position, O_g, to a new position, (x, y), measured in the groove frame, XY. As such, the position of the seal centre of gravity, C, can be described by the position vector $\vec{r}_c$ as follows,

$$\vec{r}_c = \begin{bmatrix} x \\ y \end{bmatrix} \quad [3\text{-}10]$$

Also, the seal frame X_sY_s undergoes an angular displacement, φ, measured from the groove frame in a right-handed sense. Consequently, the unit vectors, $\hat{X}$ and $\hat{Y}$, along the groove frame axes can be related to the unit vectors, $\hat{X}_s$ and $\hat{Y}_s$ using the following frame transformation equation,

$$\begin{bmatrix} \hat{X}_s \\ \hat{Y}_s \end{bmatrix} = \begin{bmatrix} \cos\varphi & -\sin\varphi \\ \sin\varphi & \cos\varphi \end{bmatrix} \begin{bmatrix} \hat{X} \\ \hat{Y} \end{bmatrix}$$

[3-11]

The location of point C with respect to the base frame, X_1Y_1, whose origin is fixed at the origin of the base frame, X_oY_o, but rotates with the rotor at a constant angular velocity, ω, can be expressed as follows:

$$r_c^1 = (2r\sin\theta + L_i + x)\hat{\imath} + y\hat{\jmath}$$

[3-12]

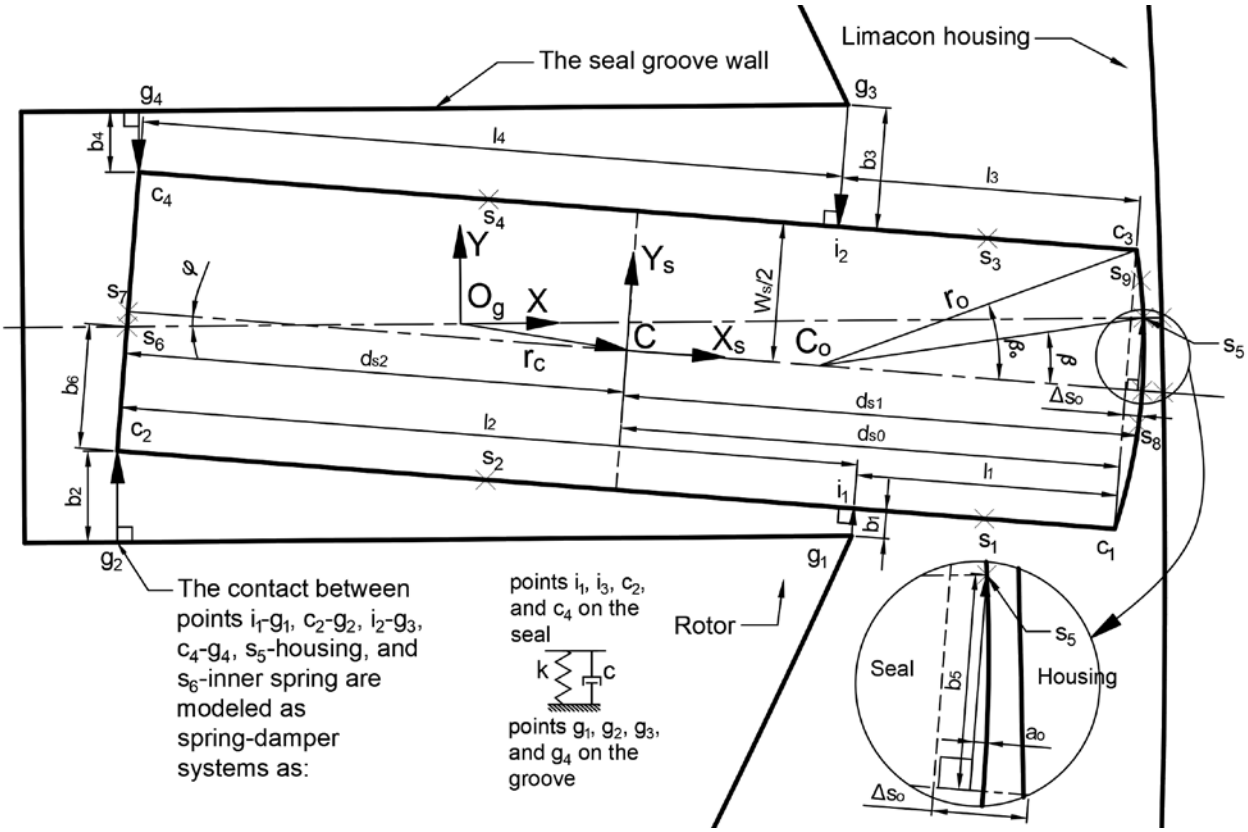

Figure 3-5: Seal dynamics - the elastic contact approach

where $\hat{\imath}$ and $\hat{\jmath}$ are unit vectors in the directions of X_1 and Y_1 respectively and L_i is the distance from the rotor centre point and the seal centre of gravity at the initial position. It is worthy of note here that the frame XY is parallel to the frame X_1Y_1 except the origins of the two frames are separated by a distance $2r\sin\theta + L_i$ along the X_1 axis. With the rotating at a constant angular velocity, ω, the Cartesian frame X_1Y_1 does not experience any form of acceleration and is used in this paper as the frame of reference with respect to which the seal equations of motions will be written.

The velocity of the seal in the X_1Y_1 frame now takes the form:

$$v_c^1 = (2\omega r\cos\theta + \dot{x} - \omega y)\hat{\imath} + (2\omega r\sin\theta + \omega L_i + \omega x + \dot{y})\hat{\jmath} \quad [3\text{-}13]$$

where t denotes time and $\frac{d\theta}{dt} = \omega$. In equation [3-13] above, (.) signifies differentiation with respect to time where $\frac{d\hat{\imath}}{dt} = \omega\hat{\jmath}$, and $\frac{d\hat{\jmath}}{dt} = -\omega\hat{\imath}$. The acceleration of the seal's centre of gravity is expressed as follows:

$$a_c^1 = \ddot{X}_1\,\hat{\imath} + \ddot{Y}_1\,\hat{\jmath} \quad [3\text{-}14]$$

where the acceleration components, $\ddot{X}_1$ and $\ddot{Y}_1$, are given as follows;

$$\begin{cases} \ddot{X}_1 = \ddot{x} - 4r\omega^2\sin\theta - \omega^2 L_i - \omega^2 x - 2\omega\dot{y} \\ \ddot{Y}_1 = \ddot{y} + 4r\omega^2\cos\theta - \omega^2 y + 2\omega\dot{x} \end{cases} \quad [3\text{-}15]$$

The seal axial length, d_s, is defined as the combination of d_{s_1} and d_{s_2} as follows:

$$d_s = d_{s_1} + d_{s_2} \quad [3\text{-}16]$$

where d_{s_1} and d_{s_2} are measured from the seal centre of gravity to the outside and inside ends of the seal, respectively, as shown in Figure 5, which also shows the seal circular-

arc face of radius r_o and its centre, C_o. The angle β_o is measured from the seal centre line to the radial line $C_o c_3$ (or $C_o c_1$) while the angle β is measured from the seal centre line to the radial line $C_o s_5$. These angles, β and β_o, will later on in this paper help determining the locations of points s_5, s_8, and s_9.

It is essential to determine the special points on the seal onto which the forces and pressures from the seal-groove, seal spring, housing wall, and the working chambers would act. The expressions describe the positions of those points will depend on the relative positions, x and y, of the seal centre of gravity, C, and the seal angular position, φ. Such expressions will be determined in the below sections.

3.5.1. Vector representation of the critical contact points

As shown in Figure 3-5, the contact points on the seal groove are labelled from g_1 to g_4, in which points g_1 and g_3 are fixed on the groove and located near the tip of the rotor apex while the actual positions of points g_2 and g_4 vary with the seal's motion. The position vectors from O_g to g_1 and to g_3 can be expressed, respectively, as follows:

$$\vec{r}_{g_1} = \begin{cases} x_{g_1} = d_{s_1} - \zeta_0 - \delta_w \\ y_{g_1} = -\dfrac{W_g}{2} \end{cases} \quad [3\text{-}17]$$

and

$$\vec{r}_{g_3} = \begin{cases} x_{g_3} = d_{s_1} - \zeta_0 - \delta_w \\ y_{g_3} = \dfrac{W_g}{2} \end{cases} \quad [3\text{-}18]$$

Where the constant ζ_0 is the initial value of the seal protrusion outside the apex groove.

In the X_sY_s frame, the contact points c_2 and c_4 fixed on the seal correspond to the moving points g_2 and g_4 on the groove. The position vectors of these points with respect to the moving origin, C, can be expressed respectively as,

$$\vec{r}_{c_2}^{\,S} = \begin{bmatrix} -d_{s_2}\hat{X}_s \\ -\frac{W_s}{2}\hat{Y}_s \end{bmatrix} \quad and \quad \vec{r}_{c_4}^{\,S} = \begin{bmatrix} -d_{s_1}\hat{X}_s \\ \frac{W_s}{2}\hat{Y}_s \end{bmatrix}$$

[3-19]

The contact points on the seal correspond to points g_1 and g_3 are i_1 and i_2, respectively; the position vectors of these points in the XY-frame are shown as follows:

$$\vec{r}_{i_1} = \left[\left(l_2 - d_{s_2}\right)\cos\varphi + \frac{W_s}{2}\sin\varphi\right]\hat{X} + \left[\left(l_2 - d_{s_2}\right)\sin\varphi - \frac{W_s}{2}\cos\varphi\right]\hat{Y}$$

[3-20]

$$\vec{r}_{i_2} = \left[\left(l_4 - d_{s_2}\right)\cos\varphi - \frac{W_s}{2}\sin\varphi\right]\hat{X} + \left[\left(l_4 - d_{s_2}\right)\sin\varphi + \frac{W_s}{2}\cos\varphi\right]\hat{Y}$$

[3-21]

Where l_2 and l_4 are given by the following expressions:

$$l_2 = -x\cos\varphi - y\sin\varphi + d_{s_2} + \left(d_{s_1} - \zeta_0 - \delta_w\right)\cos\varphi - \frac{W_g}{2}\sin\varphi$$

[3-22]

and

$$l_4 = -x\cos\varphi - y\sin\varphi + d_{s_2} + \left(d_{s_1} - \zeta_0 - \delta_w\right)\cos\varphi + \frac{W_g}{2}\sin\varphi$$

[3-23]

Figure 3-5 depicts the contact point s_5 between the seal tip and the machine housing; the vector representation of this point will be defined below. As the seal slides on the machine housing, point s_5 moves between the points c_1 and c_3 on the seal tip. The

positions of c_1 and c_3 with respect to the origin, C, of the moving frame X_sY_s are as follows:

$$\vec{r}_{c_1}^{\,s} = \begin{bmatrix} d_{s_0}\hat{X}_s \\ -\frac{W_s}{2}\hat{Y}_s \end{bmatrix} \quad and \quad \vec{r}_{c_3}^{\,s} = \begin{bmatrix} d_{s_0}\hat{X}_s \\ \frac{W_s}{2}\hat{Y}_s \end{bmatrix}$$

[3-24]

Consequently, the position of s_5 in frame XY can be found as:

$$\vec{r}_{s_5} = \vec{r}_c + (d_{s_1} - a_o)\hat{X}_s + b_5\hat{Y}_s$$

[3-25]

which can be re-written as,

$$\vec{r}_{s_5} = \big(x + (d_{s_1} - a_o)\cos\varphi - b_5\sin\varphi\big)\hat{X} + \big(y + (d_{s_1} - a_o)\sin\varphi + b_5\cos\varphi\big)\hat{Y}$$

[3-26]

where a_o and b_5 are shown in Figure 3-5 and can, respectively, be calculated as,

$$a_o = r_o(1 - \cos\beta)$$

[3-27]

and

$$b_5 = r_o\sin\beta$$

[3-28]

Since point s_5 always stays attached to X-axis, the Y component of point s_5 has to be zero. Hence, the coefficient of the $\hat{Y}$ component of equation [3-26] can be written as:

$$y + (d_{s_1} - a_o)\sin\varphi\sin\varphi + b_5\cos\varphi = 0$$

[3-29]

which can be substituted and rearranged to give

$$y + d_{s_1}\sin\varphi - r_o(1 - \cos\beta)\sin\varphi + r_o\sin\beta\cos\varphi = 0$$

[3-30]

Value of angle β can then be found by solving equation [3-30] as:

$$\beta = \sin^{-1}\left[\left(1 - \frac{d_{s_1}}{r_o}\right)\sin\varphi - \frac{y}{r_o}\right] - \varphi$$

[3-31]

Of note is that if the radius of curvature, r_o, of the seal tip is large, the value of β will approach zero ($\beta \cong 0$), the pressure forces on the seal tip will be acting parallel to the X_s axis.

Equation [3-26] can now be simplified as

$$\vec{r}_{s_5} = \left(x + (d_{s_1} - a_o)\cos\varphi - b_5\sin\varphi\right)\hat{X}$$

[3-32]

The difference in the X component of $\vec{r}_{s_5}$ and the initial value of this component, $d_{s_1} - \delta_w$, will determine the value of the contact force at this point. This difference, Δx_{s_5}, can be calculated as follows:

$$\Delta x_{s_5} = x + (d_{s_1} - a_o)\cos\varphi - b_5\sin\varphi - d_{s_1} + \delta_w$$

[3-33]

where Δx_{s_5} determines the elastic contact force between the seal and the housing as follows,

$$F_w = \begin{cases} k_w \Delta x_{s_5} & if\ \Delta x_{s_5} > 0 \\ 0 & if\ \Delta x_{s_5} \leq 0 \end{cases}$$

[3-34]

It has been assumed that sliding contact exists between the seal and the seal spring. When the seal is at its initial position, the seal-spring contact point is s_7. Point s_7 is on the surface of the seal on the negative side of the X_s-axis as shown in Figure 3-5, this point can be expressed as

$$\vec{r}_{s_7} = \left[\frac{d_{s_2}}{\cos\varphi} - x - \left(\frac{W_s}{2} - b_6\right)\sin\varphi\right]\hat{X} + \left[\left(\frac{W_s}{2} - b_6\right)\cos\varphi\right]\hat{Y}$$

[3-35]

During the motion of the apex seal, the seal-spring contact point shifts away from s_7, this new contact point is labelled s_6. The distance b_6 measured from c_2 to s_6 can be expressed as

$$b_6 = \frac{W_s}{2} + \mathrm{b}_5 - \left(\mathrm{d}_{s_1} - a_o\right)\tan\varphi - d_{s_2}\tan\varphi$$

[3-36]

The distance from the seal centre of gravity to point s_6 can be calculated as:

$$x_{s_6} = \frac{\left(d_{s_1} - a_o\right) + d_{s_2}}{\cos\varphi} - x_{s_5}$$

[3-37]

The position of point s_6 when compared to its initial position, $d_{s_2} - \delta_w$, will determine the spring deflection, Δx_{s_6}, and this will in turn be used to calculate the force exerted by the spring, F_{sp}, on to the inner end of the seal. The spring deflection is given as follows:

$$\Delta x_{s_6} = x_{s_6} - \left(d_{s_2} - \delta_w\right) = \frac{\left(d_{s_1} - a_o\right) + d_{s_2}}{\cos\varphi} - x_{s_5} - \left(d_{s_2} - \delta_w\right)$$

[3-38]

The following spring force exits only if Δx_{s_6}>0,

$$F_{sp} = k_s\left(\Delta x_{s_6} + \delta_s\right)$$

[3-39]

It is now essential to determine the distances between the points g_1, g_2, g_3, and g_4 and their corresponding contact points on the seal – shown as b_1, b_2, b_3, and b_4 in Figure 3-5. If the distances are positive, there are no forces between the seal and the groove;

otherwise, contact forces will exist. The distances b_1, b_2, b_3, and b_4 can be calculated as follows:

$$b_1 = \left(\vec{r}_c + \vec{r}_{c_2}^{\,s} - \vec{r}_{g_1}\right) \cdot \hat{Y}_s = -x \sin\varphi + y \cos\varphi - \frac{W_s}{2} + \left(d_{s_1} - \zeta_0 - \delta_w\right) \sin\varphi + \frac{W_g}{2} \cos\varphi \quad [3\text{-}40]$$

$$b_2 = \left(\vec{r}_c + \vec{r}_{c_2}^{\,s} - \vec{r}_{g_1}\right) \cdot \hat{Y} = y - d_{s_2} \sin\varphi - \frac{W_s}{2} \cos\varphi + \frac{W_g}{2} \quad [3\text{-}41]$$

$$b_3 = -\left(\vec{r}_c + \vec{r}_{c_4}^{\,s} - \vec{r}_{g_3}\right) \cdot \hat{Y}_s = x \sin\varphi - y \cos\varphi - \frac{W_s}{2} - \left(d_{s_1} - \zeta_0 - \delta_w\right) \sin\varphi + \frac{W_g}{2} \cos\varphi \quad [3\text{-}42]$$

$$b_4 = -\left(\vec{r}_c + \vec{r}_{c_4}^{\,s} - \vec{r}_{g_3}\right) \cdot \hat{Y} = -y + d_{s_2} \sin\varphi - \frac{W_s}{2} \cos\varphi + \frac{W_g}{2} \quad [3\text{-}43]$$

The contact forces between the seal and the seal groove at points g_1, g_2, g_3, and g_4 are denoted by $F_{g_1}, F_{g_2}, F_{g_3}$, and F_{g_4}, respectively. The forces F_{g_2} and F_{g_4} act along the lines that are perpendicular to the walls of the seal groove at points g_2 and g_4, respectively; while the forces F_{g_1} and F_{g_3} act along the lines that are perpendicular to the seal side surfaces at points i_1 and i_2, respectively. Those lines of action are shown in Figure 3-5. The conditions from which the magnitudes and directions of the seal and seal-groove forces can be determined are shown in Algorithm 3-1 below:

Algorithm 3-1: Conditions to determine the magnitude and direction of the seal and seal-groove forces

```
1   Begin
2       if b_1 < 0 then
3           F⃗_g1 = |b_1| k_g1 (−γ_1 μ_2 X̂_s + Ŷ_s)
4           else F⃗_g1 = 0⃗
5       end if
6       if b_2 < 0 then
7           F⃗_g2 = |b_2| k_g2 (−γ_2 μ_2 X̂ + Ŷ)
8           else F⃗_g2 = 0⃗
9       end if
10      if b_3 < 0 then
11          F⃗_g3 = |b_3| k_g3 (−γ_3 μ_2 X̂_s − Ŷ_s)
12          else F⃗_g3 = 0⃗
13      end if
14      if b_4 < 0 then
15          F⃗_g4 = |b_4| k_g4 (−γ_4 μ_2 X̂ − Ŷ)
16          else F⃗_g4 = 0⃗
17      end if
18  End
```

where k_{g_i} is the stiffness of the groove material at location g_i and γ_i signifies the sign of the relative velocity at the same location $(i = 1, 2, 3, 4)$; μ_2 is the friction coefficient between the seal and seal-groove.

When the value of b_i is greater than zero $(b_i > 0)$ pressures from the working chambers are able to enter the cavity between the seal and seal groove, which will affect the seal dynamics. These forces will act at points s_1, s_2, s_3, and s_4 as shown in Figure 3-5, where s_1, s_2, s_3, and s_4 are the mid-points between $i_1 - c_1$, $c_2 - i_1$, $i_2 - c_3$, and $c_4 - i_2$, respectively. The positions of such points can be expressed in the XY frame as follows:

$$\vec{r}_{s_1} = \left[\left(d_{s_1} - \frac{l_1}{2}\right)\cos\varphi + \frac{W_s}{2}\sin\varphi\right]\hat{X} + \left[\left(d_{s_1} - \frac{l_1}{2}\right)\sin\varphi - \frac{W_s}{2}\cos\varphi\right]\hat{Y} \quad [3\text{-}44]$$

$$\vec{r}_{s_2} = \left[\left(\frac{l_2}{2} - d_{s_2}\right)\cos\varphi + \frac{W_s}{2}\sin\varphi\right]\hat{X} + \left[\left(\frac{l_2}{2} - d_{s_2}\right)\sin\varphi - \frac{W_s}{2}\cos\varphi\right]\hat{Y}$$

[3-45]

$$\vec{r}_{s_3} = \left[\left(d_{s_1} - \frac{l_3}{2}\right)\cos\varphi - \frac{W_s}{2}\sin\varphi\right]\hat{X} + \left[\left(d_{s_1} - \frac{l_3}{2}\right)\sin\varphi + \frac{W_s}{2}\cos\varphi\right]\hat{Y}$$

[3-46]

$$\vec{r}_{s_4} = \left[\left(\frac{l_4}{2} - d_{s_2}\right)\cos\varphi - \frac{W_s}{2}\sin\varphi\right]\hat{X} + \left[\left(\frac{l_4}{2} - d_{s_2}\right)\sin\varphi + \frac{W_s}{2}\cos\varphi\right]\hat{Y}$$

[3-47]

where $l_1 = d_{s_2} + d_{s_0} - l_2$ and $l_3 = d_{s_2} + d_{s_0} - l_4$

It worthy of note here that the distance d_{s_0} is measured along X_s from the centre of gravity of the seal to the point where the curved end starts. In the next section, the forces and pressures on the apex seal at the special points featured here will be calculated.

3.5.2. Forces acting on the apex seal

From the position expressions for points i_1, i_2, s_5, s_6, c_2, and c_4, it is critical to work out the relative velocities between the seal and the rotor, $\vec{v}_{sr} = \vec{v}_s - \vec{v}_r$, at those contact points; as such the frictional and material damping forces can be calculated. The analysis starts below with point i_1, at which the seal velocity can be expressed as

$$\vec{v}_{s_{i_1}} = \vec{v}_{\mathrm{Og}} + \vec{\omega} \times \vec{r}_c + \dot{\vec{r}}_c + (\vec{\omega} + \dot{\vec{\varphi}}) \times \left[(d_{s_0} - l_1)\hat{X}_s - \frac{W_s}{2}\hat{Y}_s\right]$$

[3-48]

where $\vec{v}_{\mathrm{Og}}$ is the velocity of point O_g referred to above. The velocity of point i_1, on the rotor, is

$$\vec{v}_{r_{i_1}} = \vec{v}_{\mathrm{Og}} + \vec{\omega} \times \vec{r}_c + \vec{\omega} \times \left[(d_{s_0} - l_1)\hat{X}_s - \frac{W_s}{2}\hat{Y}_s\right]$$

[3-49]

Hence, the relative velocity of point i_1 can be found from the difference of equations [3-48] and [3-49] as follows:

$$\Delta\vec{v}_{i_1} = \vec{v}_{s_{i_1}} - \vec{v}_{r_{i_1}} = \dot{\vec{r}}_c + \dot{\vec{\varphi}} \times \left[(d_{s_0} - l_1)\hat{X}_s - \frac{W_s}{2}\hat{Y}_s \right] \quad [3\text{-}50]$$

which can be manipulated to give

$$\Delta\vec{v}_{i_1} = \dot{x}\hat{X} + \dot{y}\hat{Y} + \frac{W_s}{2}\dot{\varphi}\hat{X}_s + (d_{s_0} - l_1)\dot{\varphi}\hat{Y}_s \quad [3\text{-}51]$$

From the above equation, the relative velocity of i_1 can be separated into $\hat{X}_s$ and $\hat{Y}_s$ components

$$\Delta\vec{v}_{i_1} \cdot \hat{X}_s = \dot{x}\cos\varphi + \dot{y}\sin\varphi + \frac{W_s}{2}\dot{\varphi} \quad [3\text{-}52]$$

and

$$\Delta\vec{v}_{i_1} \cdot \hat{Y}_s = -\dot{x}\sin\varphi + \dot{y}\cos\varphi + (d_{s_0} - l_1)\dot{\varphi} \quad [3\text{-}53]$$

These components will assist the sign convention of the frictional and damping force, $\vec{F}_{f_{i_1}}$ and $\vec{F}_{d_{i_1}}$, respectively as

$$\gamma_1 = sign(\Delta\vec{v}_{i_1} \cdot \hat{X}_s) \quad [3\text{-}54]$$

and

$$\begin{cases} \vec{F}_{d_{i_1}} = -c_r(\Delta\vec{v}_{i_1} \cdot \hat{Y}_s)\hat{Y}_s & if \quad (\Delta\vec{v}_{i_1} \cdot \hat{Y}_s) < 0 \\ \vec{F}_{d_{i_1}} = \vec{0} & otherwise \end{cases} \quad [3\text{-}55]$$

where c_r is the equivalent damping coefficient of the seal-groove material.

Likewise, relative velocities of points $c_2, c_4,$ and i_2 of the seal with respect to the groove can be determined. For point c_2:

$$\Delta\vec{v}_{c_2} = \vec{v}_{s_{c_2}} - \vec{v}_{r_{c_2}} = \dot{\vec{r}}_c - \dot{\vec{\varphi}} \times \left[d_{s_2}\hat{X}_s + \frac{W_s}{2}\hat{Y}_s \right]$$

[3-56]

Which can be simplified as,

$$\Delta\vec{v}_{c_2} = \dot{x}\hat{X} + \dot{y}\hat{Y} + \frac{W_s}{2}\dot{\varphi}\hat{X}_s - d_{s_2}\dot{\varphi}\hat{Y}_s$$

[3-57]

For point c_4:

$$\Delta\vec{v}_{c_4} = \vec{v}_{s_{c_4}} - \vec{v}_{r_{c_4}} = \dot{\vec{r}}_c + \dot{\vec{\varphi}} \times \left[-d_{s_2}\hat{X}_s + \frac{W_s}{2}\hat{Y}_s \right]$$

[3-58]

Which can be simplified as follows,

$$\Delta\vec{v}_{c_4} = \dot{x}\hat{X} + \dot{y}\hat{Y} - \frac{W_s}{2}\dot{\varphi}\hat{X}_s - d_{s_2}\dot{\varphi}\hat{Y}_s$$

[3-59]

For point i_2:

$$\Delta\vec{v}_{i_2} = \vec{v}_{s_{i_2}} - \vec{v}_{r_{i_2}} = \dot{\vec{r}}_c + \dot{\vec{\varphi}} \times \left[(d_{s_0} - l_3)\hat{X}_s + \frac{W_s}{2}\hat{Y}_s \right]$$

[3-60]

Which can be simplified as follows;

$$\Delta\vec{v}_{i_2} = \dot{x}\hat{X} + \dot{y}\hat{Y} - \frac{W_s}{2}\dot{\varphi}\hat{X}_s + (d_{s_0} - l_3)\dot{\varphi}\hat{Y}_s$$

[3-61]

From equations [3-57], [3-59], and [3-61], the sign convention of the frictional and damping forces at those points can be found by utilising the following expressions

$$\begin{cases} \begin{cases} \gamma_2 = sign\left(\Delta\vec{v}_{c_2} \cdot \hat{X}\right) \\ \begin{cases} \vec{F}_{d_{c_2}} = -c_r\left(\Delta\vec{v}_{c_2} \cdot \hat{Y}\right)\hat{Y} & if \quad \left(\Delta\vec{v}_{c_2} \cdot \hat{Y}\right) < 0 \\ \vec{F}_{d_{c_2}} = \vec{0} & otherwise \end{cases} \end{cases} \\ \begin{cases} \gamma_3 = sign\left(\Delta\vec{v}_{i_2} \cdot \hat{X}_s\right) \\ \begin{cases} \vec{F}_{d_{i_2}} = -c_r\left(\Delta\vec{v}_{i_2} \cdot \hat{Y}_s\right)\hat{Y}_s & if \quad \left(\Delta\vec{v}_{i_2} \cdot \hat{Y}_s\right) > 0 \\ \vec{F}_{d_{i_2}} = \vec{0} & otherwise \end{cases} \end{cases} \\ \begin{cases} \gamma_4 = sign\left(\Delta\vec{v}_{c_4} \cdot \hat{X}\right) \\ \begin{cases} \vec{F}_{d_{c_4}} = -c_r\left(\Delta\vec{v}_{c_4} \cdot \hat{Y}\right)\hat{Y} & if \quad \left(\Delta\vec{v}_{c_4} \cdot \hat{Y}\right) > 0 \\ \vec{F}_{d_{c_4}} = \vec{0} & otherwise \end{cases} \end{cases} \end{cases}$$

[3-62]

The four side contact forces which correspond to the g_i locations can now be expressed as follows:

$$\begin{cases} \vec{F}_{i_1} = \vec{F}_{g_1} + \vec{F}_{d_{i_1}} \\ \vec{F}_{c_2} = \vec{F}_{g_2} + \vec{F}_{d_{c_2}} \\ \vec{F}_{i_2} = \vec{F}_{g_3} + \vec{F}_{d_{i_2}} \\ \vec{F}_{c_4} = \vec{F}_{g_4} + \vec{F}_{d_{c_4}} \end{cases}$$

[3-63]

At point s_5, where the seal touches the machine housing, the seal velocity can be expressed as

$$\vec{v}_{s_{s_5}} = \vec{v}_{\mathrm{Og}} + \vec{\omega} \times \vec{r}_c + \dot{\vec{r}}_c + \left(\vec{\omega} + \dot{\vec{\varphi}}\right) \times \left[\left(d_{s_1} - a_o\right)\hat{X}_s + b_5\hat{Y}_s\right]$$

[3-64]

This velocity can be re-written as follows,

$$\vec{v}_{s_{s_5}} = (2r\omega\cos\theta + \dot{x} - \omega y)\hat{X} + (\dot{y} + 2r\omega\sin\theta + \omega L_i + \omega x)\hat{Y} - (\omega + \dot{\varphi})b_5\hat{X}_s + (\omega + \dot{\varphi})\left(d_{s_1} - a_o\right)\hat{Y}_s$$

[3-65]

which can be rewritten in terms of $\hat{X}$ and $\hat{Y}$ as

$$\vec{v}_{s_{s_5}} = \left[2r\omega\cos\theta + \dot{x} - \omega y - (\omega + \dot{\varphi})\left(\left(d_{s_1} - a_o\right)\sin\varphi + b_5\cos\varphi\right)\right]\hat{X} + \left[\dot{y} + 2r\omega\sin\theta + \omega(L_i + x) + (\omega + \dot{\varphi})\left(\left(d_{s_1} - a_o\right)\cos\varphi - b_5\sin\varphi\right)\right]\hat{Y}$$

[3-66]

The $\hat{X}$ component of the seal velocity at point s_5 shown in equation [3-66] will determine the sign convention and magnitude of the damping force from the machine housing, $F_{d_{s_5}}$. Such a condition can be expressed as

$$\begin{cases} \vec{F}_{d_{s_5}} = -c_w\left(\vec{v}_{s_{s_5}} \cdot \hat{X}\right)\hat{X} & if\ \left(\vec{v}_{s_{s_5}} \cdot \hat{X}\right) > 0 \\ \vec{F}_{d_{s_5}} = \vec{0} & otherwise \end{cases}$$

[3-67]

where c_w is the wall damping coefficient. As pointed out previously, if the value of Δx_{s_5} is positive ($\Delta x_{s_5} > 0$), the seal and the housing wall come into contact, hence, there exists a contact force at point s_5, $\vec{F}_{s_5}$. Furthermore, if the magnitude of relative velocity between the seal and housing is positive, the seal also experiences a damping force from the wall. These conditions can be expressed as follows:

Algorithm 3-2: Conditions for the seal-wall contact and damping forces

```
1  Begin
2      if Δx_{s5} > 0 then
3          F_w = k_w Δx_{s5}
4          if (v⃗_{s_{s5}} · X̂) > 0 then
5              F_w = k_w Δx_{s5} + c_w (v⃗_{s_{s5}} · X̂)
6          end if
7      end if
8      F⃗_{s5x} = −F_w X̂
```

9	$\vec{F}_{s_{5y}} = F_w \frac{\tan\lambda - \mu_1}{1+\mu_1 \tan\lambda} \hat{Y}$
10	***End***

The force acting on the seal at point s_5, $\vec{F}_{s_5}$, and the moment $\vec{M}_{s_5}$ about centre of gravity can now be expressed as:

$$\begin{cases} \vec{F}_{s_5} = \vec{F}_{s_{5x}} + \vec{F}_{s_{5y}} \\ \vec{M}_{s_5} = \vec{r}_{s_5} \times \vec{F}_{s_5} \end{cases}$$

[3-68]

Similarly, at point s_6 the seal and groove velocities are given, respectively, as follows:

$$\begin{cases} \vec{v}_{s_{s_6}} = \vec{v}_{\mathrm{Og}} + \vec{\omega} \times \vec{r}_c + \dot{\vec{r}}_c + (\vec{\omega} + \dot{\vec{\varphi}}) \times \left[-d_{s_2} \hat{X}_s - \left(\frac{W_s}{2} - b_6 \right) \hat{Y}_s \right] \\ \vec{v}_{r_{s_6}} = \vec{v}_{\mathrm{Og}} + \vec{\omega} \times \vec{r}_c + \vec{\omega} \times \left[-d_{s_2} \hat{X}_s - \left(\frac{W_s}{2} - b_6 \right) \hat{Y}_s \right] \end{cases}$$

[3-69]

Hence, the relative velocity of the seal with respect to the groove can be calculated as

$$\Delta\vec{v}_{s_6} = \vec{v}_{s_{s_6}} - \vec{v}_{r_{s_6}} = \dot{\vec{r}}_c - \dot{\vec{\varphi}} \times \left[d_{s_2} \hat{X}_s + \left(\frac{W_s}{2} - b_6 \right) \hat{Y}_s \right]$$

[3-70]

This velocity is simplified as follows,

$$\Delta\vec{v}_{s_6} = \dot{x}\hat{X} + \dot{y}\hat{Y} + \dot{\varphi} \left(\frac{W_s}{2} - b_6 \right) \hat{X}_s - \dot{\varphi} d_{s_2} \hat{Y}_s$$

[3-71]

Which can be expressed in terms of $\hat{X}$ and $\hat{Y}$ components as

$$\Delta\vec{v}_{s_6} = \left[\dot{x} + \dot{\varphi} d_{s_2} \sin\varphi + \dot{\varphi} \left(\frac{W_s}{2} - b_6 \right) \cos\varphi \right] \hat{X} + \left[\dot{y} - \dot{\varphi} d_{s_2} \cos\varphi + \dot{\varphi} \left(\frac{W_s}{2} - b_6 \right) \sin\varphi \right] \hat{Y}$$

[3-72]

The friction and damping forces, $F_{f_{s_6}}$ and $F_{d_{s_6}}$, can be determined from the following conditions

$$\begin{cases} \begin{cases} \vec{F}_{d_{s_6}} = -c_s(\Delta\vec{v}_{s_6} \cdot \hat{X})\hat{X} & if \quad (\Delta\vec{v}_{s_6} \cdot \hat{X}) < 0 \\ \vec{F}_{d_{s_6}} = \vec{0} & otherwise \end{cases} \\ \vec{F}_{f_{s_6}} = -sign(\Delta\vec{v}_{s_6} \cdot \hat{Y})\mu_s \left(F_{sp} - c_s(\Delta\vec{v}_{s_6} \cdot \hat{X})\right)\hat{Y} \end{cases}$$

[3-73]

where c_s is the damping coefficient near the seal-spring contact point,

μ_s is the friction coefficient between the spring and seal.

The force acting on the seal at point s_6, $\vec{F}_{s_6}$, and the moment $\vec{M}_{s_6}$ about centre of gravity can now be expressed as:

$$\begin{cases} \vec{F}_{s_6} = F_{sp}\,\hat{X} + \vec{F}_{d_{s_6}} + \vec{F}_{f_{s_6}} \\ \vec{M}_{s_6} = \vec{r}_{s_6} \times \vec{F}_{s_6} \end{cases}$$

[3-74]

Having calculated the contact forces acting on the seal, it remains to calculate the pressure forces as shown in the next section.

3.5.3. Forces exerted on the apex seal by pressure from the chambers

Pressure from the machine's chamber above and below the rotor chord, P_a and P_b, will result in forces acting on the seal at points $s_1, s_2, s_3,$ and s_4; the force caused by pressure within the gaps between the seal and the seal groove will act on point s_7; the pressure forces from the chambers act on the seal tips on point s_8 and s_9. These forces, shown in Figure 3-6, can be expressed as follows:

$$\begin{cases} \vec{F}_{s_1} = P_b A_{s_1} \hat{Y}_s \\ \vec{F}_{s_2} = P_{s_2} A_{s_2} \hat{Y}_s \\ \vec{F}_{s_3} = -P_a A_{s_3} \hat{Y}_s \\ \vec{F}_{s_4} = -P_{s_4} A_{s_4} \hat{Y}_s \\ \vec{F}_{s_7} = P_{end} A_{s_7} \hat{X}_s \\ \vec{F}_{s_8} = P_b A_{s_8} \hat{f}_{s_8} \\ \vec{F}_{s_9} = P_a A_{s_9} \hat{f}_{s_9} \end{cases}$$

[3-75]

where $\hat{f}_{s_8}$ and $\hat{f}_{s_9}$ are unit vectors along the lines of action of their corresponding forces, and the areas of various sections are given as

$$\begin{cases} A_{s_1} = l_1 B_s \\ A_{s_2} = l_2 B_s \\ A_{s_3} = l_3 B_s \\ A_{s_4} = l_4 B_s \\ A_{s_7} = W_s B_s \\ A_{s_8} = 2r_o \sin\left(\dfrac{\beta_o + \beta}{2}\right) B_s \\ A_{s_9} = 2r_o \sin\left(\dfrac{\beta_o - \beta}{2}\right) B_s \end{cases}$$

[3-76]

B_s in equation [3-76] is the seal depth measured perpendicular to the XY plane. Of note is that the pressure P_{end} is assumed to be half that of the difference of P_a and P_b, and the pressures P_{s_2} and P_{s_4} will depend on the seal-groove relative positions. The pressure forces $\vec{F}_{s_8}$ and $\vec{F}_{s_9}$ act on points s_8 and s_9 respectively. These points can be expressed in the $X_s Y_s$ frame as:

$$\begin{aligned} \vec{r}_{s_8} &= \left(d_{s_1} - r_o\right)\hat{X}_s + r_o e^{j\left(\frac{\beta - \beta_o}{2}\right)} \\ &= \left(d_{s_1} - r_o + r_o \cos\left(\frac{\beta - \beta_o}{2}\right)\right)\hat{X}_s + r_o \sin\left(\frac{\beta - \beta_o}{2}\right)\hat{Y}_s \end{aligned}$$

[3-77]

and

$$\vec{r}_{s_9} = (d_{s_1} - r_o)\hat{X}_s + r_o e^{j\left(\frac{\beta+\beta_o}{2}\right)}$$
$$= \left(d_{s_1} - r_o + r_o \cos\left(\frac{\beta+\beta_o}{2}\right)\right)\hat{X}_s + r_o \sin\left(\frac{\beta+\beta_o}{2}\right)\hat{Y}_s$$

[3-78]

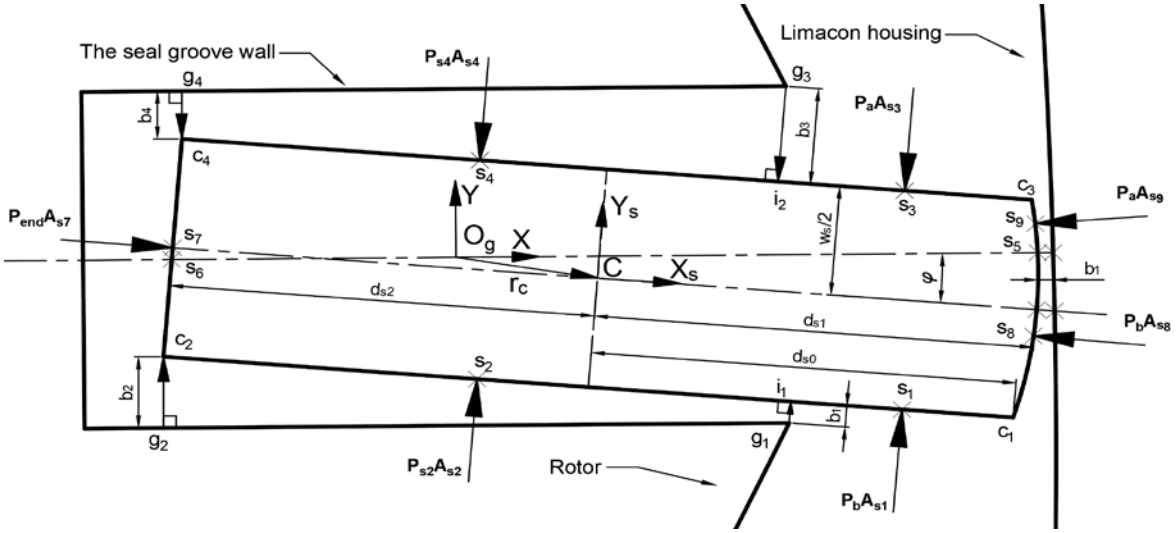

Figure 3-6: Forces acting by pressures from the chambers

At this stage, the moments of the above pressure forces about the seal centre of gravity can be expressed in the vector from as

$$\begin{cases} \vec{M}_{s_1} = \left[\left(d_{s_0} - \frac{l_1}{2}\right)\hat{X}_s - \frac{W_s}{2}\hat{Y}_s\right] \times \vec{F}_{s_1} \\ \vec{M}_{s_2} = \left[\left(\frac{l_2}{2} - d_{s_2}\right)\hat{X}_s - \frac{W_s}{2}\hat{Y}_s\right] \times \vec{F}_{s_2} \\ \vec{M}_{s_3} = \left[\left(d_{s_0} - \frac{l_3}{2}\right)\hat{X}_s + \frac{W_s}{2}\hat{Y}_s\right] \times \vec{F}_{s_3} \\ \vec{M}_{s_4} = \left[\left(\frac{l_4}{2} - d_{s2}\right)\hat{X}_s + \frac{W_s}{2}\hat{Y}_s\right] \times \vec{F}_{s_4} \\ \vec{M}_{s_7} = -d_{s_2}\hat{X}_s \times \vec{F}_{s_7} \end{cases}$$

[3-79]

The pressure and contact forces acting on the seal and their moments about the seal centre of gravity can now be expressed in a general equation of motion as follows;

$$\begin{bmatrix} m_s & 0 & 0 \\ 0 & m_s & 0 \\ 0 & 0 & I_{CG} \end{bmatrix} \begin{bmatrix} \ddot{X}_1 \\ \ddot{Y}_1 \\ \ddot{\varphi} \end{bmatrix} = \begin{bmatrix} \sum F_x \\ \sum F_y \\ \sum M_{CG} \end{bmatrix} \quad [3\text{-}80]$$

where $\ddot{X}_1$ and $\ddot{Y}_1$ are defined in equation [3-15] and $\ddot{\varphi}$ is the angular acceleration of the seal,

m_s is the seal's mass and I_{CG} is its mass moment of inertia about the centre of gravity,

$\sum F_x$ is the sum of forces acting on the seal in the x-direction

$\sum F_y$ is the sum of forces acting on the seal in the y-direction

$\sum M_{CG}$ is the sum of moments acting on the seal about its centre of gravity.

At every rotor angle, θ, the three non-linear simultaneous differential equations given in [3-80] are solved numerically to find the seal displacements, being x, y and φ.

3.5.4. Possible seal-groove interactions

As pointed out by Phung and Sultan (2017), the interactions between the seal and seal groove can be categorised into nine different cases. To differentiate between the cases, seal-groove contact points have been numbered as shown in Figure 3-3. Points n, p and q respectively represent the negative, neutral, and positive sides of the seal groove inner end; while points 1, 2, and 3 represent the negative, neutral, and positive sides of the seal groove outer end, respectively. The negative side of the groove is on the negative side of the negative side of Y_1 axis, while positive side of the groove is on the positive side of Y_1 axis. The two imaginary points 2 and p, point 2 sits between points 1 and 3 while point p sits between points n and q, are also shown in Figure 3-3 above. The seal cases can now be categorised by a letter, which represents the position of back-contact point, followed by a number, which represents the position of front contact point. i.e.:

Case q1 is when the top left-hand corner of the seal contacts with the positive side of the groove, denoted q, and the negative side of the seal contacts with the negative inner side of the groove modified apex, denoted 1, as shown in Figure 3-7a. Of note is that back-contact happens when the back corner of the seal contacts with the groove surface; front-contact is when either the negative or positive side of the seal comes into contact with the inner side of the modified apex. The nine seal-groove interaction cases are shown below.

Case q1: two-point contact, seal tilting right (Figure 3-7a) occurs when $\begin{cases} b_1 \leq 0 \\ b_2 > 0 \\ b_3 > 0 \\ b_4 \leq 0 \end{cases}$; and

Case n3: two-point contact, seal tilting left (Figure 3-7b) is when $\begin{cases} b_1 > 0 \\ b_2 \leq 0 \\ b_3 \leq 0 \\ b_4 > 0 \end{cases}$. In these two cases, there are two points of contact between the seal and the seal groove. Different values of b_1, b_2, b_3, and b_4 determine the seal tilting directions.

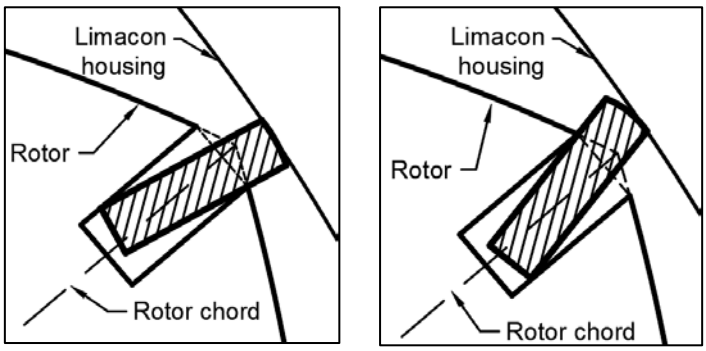

a) b)

Figure 3-7: Seal-groove interactions: a) Case q1, b) Case n3

The common factor of Case p1 (Figure 3-8a), Case n2 (Figure 3-8b), Case p3 (Figure 3-8c), and Case q2 (Figure 3-8d) is that between the seal and the seal groove exists only one contact point. This contact point can either be back-contact or front-contact. The conditions that determine these contact cases are shown in Figure 3-8 and the Algorithm 3-3 below.

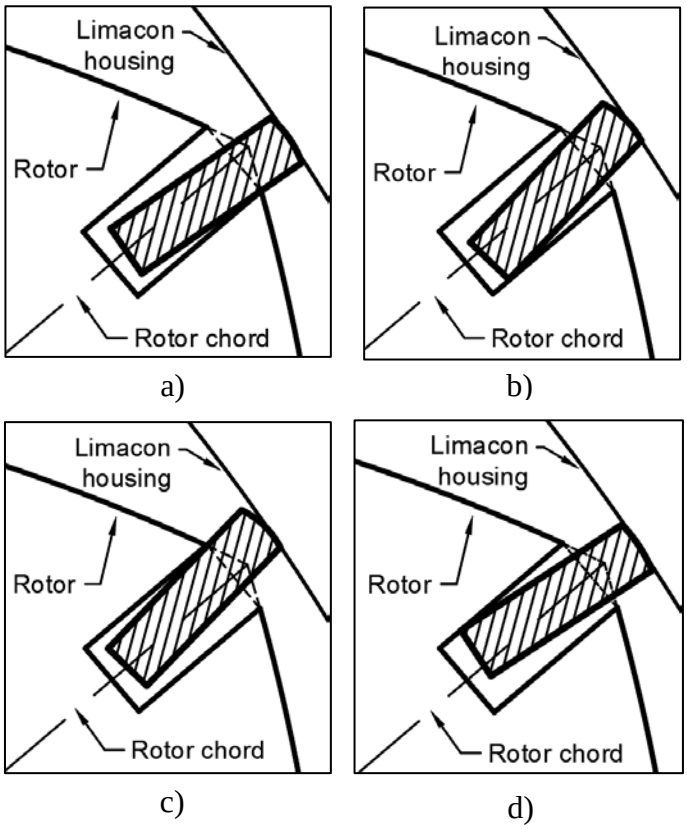

Figure 3-8: Seal-groove interactions: a) Case p1, b) Case n2, c) Case p3, d) Case q2

Algorithm 3-3: Conditions to determine the seal-groove contact cases

```
1   Begin
2       if (b1 ≤ 0 &b2 > 0 & b3 > 0 & b4 > 0) then
3           Case = Case p1
4       end if
5       if (b1 > 0 & b2 ≤ 0 & b3 > 0 & b4 > 0) then
6           Case = Case n2
7       end if
8       if (b1 > 0 & b2 > 0 & b3 ≤ 0 & b4 > 0) then
9           Case = Case p3
10      end if
11      if (b1 > 0 & b2 > 0 & b3 > 0 & b4 ≤ 0) then
12          Case = Case q2
13      end if
14  End
```

Case q3 happens when the positive side of the seal contacts with the positive side of the groove, as shown in Figure 3-9a. The conditions for this case to happen are $\begin{cases} b_1 > 0 \\ b_2 > 0 \\ b_3 \leq 0 \\ b_4 \leq 0 \end{cases}$.

Similarly, Figure 3-9b shows that when $\begin{cases} b_1 \leq 0 \\ b_2 \leq 0 \\ b_3 > 0 \\ b_4 > 0 \end{cases}$ the seal-groove interaction falls under Case n1.

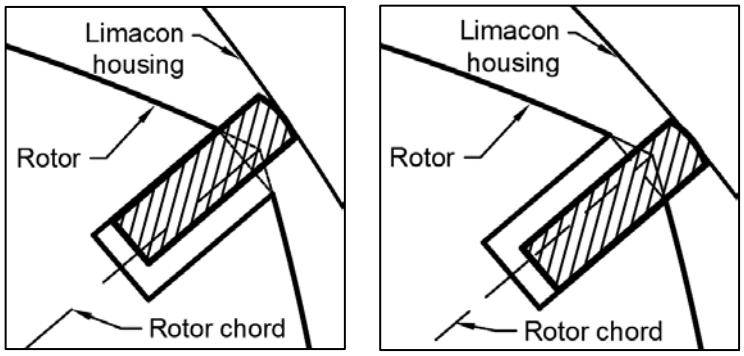

Figure 3-9: Seal-groove interactions: a) Case q3, b) Case n1

Another special case, Case p2, occurs when there is no actual contact between the seal and the seal groove. The seal floats within the groove as shown in Figure 3-10. In this case, values of $b_1, b_2, b_3,$ and b_4 are $\begin{cases} b_1 > 0 \\ b_2 > 0 \\ b_3 > 0 \\ b_4 > 0 \end{cases}$. It is worth pointing out that when the seal-groove relative position falls under Case p2, the gap between the seal and the groove will form a passage and allow working fluid to flow from higher-pressure chamber to lower-pressure one. The leakage through the gap area, $A_{gap} = b_{gap}H$ where b_{gap} is the minimum gap between the seal and the groove and H is the machine depth measured perpendicular to the page, can be included in the thermodynamic performance of the

machine is considered. The distance b_{gap} can be determined from the seal dynamics model and with the aid of Algorithm 3-4 shown below:

Algorithm 3-4: Conditions to determine the seal-groove gap

1 ***Begin***

2 $$\textit{if} \begin{cases} b_1 > 0 \\ b_2 > 0 \\ b_3 > 0 \\ b_4 > 0 \end{cases} \textit{then}$$

3 $b_{gap} = \min(b_1, b_2, b_3, b_4)$

4 ***else*** $b_{gap} = 0$

5 ***end if***

6 ***End***

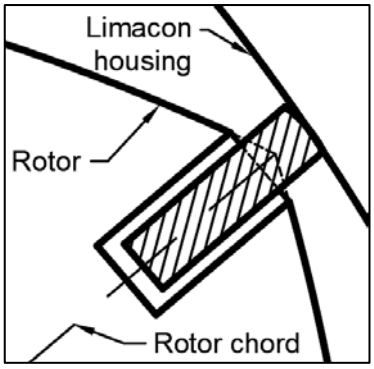

Figure 3-10: Seal-groove interaction Case p2

3.6. Numerical illustration

To validate the reliability of the seal dynamics model presented above, a case study has been considered. In this case study, it is crucial to use the actual upper and lower chamber pressures that the limaçon machine experiences during its operation. The seal response, performance, effectiveness, and leakages, and power loss have been observed from the thermodynamic performance point of view. As such the chamber pressures at different the crank angles, as shown in Figure 3-11, which have been calculated from the thermodynamic model have been utilised. The upper chamber and lower chamber pressures are shown as blue and red graphs, respectively. Of note is that the pressure profiles in the two chambers are similar to each other; due to the distinct shape of the rotor and housing, however, the pressure profiles are π (180^o) different in phase.

In Table 3-1, the key geometries i.e.: angular positions for, angular width, and length of the inlet and outlet ports are shown. The modelled machine has been allowed to run at a constant angular velocity of 1500 rpm so that the seal performance, leakages, seal-

housing friction and damping forces, seal-groove friction and damping forces can be verified. The forces acting on the seal and the seal response at different angular positions of the rotor are shown as polar plots in Figure 3-12; the positions of the inlet and outlet ports are also presented in this figure.

Table 3-1: Geometries of limaçon machine's inlet and outlet ports

	Angular position (degree)	Angular width (degree)	Length (mm)
Inlet port	-25	22	70
Outlet port	140	36	80

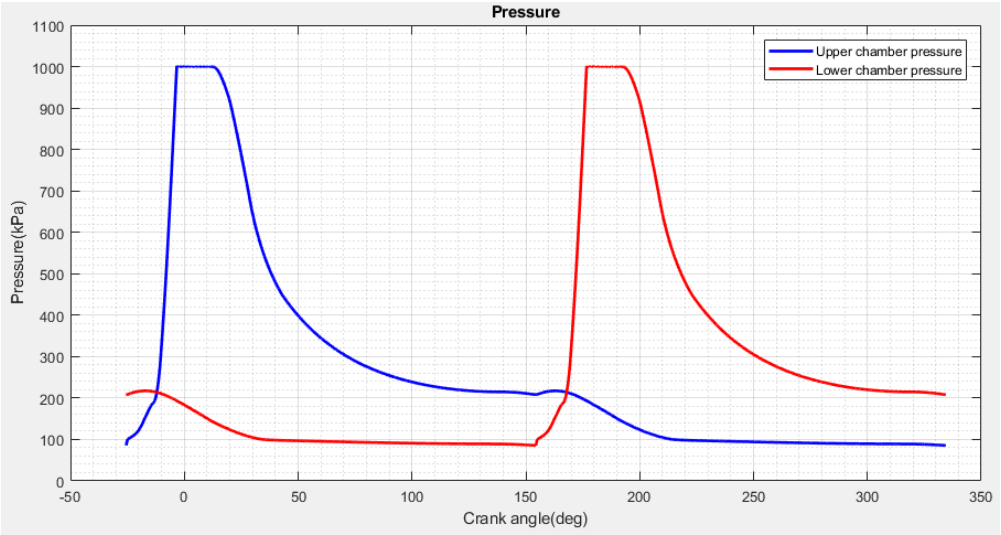

Figure 3-11: The upper and lower chamber pressure profiles for a limaçon machine as functions of the crank angle

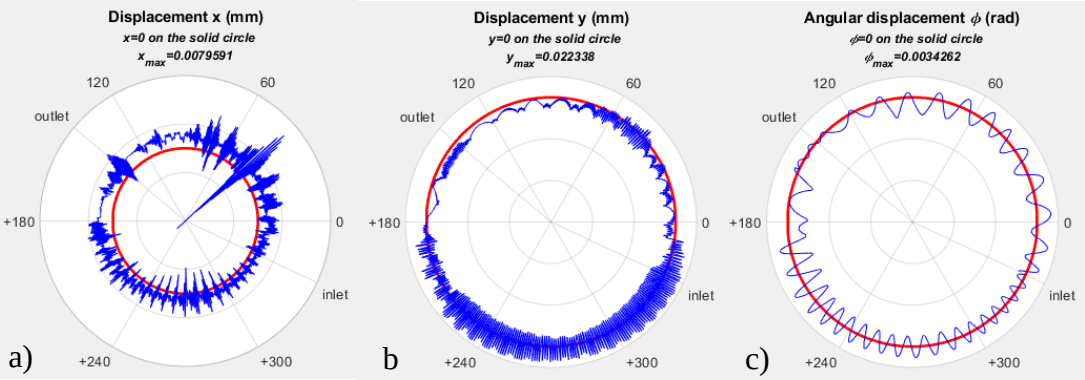

Figure 3-12: Seal linear and angular displacements

Figure 3-12a, Figure 3-12b, and Figure 3-12c show the linear displacements along X and Y axes and the angular displacement, ϕ, of the seal, respectively, during the machine operation. Figure 3-12 also shows the angular position of the machine rotor at which the seal linear and angular displacements occur; this informs the designer locations on the seal groove and the housing that need reinforcing to extend the machine reliability. The forces between the seal and the seal groove walls, $F_{i_1}, F_{i_2}, F_{c_2}$, and F_{c_4}, the spring force, F_{s_6}, due to the seal spring deflection Δx_{s_6}, and the seal-housing contact force, F_{s_5}, are shown in Figure 3-13; these forces can be calculated as demonstrated in section 3.5. Of note is that the initial position of the machine rotor is at the inlet port and the rotor rotates in the counter-clockwise direction. The two sides of the seal are subjected to two different pressures; such differences in pressure directly affect the seal dynamics, which is noticeable in Figure 3-12. As a result of that, it is critical to reinforce the housing at these angular positions and strengthen the contact surface between the seal and the seal groove, to prevent failure during the machine operation and increase the reliability of the limaçon machine.

It is also noticeable that the seal displacement in X direction (Figure 3-12a) is of significant magnitude when the apex seal is approximately at the $\frac{3\pi}{2}$ (270^o) position on the housing. This is due to the geometry of the limaçon machine. Based on Figure 3-1c,

it is apparent that the rotor experiences a sliding motion in the positive X direction in the first quarter of the X_oY_o frame. When the rotor chord approaches the second quarter of the X_oY_o frame, the direction of the sliding motion shifts towards the negative X direction. At this instance, the left-hand side seal is now located at the $\frac{3\pi}{2}$ position on the housing. Due to inertia, the seal tends to move in the positive X direction and dig into the housing wall. This results in substantial seal displacement along X direction, which would require reinforcement to the correspondent section of the housing wall.

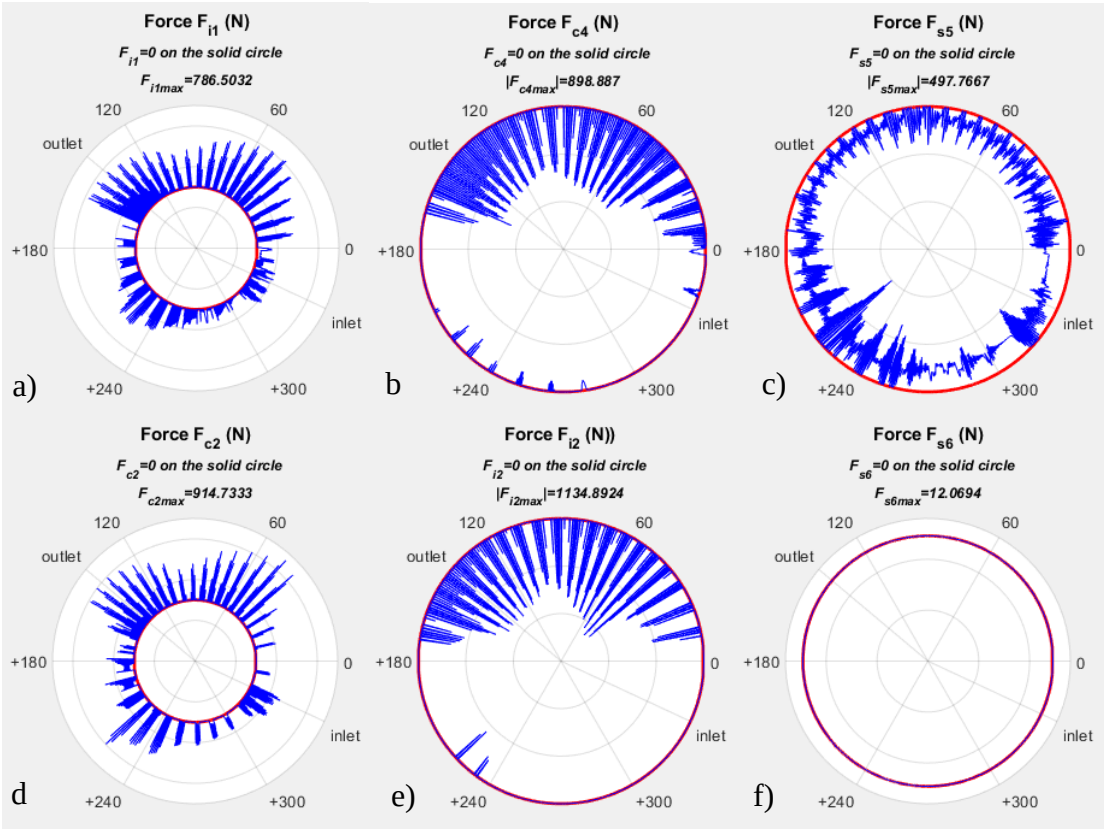

Figure 3-13: Forces acting on the apex seal

From the seal-housing force, F_{s_5}, in time domain, a frequency spectrum has been generated and shown in Figure 3-14. Force, F_{s_5}, is the response of apex seal to the pressure difference between the machine chambers and the rotor rotational motion; the major frequency of the force F_{s_5} centres at around $6 \times 10^4\ rad/s$ follows by smaller peaks at around $0.01 \times 10^4, 0.05 \times 10^4$, and $0.78 \times 10^4\ rad/s$. It is important to avoid

resonance at these frequencies when considering material used for the seal and housing surface, spring stiffness as well as damping coefficient.

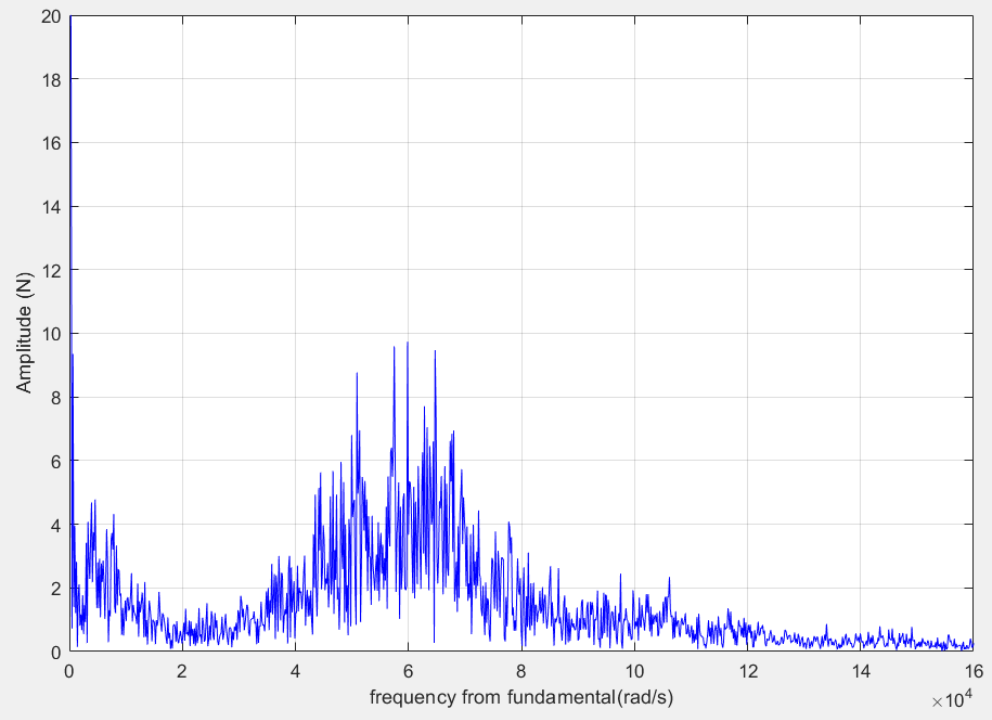

Figure 3-14: Frequency (rad/s) spectrum of the seal-housing force, F_{s_5}

3.7. Conclusion

The paper demonstrated an approach to model the dynamical behaviour of apex seals in a limaçon gas expander. The model uses a spring-damper representation to describe the characteristics of the contact between the seal and the surrounding elements, namely the housing and the rotor apical groove. A detailed mathematical description of the seal kinematics made it possible to calculate the contact forces accurately and hence formulate three nonlinear differential equations for the multi-degree of freedom seal vibration. The variable pressure in the chambers of the gas expanders were accounted for in the differential equations and these were then solved numerically to calculate the seal position and orientation at any angle of the machine rotor. The seal-groove interaction has been categorised into nine distinct cases. Those cases are labelled as two-digit numbers, the

first digit represents seal-groove back-contact position while the second digit shows the front-contact position. This seal dynamical behaviour model can be modified to suit different seal materials, spring and housing surface stiffness, as well as different types of lubrication. A numerical example was presented to confirm the validity of the presented models and their suitability for the problem at hand. The results of the presented example are indeed promising and the models presented in the paper are suitable to incorporate in the thermodynamic model to account for possible leakage past the apex seals and assess the level of surface stresses occurring in the expander housing and apical grooves.

3.8. Nomenclatures

p_1p_2 : limaçon chord

$2L$: limaçon chord length

C : centre of gravity of the seal

X_oY_o : stationary frame

X_rY_r : frame fixed at the centre point of the rotor and moves with it.

X_1Y_1 : rotating frame

$\hat{\imath}, \hat{\jmath}$, and $\hat{k}$: unit vectors of the X_1, Y_1, and Z_1 axes

X_sY_s : the frame attached to the seal centre of gravity with the unit vectors $\hat{Y_s}$ and $\hat{X_s}$

XY : a frame fixed to the groove. Also signifies the initial position of the seal-attached frame (X_sY_s) with unit vectors $\hat{Y}$ and $\hat{X}$

o : limaçon pole

O_g : the seal origin

θ : crank angle

r : radius of the base circle

m : centre point of the chord

R_h : housing radial distance

b : limaçon aspect ratio

H : machine's depth measured perpendicular to the page

ω : rotor angular velocity

L_i : distance from the rotor chord centre point, m, to the seal's centre of gravity

δ_s : initial deflection of seal spring

δ_w : initial deflection of housing due to contact with seal

k_s : spring stiffness

k_w : the equivalent spring stiffness of the limaçon housing wall

c, c_r, c_w, and c_s : damping coefficients (All typed in lowercase)

m_s : mass of the seal

F: force acting on the seal

P_a, P_b: pressure of the chamber above and below the rotor chord, respectively

A_p, A_f: areas of the seal that are exposed to the machine chambers

ρ_s : density of seal material

W_g : width of the seal groove

W_s : width of the seal

d_{si} : seal height $(i = 1, 2, or\ blank)$

C_r : rotor-housing clearance (Uppercase *C*)

z : portion of the rotor apex truncated to machine the seal groove

ζ_o : seal protrusion at the initial position

$x, \dot{x}, \ddot{x}$: seal linear displacement, velocity, and acceleration along X_r-axis

$y, \dot{y}, \ddot{y}$: seal linear displacement, velocity, and acceleration along Y_r-axis

$\varphi, \dot{\varphi}, \ddot{\varphi}$: seal angular displacement, velocity, and acceleration

s_i, c_i, i_i: special points on the apex seal ($i = 1, 2, 3, \dots$)

g_i : points on the seal groove ($i = 1, 2, 3, \dots$)

B_s : seal depth measured perpendicular to XY plane

References

Amrouche, F., Erickson, P., Park, J., & Varnhagen, S. (2014). An experimental investigation of hydrogen-enriched gasoline in a Wankel rotary engine. International Journal Of Hydrogen Energy, 39(16), 8525-8534. http://dx.doi.org/10.1016/j.ijhydene.2014.03.172

Costa, S. I. R., Grou, M. A., Figueiredo, V. (1999). Mechanical curves - a kinematic Greek look through the computer. Int. J. Math. Edu. Sci. Technol., 30(3), 459–469.

Drogosz, P. (2011). Trajectory of the apex seals of the Wankel rotary engine. Journal of KONES Powertrain and Transport, 18(2), 117-122.

Handschuh, R. F., & Owen, A. K. (2010). Analysis of Apex Seal Friction Power Loss in Rotary Engines. NASA Glenn Research Center, Cleveland, Ohio. NASA Technical Memorandum No. 2010-216353.

Lemort, V., Quoilin, S., Cuevas, C., & Lebrun, J. (2009). Testing and modeling a scroll expander integrated into an Organic Rankine Cycle. Applied Thermal Engineering, 29(14-15), 3094-3102. http://dx.doi.org/10.1016/j.applthermaleng.2009.04.013

Matsuura, K., Terasaki, K., & Watanabe, I. (1978). The Behavior of a Rotary Engine Apex Seal against the Trochoidal Surface. Bulletin Of JSME, 21(161), 1642-1651. http://dx.doi.org/10.1299/jsme1958.21.1642

Pennock, G., & Beard, J. (1997). Force analysis of the apex seals in the Wankel rotary compressor including the influence of fluctuations in the crankshaft speed. Mechanism And Machine Theory, 32(3), 349-361. http://dx.doi.org/10.1016/s0094-114x(96)00051-1

Phung, T. H., Sultan, I. A., & Boretti, A. (2016). Design of Limaçon Gas Expanders. In R. N. Jazar, & L. Dai (Eds.), Nonlinear Approaches in Engineering Applications (pp. 91-120). Springer International Publishing Switzerland.

Phung, T. H., & Sultan, I. A., (2017). Apex seal vibration analysis of limaçon positive displacement machines. 9th Australasian Congress on Applied Mechanics (ACAM9), Engineers Australia, Sydney, 595-603. https://search.informit.com.au/documentSummary;dn=394117366088909;res=IELENG, ISBN: 9781925627022.

Picard, M., Tian, T., & Nishino, T. (2015). Predicting Gas Leakage in the Rotary Engine—Part I: Apex and Corner Seals. Journal Of Engineering For Gas Turbines And Power, 138(6), 062503. http://dx.doi.org/10.1115/1.4031873

Picard, M., Tian, T., & Nishino, T. (2015). Predicting Gas Leakage in the Rotary Engine—Part II: Side Seals and Summary. Journal Of Engineering For Gas Turbines And Power, 138(6), 062504. http://dx.doi.org/10.1115/1.4031874

Rose, S., & Yang, D. (2014). Wide and multiple apex seals for the rotary engine. Mechanism And Machine Theory, 74, 202-215. http://dx.doi.org/10.1016/j.mechmachtheory.2013.12.011

Sultan, I. (2005). The Limaçon of Pascal: Mechanical Generation and Utilization for Fluid Processing. Proceedings Of The Institution Of Mechanical Engineers, Part C: Journal Of Mechanical Engineering Science, 219(8), 813-822. http://dx.doi.org/10.1243/095440605x31698

Sultan, I. (2006). Profiling Rotors for Limaçon-to-Limaçon Compression-Expansion Machines. Journal Of Mechanical Design, 128(4), 787-793. http://dx.doi.org/10.1115/1.2202877

Sultan, I. (2007). A surrogate model for interference prevention in the limaçon-to-limaçon machines. Engineering Computations, 24(5), 437-449. http://dx.doi.org/10.1108/02644400710755852

Sultan, I. (2008). A Geometric Design Model for the Circolimaçon Positive Displacement Machine. Journal Of Mechanical Design, 130(6), 062307. http://dx.doi.org/10.1115/1.2901143

Warren, S., & Yang, D. (2013). Design of rotary engines from the apex seal profile (Abbr.: Rotary engine design by apex seal). Mechanism And Machine Theory, 64, 200-209. http://dx.doi.org/10.1016/j.mechmachtheory.2013.01.015

Zhang, S., Liu, J., Zuo, Z., & Zhang, Y. (2017). An analytical investigation of oil film thickness for the apex seal in a small Wankel rotary engine. Tribology International, 116, 383-393. http://dx.doi.org/10.1016/j.triboint.2017.07.031

Zhang, Y., Zuo, Z., Yuan, C., & Wang, D. (2014). Analysis on Performance of Leaf Spring Rotary Engine. Energy Procedia, 61, 984-989. http://dx.doi.org/10.1016/j.egypro.2014.11.1009

Chapter 4: Thermodynamic-based optimisation of the limaçon-to-circular expanders*

4.1. Abstract

Limaçon machine, of which the relative motion between the rotor and housing follows the limaçon curve, belongs to a class of rotary positive displacement machines. The profiles of rotors and housings of those machines can be constructed of either limaçon or circular curves, hence the names: limaçon-to-limaçon (Sultan, 2005), circolimaçon (Sultan, 2008), and limaçon-to-circular machines (Phung, Sultan, & Boretti, 2016). This paper presents the investigation into the thermodynamic performance of the limaçon-to-circular machines with the presence of apex seals and inlet valve.

This paper sets out by briefly introducing the limaçon technology and the construction of the limaçon-to-circular machine working volume. The mathematical descriptions of ports' positions and areas have also been introduced. The paper then discusses the flow and phase composition of working fluid through the working chambers as well as how the fluid velocity is modelled and calculated. Then the seal dynamic model and response of inlet valve are presented followed by the machine thermodynamic model. A case study has also been presented to show the responses of seals and inlet valve during the machine operation.

Keywords: Rotary machine; limaçon-to-circular; limaçon machine; limaçon motion; pump; gas expander; compressor; positive displacement; optimisation; thermodynamics.

Article type: Research paper

* This chapter has been submitted to will be submitted to Journal of Engineering for Gas Turbines and Power for publication

4.2. Introduction

Over the past years, the consumption of fossil fuel continues to grow (International Energy Agency, 2015; Department of Industry and Science, 2015) due to the increase in energy demand in both heat and electricity forms. The growth in non-renewable resource consumption together with the low efficiency of the current energy conversion processes result in enormous amount of excess heat is wasted and more greenhouse gas makes its way to the atmosphere. The energy generating activities are definitely key factors that drive the changes in our climate system and escalating risk for different aspect of life (IPCC, 2015; Climate Council, 2015).

From both the environmental and the technological point of view, it is essential to reduce the consumption of non-renewable resources by increasing the efficiency of energy conversion processes as a short-term strategy. The process efficiency can be increased by means of heat recuperation – a practice that captures the previously overlooked waste heat to produce extra mechanical or electrical power. Organic Rankine Cycle (ORC) based micro power plants that utilise organic fluids to transfer heat and expand in the expander to give off work are often employed (Mathias, Johnston, Cao, Priedeman, & Christensen, 2009). Due to the relatively low temperature of low-grade heat, components of ORC micro power plants are often exposed to multi-phase flow; such a condition allows fluid droplets to be formed, which is not suitable for turbine technology. Lemort et al. (2009) and Sultan and Schaller (2011; 2012) in their published work have pointed out that the perfect candidates for low working fluid temperature, multi-phase flow, and low flow rate conditions are positive displacement machines, which include different embodiments of limaçon machines.

This paper investigates the output power and the efficiency of the limaçon-to-circular machine. A mathematical model has been developed based on the thermodynamic

performance, seal dynamic, and inlet valve dynamic of such a machine. A case study has been presented to test the reliability of such a model.

4.3. The limaçon-to-circular machine's working volume

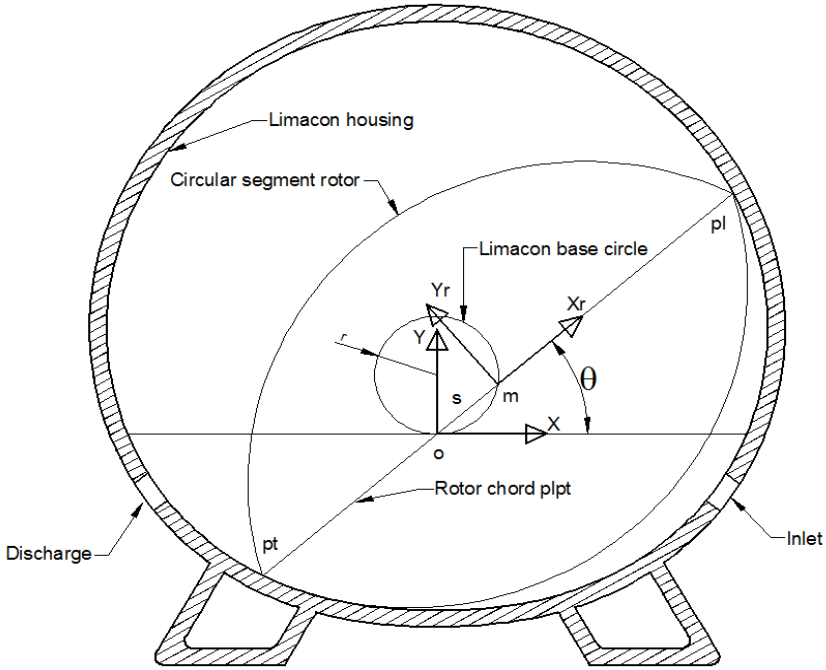

Figure 4-1: A limaçon-to-circular expander

Detailed in Figure 4-1 is a limaçon-to-circular machine and its geometrical aspects. As shown in the figure, the limaçon chord, $p_l p_t$, whose length is $2L$ is allowed to rotate and slide about the limaçon pole, o, which is the origin of a stationary frame XY. The profile of the limaçon housing is formed by the trace of the apices, p_l or p_t. Additionally, another frame namely $X_r Y_r$ is firmly attached to the rotor chord at its centre point, m, and moves with the chord. The angle θ measured from X-axis to X_r-axis followed the right-hand sense is the angular displacement of the machine rotor. When the rotor is in motion, its centre point, m, stays kinematically attached to the base circle of radius, r. It is worth noticing that, the two lobes of such a limaçon-to-circular machine is constructed of two circular segments of radius, R, which take the chord, $p_l p_t$, as the mirror line; hence, the machine received the name limaçon-to-circular machine. Phung et al. (2016) have pointed

out that the housing and rotor of such a machine have distinct profiles (i.e.: limaçon housing, circular segment rotor) and the rotation of the rotor inside the housing follows the limaçon housing; therefore, during operations this machine may encounter rotor-housing interference. As such, Phung et al. (2016) have introduced a clearance value, C, to their calculation to yield the value of R as follows:

$$R = (1 - C_L)\sqrt{L^2 + \frac{4r^2a^2}{1 - 4b^2}} \quad [4\text{-}1]$$

where $0 < b = \frac{r}{L} = 0.25$ is the limaçon aspect ratio, $a > 1$, and $C_L = \frac{C}{L}$. Consequently, the volume of the working chamber below the rotor chord, V_{net}, at any rotor angle, θ, can be expressed as follows:

$$V_{net\_b} = HL^2\left\{\left[\left(b^2 + \frac{1}{2}\right)\pi - 4b\cos\theta\right] - (1 - C_L)\left[\tan^{-1}\left(\frac{\sqrt{1 - 4b^2}}{2ab}\left(1 + \frac{4a^2b^2}{1 - 4b^2}\right)\right) - \frac{2ab}{\sqrt{1 - 4b^2}}\right]\right\} \quad [4\text{-}2]$$

where H is the expander's housing depth measured perpendicular to the page.

The next section introduces a model to calculate the instantaneous port area of the limaçon-to-circular machine as seen from the working chamber.

4.4. Inlet and outlet ports' cross-sectional areas calculation

Sultan and Schaller (2011) have developed a concept to calculate the cross-sectional areas of the inlet and outlet ports of the limaçon-to-limaçon machine. The proposed concept treats both ports without discrimination; hence, no specific reference has been

made to either port. As such, this paper will employ the similar approach to calculate the port areas for the limaçon-to-circular machine.

The radial positions of the port leading and trailing edges are defined by the two position vectors, $\boldsymbol{R}_l$ and $\boldsymbol{R}_t$, which are described in Figure 4-2. The leading edge is defined as the one that the rotor chord leading apex, p_l, meets first during one cycle of operation. These port edges vectors $\boldsymbol{R}_l$ and $\boldsymbol{R}_t$, can be expressed as follows:

$$\begin{cases} \boldsymbol{R}_l = L(2b\sin\theta_l + 1)\widehat{\boldsymbol{R}}_l \\ \boldsymbol{R}_t = L(2b\sin\theta_t + 1)\widehat{\boldsymbol{R}}_t \end{cases} \quad [4\text{-}3]$$

where θ_l is the leading edge angle, θ_t is the trailing edge angle, $\widehat{\boldsymbol{R}}_l = \begin{bmatrix} \cos\theta_l \\ \sin\theta_l \\ 0 \end{bmatrix}$ and $\widehat{\boldsymbol{R}}_t = \begin{bmatrix} \cos\theta_t \\ \sin\theta_t \\ 0 \end{bmatrix}$ are the unit vectors.

The angular location of the leading edge, $\theta_l < \frac{\pi}{2}$, is defined first, followed by the port angular width, $\Delta\theta_p$. Hence, the angular position of the trailing edges can be calculated as: $\theta_t = \theta_l + \Delta\theta_p$. The port length, L_p, is given within the condition bounded by the rotor depth, H, in which $L_p < H$. The port width, W, is calculated from the two edges vectors, $\boldsymbol{R}_l$ and $\boldsymbol{R}_t$, as:

$$W = |\boldsymbol{R}_l - \boldsymbol{R}_t| \quad [4\text{-}4]$$

In this paper, the authors have utilised the semicircular shape for the port ends as described in Figure 4-2; hence, the full cross-sectional area of the port, A_f, can be calculated as follows:

$$A_f = L_p W - W^2\left(1 - \frac{\pi}{4}\right)$$

[4-5]

In order to study the rotor-port interaction, which is the relation between the leading apex of the rotor and the port edges, the position of the rotor leading and trailing edges are defined as follows:

$$\begin{cases} \boldsymbol{P}_l = L(2b\sin\theta + 1)\widehat{\boldsymbol{X}}_r \\ \boldsymbol{P}_t = L(2b\sin\theta - 1)\widehat{\boldsymbol{X}}_r \end{cases}$$

[4-6]

where $\widehat{\boldsymbol{X}}_r = \begin{bmatrix} \cos\theta \\ \sin\theta \\ 0 \end{bmatrix}$ is a unit vector along the rotor chord, which is shown in Figure 4-2.

The relative locations of the rotor leading apex with respect to the port edges can now be defined using the two scalar quantity, s_l and s_t, as follows:

$$\begin{cases} s_l = \left(\widehat{\boldsymbol{R}}_l \times \widehat{\boldsymbol{X}}_r\right) \cdot \left(\widehat{\boldsymbol{X}}_r \times \widehat{\boldsymbol{Y}}_r\right) \\ s_t = \left(\widehat{\boldsymbol{R}}_t \times \widehat{\boldsymbol{X}}_r\right) \cdot \left(\widehat{\boldsymbol{X}}_r \times \widehat{\boldsymbol{Y}}_r\right) \end{cases}$$

[4-7]

where $\widehat{\boldsymbol{Y}}_r = \begin{bmatrix} -\sin\theta \\ \cos\theta \\ 0 \end{bmatrix}$ is a unit vector along the axis perpendicular to the rotor chord (Figure 4-2).

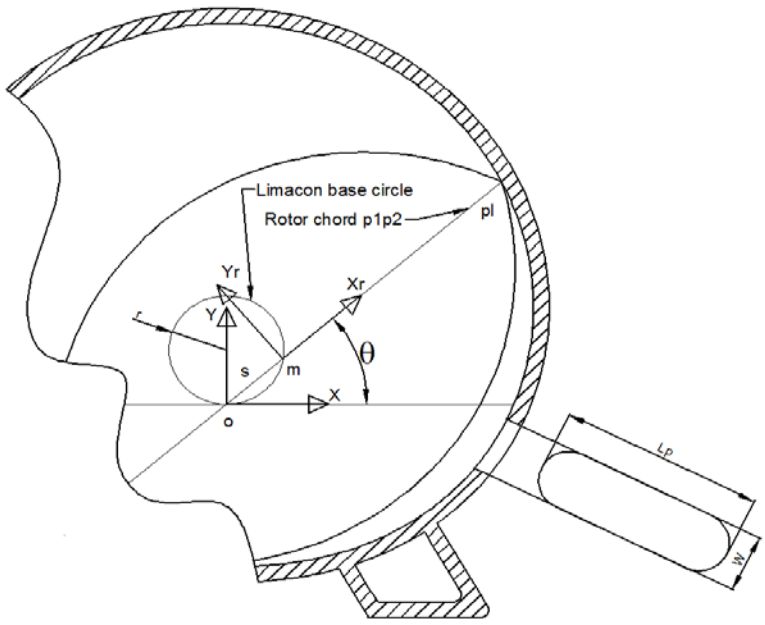

Figure 4-2: The limaçon-to-circular port area

The port areas can now be determined from one of the following four cases:

- Case 1: when $s_l \geq 0$ and $s_t \geq 0$, it is suggested that the port is fully open to the control volume. In this case the port instantaneous area, A_p, can be set equal to the full area, A_f.
- Case 2: when $s_l \geq 0$ and $s_t < 0$, it is suggested that the port is being progressively opened to the control volume. In this case the port area, A_p, can be approximated using the equation $A_p = A_f \frac{|\boldsymbol{P}_l - \boldsymbol{R}_l|}{W}$.
- Case 3: when $s_l < 0$ and $s_t \geq 0$, it is suggested that the port is being progressively shut off from the control volume. In this case the port area, A_p, can be approximated using the equation $A_p = A_f \frac{|\boldsymbol{P}_t - \boldsymbol{R}_t|}{W}$.
- Case 4: when $s_l > 0$ and $s_t < 0$, it is suggested that the port is totally shut off from the control volume. The port area, A_p, in this case is equal to zero (i.e.: $A_p = 0$).

The above four cases of the port areas can be summarised as follows:

$$\begin{cases} if\ s_l \geq 0\ and \begin{cases} s_t \geq 0\ then\ A_p = A_f \\ s_t < 0\ then\ A_p = A_f \dfrac{|\boldsymbol{P}_l - \boldsymbol{R}_l|}{W} \end{cases} \\ if\ s_l < 0\ and \begin{cases} s_t \geq 0\ then\ A_p = A_f \dfrac{|\boldsymbol{P}_t - \boldsymbol{R}_t|}{W} \\ s_t < 0\ then\ A_p = 0 \end{cases} \end{cases}$$

[4-8]

The velocity of fluid flow through the port will be studied in the next section.

4.5. Fluid velocity through ports

The flow of the working fluid through the ports of the limaçon machine encounters a sudden expansion and a change in direction, this type of flow is similar to that of the

globe valves; therefore, these limaçon-to-circular machines' ports can be approximated as globe valves rather than orifices. McNeil (2000), who also referred to the work of Fairhurst (1983) on globe valves, has published work on the approximation of flow in orifice plates, gate valves as well as globe valves.

The flow through ports undergoes an energy conversion process, which can be described as an equation to calculate the velocity at the downstream side of the ports:

$$U = \sqrt{2(h_u - h_d)} = \sqrt{2\Delta h} \quad [4\text{-}9]$$

where h_u and h_d are the up-stream and down-stream isentropic enthalpy, respectively

Δh is an isentropic enthalpy drop along the flow direction

When the losses due to friction and the change in cross-sectional area are taken into account, equation [4-9] can be re-written as a function of the enthalpy drop and the loss coefficient, $K_p = N_p f$, as follows (Massoud, 2005):

$$U = \sqrt{\frac{2\Delta h}{K_p}} \quad [4\text{-}10]$$

where N_p is a specific number given for a specific type of flow and f is a friction factor for turbulent flow. The friction factor, f, can be calculated using the Colebrook correlation (Munson, Rothmayer, Okiishi, & Huebsch, 2013) as follows:

$$\frac{1}{\sqrt{f}} = -2.0\, log\left(\frac{\varepsilon/D}{3.7} + \frac{2.51}{Re\sqrt{f}}\right) \quad [4\text{-}11]$$

where ε is the surface roughness, D is the diameter or hydraulic diameter of the pipe or the flow container, and Re is the Reynolds number. Equation [4-11], however, requires

iteration to solve for the friction factor, f. Hence, Massoud (2005) suggested that in most engineering applications where smooth pipes are utilised and the flow is fully developed turbulent, the friction factor can be expressed using the McAdams formulation:

$$f = \frac{0.184}{Re^{0.2}} = \frac{0.184}{\left(\frac{\rho UD}{\mu}\right)^{0.2}}$$

[4-12]

From the definition of Reynolds number, $Re = \frac{\rho UD}{\mu}$, equations [4-10] and [4-12] can be utilised to find the velocity of flow through the inlet port of the limaçon-to-circular machine as:

$$U_i = \begin{cases} \left(\frac{2\Delta h}{0.184 N_p}\right)^{\frac{5}{9}} \left(\frac{\rho_{id} D_{id}}{\mu_{id}}\right)^{\frac{1}{9}} & if \ \sqrt{2\Delta h} < U_s \\ \frac{U_s^{\frac{11}{10}}}{\sqrt{0.184 N_p}} \left(\frac{\rho_{id} D_{id}}{\mu_{id}}\right)^{\frac{1}{10}} & if \ \sqrt{2\Delta h} > U_s \end{cases}$$

[4-13]

where subscript i represents the flow through the inlet port.

$\rho_{id}, D_{id}, and\ \mu_{id}$ are the down-stream density, hydraulic diameter, and viscosity, respectively.

U_s is the speed of sound on the down-stream side of the port

The above equation can also be used to calculate the velocity of flow through the outlet port by replacing the subscript i for the inlet, by o for the outlet. Equation [4-13] can be utilised for both single and two-phase flow situations. In two-phase flow condition, the homogeneous flow model (Fairhurst, 1983) is to be employed and used in line with equations [4-12] and [4-13], in which the equivalent viscosity is obtained using the McAdams' equation as follows:

$$\frac{1}{\mu_{id}} = \frac{x}{\mu_{vap}} + \frac{1-x}{\mu_{lid}} \quad [4\text{-}14]$$

where μ_{id} is the equivalent down-stream viscosity of the inlet port

μ_{vap}, and μ_{lid} are the viscosities of the vapour and liquid phase, respectively

$x = \frac{mass\ flowrate\ of\ the\ gas\ phase}{total\ mass\ flowrate} = \frac{\dot{m}_{gas}}{\dot{m}_{liquid}+\dot{m}_{gas}}$ is the dryness fraction (Ryley, 1964)

Additionally, the speed of sound of the two-phase flow can be calculated either by using the available REFPROP functions offered by Lemmon et al. (2010) or based on the equilibrium of mechanical, thermal, and fluid phase assumptions, such an approach is detailed in the published work by Lund and Flatten (2010). The accuracy of the speed of sound can also be improved by using the two methods simultaneously.

With the utilisation of the loss coefficient, K_p, and the McAdams formulation, the velocity of fluid flows through the inlet and outlet ports can be calculated using equation [4-13] in a non-iterative manner. Moreover, the employment of the enthalpy difference instead of pressure difference has excluded the need of calculating the expansion factor during the expansion process in two-phase flow condition. Hence, in the following section, the flow velocity equation [4-13] will be put in to use in accordance with the continuity and energy equations in order to obtain a thermodynamic model for the limaçon-to-circular machine.

4.6. The seal dynamics model

It is important to take into account the effect of apex sealing in the thermodynamic performance model of this limaçon-to-circular machine. The apex seal model presented in Chapter 3 has been used to calculate possible leakages between the upper and lower

chambers through the seal-housing gap. The apex seal model, presented in Chapter 3, has also been utilised to calculate friction between the seal and the machine housing.

4.7. Dynamic response of inlet valve

To control the amount of fluid entering the machine chamber to be expanded, a control valve is fitted at the inlet, as shown in Figure 4-3. The inclusion of an inlet valve has subsequently created an antechamber, V_3, which separates the inlet passage and the machine working chambers. Hence, during the machine operation, fluid will need to fill this antechamber before entering the upper chamber instead of flowing directly from the inlet to the upper chamber as in the case of no-inlet-valve design. Figure 4-3 shows that depending on the angular position of the rotor, the antechamber can be exposed to either the upper chamber, the lower chamber, or both at the same time. The inlet valve is of a normally open type and kept open by a spring, k_v, as shown in Figure 4-3. The spring force, $k_v\delta_v$, is large enough to keep the valve open even when the top surface of the valve is exposed to pressure from the supply tank. The valve stem is connected to a lever which is then connected to a plunger the motion of which controls the valve opening and closing. Movement of the plunger is controlled by two solenoids installed at the two ends of the stem (Figure 4-3). One solenoid helps closing the valve to cut off fluid supply, the other assists the spring during the valve opening phase. This design aims to reduce the valve response time and ensures that the machine can still functioning in case one or both of the solenoids fail. Of note is the position of the pivot point, this point is located closer to the valve stem than to the plunger; the distances from pivot point to the valve stem and plunger are a and b, respectively. The ratio of the arms will help increasing the amount of force acting on the valve steam at the same time reducing the current load on the solenoid coils.

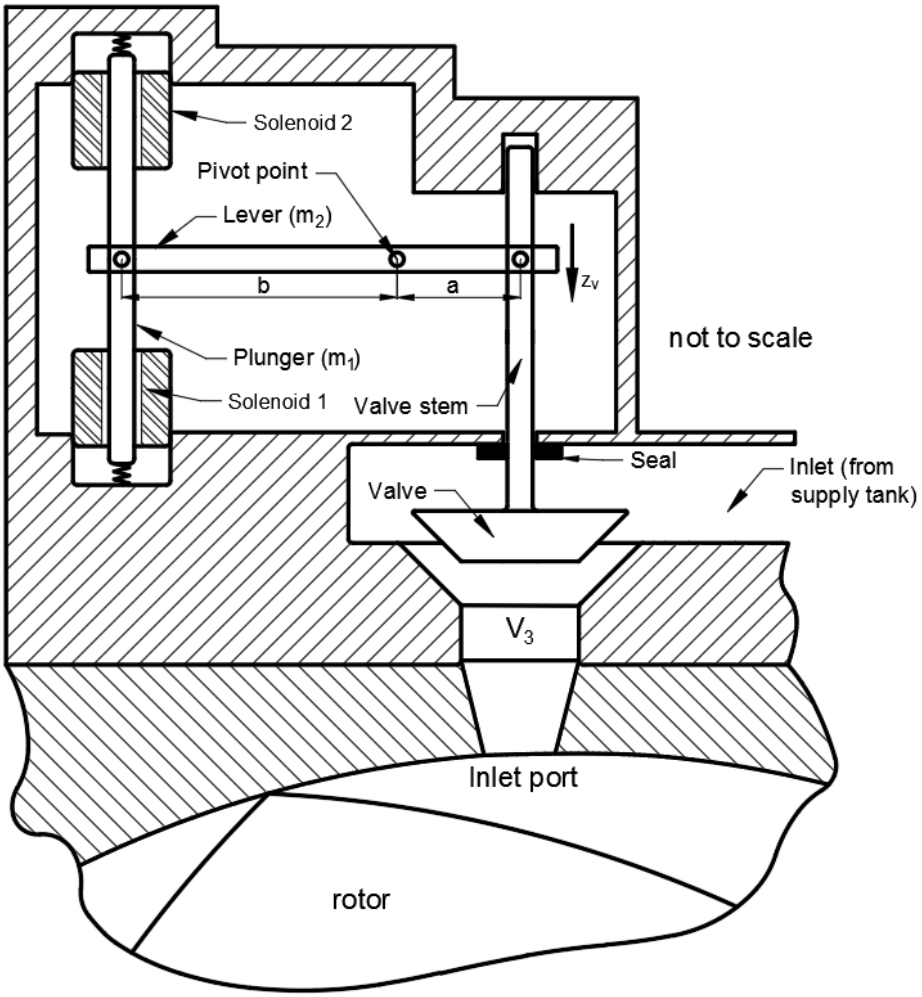

Figure 4-3: Design of an inlet valve

It is now essential to derive the equation of motion of this plunger-lever-valve system. The mass of the plunger, the lever, and the valve are defined as m_1, m_2, and m_3 respectivety. The distances the valve and the plunger travel in vertical direction are z_v and x_v, respectively; linear motion of the centre of gravity (CG) of the lever in the vertical direction is y_v. The potential energy and kinetic energies of the system can be expressed as:

$$PE = \frac{1}{2}k_v(\delta_v + x_v)^2 + m_1 g x_v + m_2 g y_v - m_3 g z_v \quad [4\text{-}15]$$

and

$$KE = \frac{1}{2}m_1\dot{x}_v^2 + \frac{1}{2}m_2\dot{y}_v^2 + \frac{1}{2}m_3\dot{z}_v^2 + \frac{1}{2}I_2\dot{\theta}_v^2$$

[4-16]

Equation [4-15] and [4-16] can be rewritten in terms of z_v and $\dot{z}_v$ as follows:

$$PE = \frac{1}{2}k_v\left(\delta_v + z_v\frac{b}{a}\right)^2 + \left[m_1\frac{b}{a} + m_2\left(\frac{b-a}{2a}\right) - m_3\right]gz_v$$

[4-17]

and

$$KE = \frac{1}{2}m_1\left(\frac{b}{a}\right)^2\dot{z}_v^2 + \frac{1}{2}m_2\left(\frac{a+b}{2a}\right)^2\dot{z}_v^2 + \frac{1}{2}m_3\dot{z}^2 + \frac{1}{2}\frac{I_2}{a^2}\dot{z}_v^2$$

$$KE = \frac{1}{2}\left[m_1\left(\frac{b}{a}\right)^2 + m_2\left(\frac{a+b}{2a}\right)^2 + m_3 + \frac{I_2}{a^2}\right]\dot{z}_v^2$$

[4-18]

where k_v is the spring stiffness; δ_v is the spring initial deflection. The spring is aligned with the solenoids plungers

I_2 is the moment of inertia of the lever about the pivot point

$\dot{x}_v, \dot{y}_v$, and $\dot{z}_v$ are the velocity of m_1, m_2, and m_3, respectively.

Differentiating the equation of potential energy with respect to z_v and kinetic energy with respect to $\dot{z}_v$ give:

$$\frac{\partial PE}{\partial z_v} = k_v\frac{b}{a}\left(\delta_v + z_v\frac{b}{a}\right) + \left[m_1\frac{b}{a} + m_2\left(\frac{b-a}{2a}\right) - m_3\right]g$$

[4-19]

and

$$\frac{\partial KE}{\partial \dot{z}_v} = \left[m_1\left(\frac{b}{a}\right)^2 + m_2\left(\frac{a+b}{2a}\right)^2 + m_3 + \frac{I_2}{a^2}\right]\dot{z}_v$$

[4-20]

Based on the Lagrange energy method, the equation of motion of this system can be written as

$$\left[m_1\left(\frac{b}{a}\right)^2 + m_2\left(\frac{a+b}{2a}\right)^2 + m_3 + \frac{I_2}{a^2}\right]\ddot{z}_v + c_{eq}\dot{z}_v + kz_v\left(\frac{b}{a}\right)^2 = -k_v\delta_v\left(\frac{b}{a}\right) - \left[m_1\frac{b}{a} + m_2\left(\frac{b-a}{2a}\right) - m_3\right]g + \Delta P C_d A_v + F_{sl}\frac{b}{a} + F_{sur} \quad [4\text{-}21]$$

where c_{eq} is the equivalent damping coefficient;

$\Delta P = P_{in} - P_3$ is the difference in pressure between the inlet and antechamber;

C_d is the drag coefficient of the valve, $0.6 \leq C_d \leq 0.9$

A_v is the area of the vale that is subjected to the effect of pressure difference;

F_{sl} is the force exerted by the solenoids; and

F_{sur} is the contact force that the valve experiences either from the seat or from the mechanical stopper.

The force F_{surf} can be calculated by using the following algorithm:

if $z_v > s_{st}$
  $F_{sur} = -k_{seat}(z_v - s_{st}) - c_{seat}\dot{z}_v$
else if $z_v < 0$
  $F_{sur} = -k_{stop}z_v - c_{stop}\dot{z}_v$
else
  $F_{sur} = 0$
end

where s_{st} is the stroke or the maximum motion of the valve stem

k_{seat} and k_{stop} are the stiffness of the seat and mechanical stopper, respectively

c_{seat} and c_{stop} are the damping coefficient of the seat and mechanical stopper, respectively

Yuan and Li (2004), in their paper, present a mathematical model from which force exerted by a solenoid can be calculated. Based on such a model, the solenoid force, F_{sl}, for this inlet valve model can be calculated as follows:

$$F_{sl} = \frac{\beta_{s_1}}{2}\left(\frac{i_{s_1}}{z_{s_1} + d_{0_s}}\right)^2 - \frac{\beta_{s_2}}{2}\left(\frac{i_{s_2}}{z_{s_2} + d_{0_s}}\right)^2 \quad [4\text{-}22]$$

where subscript $i = 1$ or 2 are for two-solenoid set up; i_{s_i} are solenoid currents;

z_{s_i} are the displacements of the plunger relative to the solenoids 1 and 2;

$\beta_{s_1} = \beta_{s_2} = \beta_s$ and d_{0_s} are given by Yuan and Li (2004);

The displacement of the plunger can be calculated from the relationship with the valve stem displacement as $z_{s_1} = \frac{b}{a} z_v$ and $z_{s_2} = \frac{b}{a}(s_{st} - z_v)$. The velocities $\dot{z}_{s_1}$ and $\dot{z}_{s_2}$ depends on the velocity of the valve as follows

$$\dot{z}_{s_1} = \frac{b}{a}\dot{z}_v \quad and \quad \dot{z}_{s_2} = -\frac{b}{a}\dot{z}_v \quad [4\text{-}23]$$

The solenoids are controlled based on the angular position of the rotor. When the inlet valve is required to be opened or closed at a certain rotor angular position, θ, a electrical voltage is applied to the opening or closing solenoids. Before the solenoids can effectively close or open the inlet valve, current flow within the coils need time to build up. This current build-up can be derived from the relationship between voltage and current as follows:

$$V_{s_1} = i_{s_1} R_{s_1} - \frac{i_{s_1} \beta_s}{\left(z_{s_1} + d_{0_s}\right)^2} \dot{z}_{s_1} + \frac{\beta_s}{z_{s_1} + d_{0_s}} \frac{di_{s_1}}{dt}$$

[4-24]

which can be rearranged for the change of current with respect to time as:

$$\frac{d_{i_{s_1}}}{dt} = \frac{z_{s_1} + d_{0_s}}{\beta_s} \left[V_{s_1} - i_{s_1} R_s + \frac{\beta_s i_{s_1} \dot{z}_{s_1}}{\left(z_{s_1} + d_{0_s}\right)^2} \right]$$

[4-25]

Similarly, the build-up of current in the second solenoid can be expressed as:

$$\frac{d_{i_{s_2}}}{dt} = \frac{z_{s_2} + d_{0_s}}{\beta_s} \left[V_{s_2} - i_{s_2} R_s + \frac{\beta_s i_{s_2} \dot{z}_{s_2}}{\left(z_{s_2} + d_{0_s}\right)^2} \right]$$

[4-26]

The nonlinear differential equations given by [4-21], [4-25], and [4-26] can be solved simultaneously in an iterative fashion to calculate the valve position and the solenoid currents at every rotor angle, θ. The voltages that drive the solenoids are given as shown in Figure 4-4 below to open and close the inlet valve at angles which are meant to match the power requirements of the expander for a given demand.

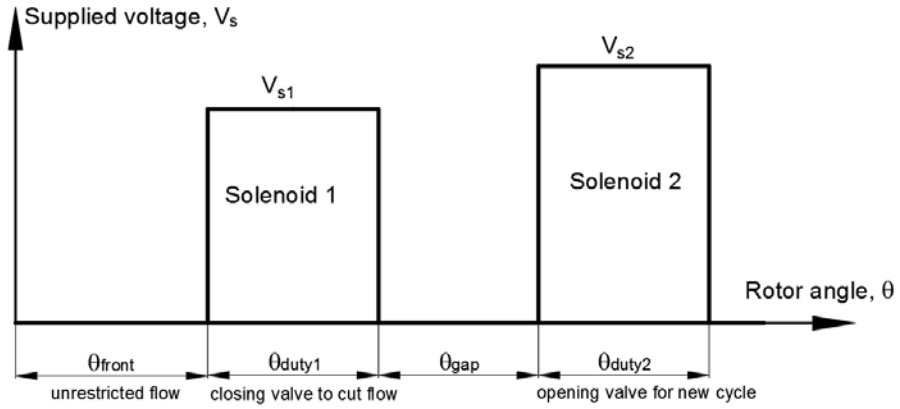

Figure 4-4: Solenoid control voltage

The effective orifice area or the equivalent area of the valve that allows the fluid to flow through during the valve opening phase can be calculated based on a simplified version of Hunt and Davis's equation as follows (Tuymer & Machu, 2001):

$$A_{eq} = \sqrt{\frac{1}{\frac{1}{(0.85\,\pi D_s(s_{st}-z_v))^2} + \frac{1}{A_v^2}}}$$

[4-27]

Where $A_v = \frac{\pi}{4} D_s^2$ and D_s is the diameter of the valve seat.

The thermodynamic model of limaçon machine is detailed in the next section.

4.8. The thermodynamic model

The performance of a limaçon-to-circular machine depends on the derivative $\frac{dV_{net\_b}}{d\theta}$, which can be expressed as:

$$\frac{dV_{net_b}}{d\theta} = 4bHL^2 \sin\theta$$

[4-28]

where V_{net_b} is volume of the working chamber below the rotor chord previously described in equation [4-2]. Hence, the mass flow rate, $\dot{m} = \frac{dm}{dt}$, of the fluid inside the working chamber in relation with the fluid density, the available chamber volume, and the rotor angular position can be obtained as:

$$\frac{dm}{dt} = \left(4b\rho HL^2 \sin\theta + V_{net_b}\frac{d\rho}{d\theta}\right)\frac{d\theta}{dt} = \left(4b\rho HL^2 \sin\theta + V_{net_b}\frac{d\rho}{d\theta}\right)\omega$$

[4-29]

where ρ, and m are in turn the instantaneous density and mass of the fluid inside the working chamber at any given rotor angle θ. The term $\frac{d\theta}{dt} = \omega$ is the rotor angular

velocity given in $\frac{rad}{s}$. The change of the fluid mass in the working chamber below the rotor chord can be obtained by rearranging equation [4-29] as follows:

$$\frac{d\rho_b}{d\theta} = \frac{1}{V_{net\_b}}\left(\frac{1}{\omega}\frac{dm}{dt} - 4b\rho_b HL^2 \sin\theta\right) \quad [4\text{-}30]$$

where the subscript b denotes "below the rotor".

When the continuity equation is utilised and the effect of leakage through the sides of the machine and the apex seals are taken into account, equation [4-30] can then be re-written for the change of fluid mass in the two chambers below and above the rotor chord, respectively, as:

$$\frac{d\rho_b}{d\theta} = \frac{1}{V_{net\_b}}\left(\frac{1}{\omega}(A_{ib}\rho_{idb}U_{ib} - A_{ob}\rho_{odb}U_{ob} - \dot{m}_{sb} \pm \dot{m}_{asb}) - 4b\rho_b HL^2 \sin\theta\right) \quad [4\text{-}31]$$

$$\frac{d\rho_a}{d\theta} = \frac{1}{V_{net\_a}}\left(\frac{1}{\omega}(A_{ia}\rho_{ida}U_{ia} - A_{oa}\rho_{oda}U_{oa} - \dot{m}_{sa} \mp \dot{m}_{asa}) - 4b\rho_a HL^2 \sin\theta\right) \quad [4\text{-}32]$$

where subscripts i, o, d, a, and b denote "inlet", "outlet", "down-stream", "above the rotor chord", and "below the rotor chord", respectively

$\dot{m}_s$ and $\dot{m}_{as}$ are the mass flowrate of leakages of working fluid through the sides of the machine and apex seals, respectively

The velocity of the fluid through the inlet and outlet ports, U_i and U_o, can be calculated by utilising equation [4-13]. The signs $\pm$ show the directions of such leakages, which are governed by the instantaneous value of pressures in the upper and lower chambers.

When the energy transfers to and from the fluid inside the working chamber is considered to occur as an adiabatic process, the following equation can be utilised:

$$\frac{dh_i}{dt} - \frac{dh_o}{dt} = \frac{d(me)}{dt} + \frac{PdV}{dt} \quad [4\text{-}33]$$

where h_i, and h_o are the total enthalpy moving in and out of a working chamber, respectively; e is the specific internal energy available in the working chamber. Since, the term internal energy, e, can be substituted by $h - pv$, and $m\frac{dh}{dt} = mT\frac{ds}{dt} + V\frac{dP}{dt}$, equation [4-33] can be re-written as:

$$\frac{dh_i}{dt} - \frac{dh_o}{dt} = \frac{mTds}{dt} + \frac{hdm}{dt} \quad [4\text{-}34]$$

or
$$mT\omega\frac{ds}{d\theta} = (h_i - h)\frac{dm_i}{dt} - (h_o - h)\frac{dm_o}{dt} \quad [4\text{-}35]$$

The above equation can then be manipulated to produce equations, which show the rate of entropy change in the two working chambers per rotor angular rotational angle as below:

$$\frac{ds_b}{d\theta} = \frac{1}{\omega\rho_b V_b T_b}[A_{ib}U_{ib}\rho_{idb}(h_{iub} - h_b) - A_{ob}U_{ob}\rho_{odb}(h_{oub} - h_b) - \dot{m}_{sb}(h_{sb} - h_b) \pm \dot{m}_{asb}(h_{asb} - h_b)] \quad [4\text{-}36]$$

$$\frac{ds_a}{d\theta} = \frac{1}{\omega\rho_a V_a T_a}[A_{ia}U_{ia}\rho_{ida}(h_{iua} - h_a) - A_{oa}U_{oa}\rho_{oda}(h_{oua} - h_a) - \dot{m}_{sa}(h_{sa} - h_b) \mp \dot{m}_{asa}(h_{asa} - h_a)] \quad [4\text{-}37]$$

where the subscripts i, o, d, u, a, and b denote "inlet", "outlet", "down-stream", "up-stream", "above the rotor chord", and "below the rotor chord", respectively

m_s and m_{as} are the mass flowrate of leakages of working fluid through the sides of the machine and apex seals

h_s and h_{as} are the enthalpy on the upstream side of the sides and apex seals

Equations [4-31], [4-32], [4-36], and [4-37] can be solved simultaneously to the find the instantaneous values of densities, and entropies below and above the rotor chord, ρ_b, ρ_a, s_b, and s_a, of fluid in the two working chambers at each crank angle, θ. At each calculation step, the corresponding values of pressure, P, density, ρ, and viscosity, μ, can be calculated using the above equations. The instantaneous values for temperature, T, and enthalpy, h, can be calculated with the assistance of the functions $T(P, s)$, and $h(P, s)$ offered in REFPROP, which can be linked to Matlab for fluid properties calculation (Lemmon, Huber, & McLinden, 2010; National Institute of Standards and Technology, 2016). The REFPROP functions deliver the fluid properties for not only single but also two-phase flows that are accurate enough for the calculations in this paper. In order to achieve further accuracy for the speed of sound in two-phase flow, the REFPROP functions has been utilised in conjunction with the algorithm offered in the published work by Lund and Flatten (2010).

In this paper, the authors investigate one of the embodiments of the limaçon machines; hence, the instantaneous crankshaft torque value can be calculated based on the equation suggested by Sultan (2005), as shown below:

$$\tau = 4bL^2H(P_{cb} - P_{ca}) \sin\theta \qquad [4\text{-}38]$$

where the subscript c, b, and a are "chamber", "below the rotor", and "above the rotor" respectively.

The calculation process for the machine crankshaft torque has been approached iteratively by applying the thermodynamic model and compute at small crank angle increments within the range $\theta_{li} \leq \theta \leq \theta_{li} + \pi$ in which the θ_{li} is angular position of the inlet port leading edge. The values of pressure and density below the rotor at the start of the cycle, $P_{cb}(\theta_{li})$ and $\rho_{cb}(\theta_{li})$, respectively, are compared with the corresponding values of pressure and density above the rotor chord at the end of the cycle, $P_{ca}(\theta_{li} + \pi)$ and $\rho_{ca}(\theta_{li} + \pi)$. At the same time, the values of pressure and density above the rotor at the start of the cycle, $P_{ca}(\theta_{li})$ and $\rho_{ca}(\theta_{li})$, respectively, are compared with the corresponding values of pressure and density below the rotor at the end of the cycle, $P_{cb}(\theta_{li} + \pi)$ and $\rho_{cb}(\theta_{li} + \pi)$. The comparison process is done by using the dimensionless error expression shown below:

$$\epsilon = \left[\left(\frac{P_{cb}(\theta_{li}) - P_{ca}(\theta_{li} + \pi)}{\overline{P_l}}\right)^2 + \left(\frac{\rho_{cb}(\theta_{li}) - \rho_{ca}(\theta_{li} + \pi)}{\overline{\rho_l}}\right)^2 + \left(\frac{P_{ca}(\theta_{li}) - P_{cb}(\theta_{li} + \pi)}{\overline{P_u}}\right)^2 + \left(\frac{\rho_{ca}(\theta_{li}) - \rho_{cb}(\theta_{li} + \pi)}{\overline{\rho_u}}\right)^2\right]^{1/2} \quad [4\text{-}39]$$

where $\overline{P_l} = \frac{P_{cb}(\theta_{li}) + P_{ca}(\theta_{li} + \pi)}{2}$, $\overline{\rho_l} = \frac{\rho_{cb}(\theta_{li}) + \rho_{ca}(\theta_{li} + \pi)}{2}$, $\overline{P_u} = \frac{P_{ca}(\theta_{li}) + P_{cb}(\theta_{li} + \pi)}{2}$, and $\overline{\rho_u} = \frac{\rho_{ca}(\theta_{li}) + \rho_{cb}(\theta_{li} + \pi)}{2}$ are the pressure and density coefficients used to calculate the error.

If the value of error expression, ϵ, is larger than a small value defined by the designer, the values of $P_{cb}(\theta_{li}), \rho_{cb}(\theta_{li}), P_{ca}(\theta_{li}), and\ \rho_{ca}(\theta_{li})$ are set to be equal to $P_{ca}(\theta_{li} + \pi), \rho_{ca}(\theta_{li} + \pi), P_{cb}(\theta_{li} + \pi), and\ \rho_{cb}(\theta_{li} + \pi)$, respectively. The calculation process is then repeated over the range of $\theta \in [\theta_{li}, \theta_{li} + \pi]$ until the outcome of the error expression

falls below the predefined value, which reflects the cyclical nature of the thermodynamic process. Once the convergence is achieved, the total energy per one cycle, E_{cycle}, can be calculated by utilising the following equation:

$$E_{cycle} = 2\,\delta\theta\left(\sum_{n=1}^{N}\tau_{sn} - \frac{\tau_{sn}+\tau_{s1}}{2}\right) \quad [4\text{-}40]$$

where $\delta\theta$ is the size of the angular interval, $n \in [1, N]$ is the counter for the successive points on the torque curve, and N is the total number of intervals on the torque curve.

With the same approach, the total mass flow through the machine in one cycle, M_{cycle}, can be calculated using the expression below:

$$M_{cycle} = 2\frac{\delta\theta}{\omega}\left\{\sum_{n=1}^{N}[(A_{ib}\rho_{idb}U_{ib})_n + (A_{ia}\rho_{ida}U_{ia})_n] - \frac{(A_{ib}\rho_{idb}U_{ib})_n + (A_{ib}\rho_{idb}U_{ib})_1}{2} - \frac{(A_{ia}\rho_{ida}U_{ia})_n + (A_{ia}\rho_{ida}U_{ia})_1}{2}\right\} \quad [4\text{-}41]$$

The machine overall efficiency can be calculated from the total energy per one cycle and total mass flow through the machine as follows:

$$\eta_o = \frac{E_{cycle}}{M_{cycle}\Delta h_{is}} \quad [4\text{-}42]$$

Where Δh_{is} is the difference between the enthalpy in the inlet manifold and its isentropically reduced value in the discharge manifold. It should be highlighted that in order to account for the fact that for each full rotation of the shaft, the limaçon-to-circular

machine has two fluid expanding cycles, hence, a multiplication by two is incorporated in equations [4-40] and [4-41].

4.9. Numerical illustrations

The study of this limaçon-to-circular expander utilises organic gas R-245fa as a working fluid. Saturated R-245fa is made available at an absolute pressure of 10 bars and temperature of 145℃. The working fluid will be expanded from 10 bars to the pressure of 1 bar at the outlet manifold. The expander is allowed to run at various angular velocity i.e.: 800, 1200, 1500, and 1800 RPM and various values of antechamber, V_3. Some of the machine dimensions such as rotor half-chord length, L, limaçon aspect ratio, b, limaçon-to-circular design fator, a, radial clearance, Δ_{min}, rotor depth multiplication factor, β, and clearance volume factor, μ, will be used as constant in this study. These dimensions, which have been previously optimised for limaçon-to-circular machine (Phung, Sultan, & Boretti, 2016), are shown in Table 4-1 below. The limaçon rotor axial depth is given as $H = \beta L$.

Table 4-1: Dimensions of the limaçon-to-circular machine

	Values	Units
Rotor half-chord length, L	64.29	*mm*
Limaçon aspect ratio, b	0.165	-
The design factor, a	1.096	-
Radial clearance, Δ_{min}	0.1	*mm*
Rotor depth multiplication factor, β	1.3	-
Clearance volume factor, μ	0.167	-

In the following table, the values for inlet and outlet port angular positions, angular widths, and lengths are set as:

Table 4-2: Limaçon machine's port geometries

	Values
Inlet port angular position, θ_{li}	-25^o
Outlet port angular position, θ_{lo}	140^o
Inlet port angular width, $\Delta\theta_i$	31.78^o
Outlet port angular width, $\Delta\theta_o$	32.9^o
Inlet port length, L_o	$71\ mm$
Outlet port length, L_i	$107\ mm$

A representation of chamber pressure and temperature against the crank angle, θ, and the pressure-volume relationship can be found in Figure 4-5 and Figure 4-6 as below:

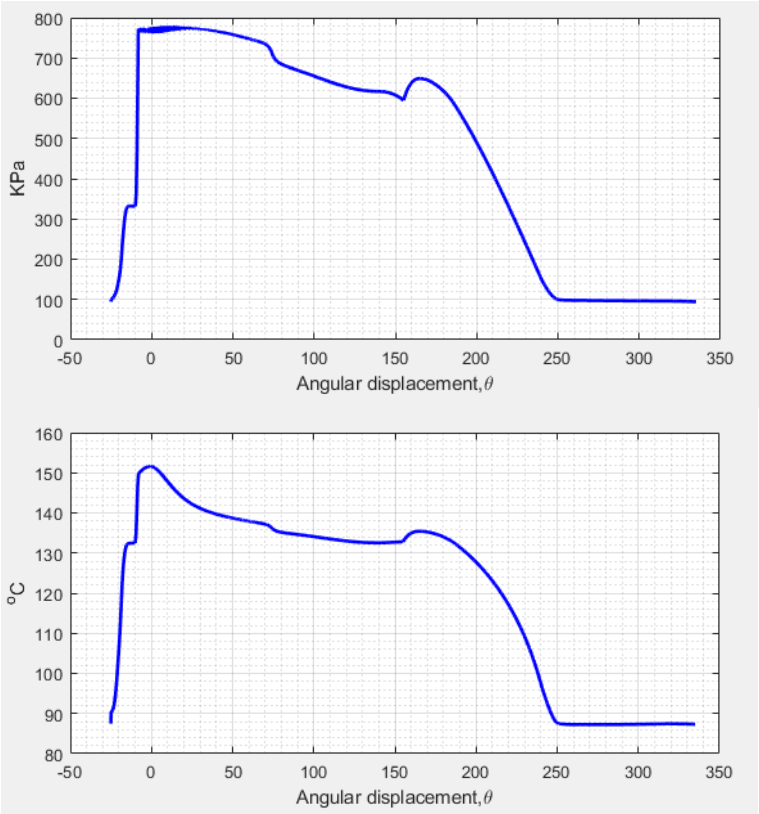

Figure 4-5: Chamber pressure and temperature against crank angle

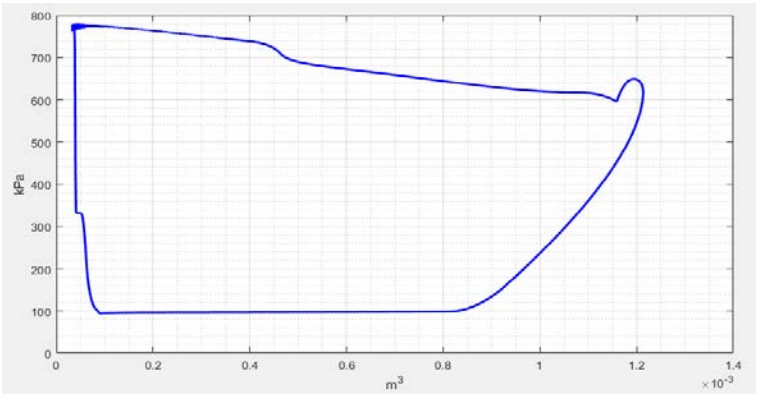

Figure 4-6: Limaçon machine PV diagram

Volume of the antechamber, V_3, also affect the pressure within the machine working chamber as shown in Figure 4-7. When volume of antechamber is small, pressure inside the machine working chamber tends to drop further compared to the case where antechamber volume is large. This is also true with the temperature drop in the working chamber (Figure 4-7). The larger the antechamber gets, fluid supply to the limaçon machine is more sufficient which can help the machine utilising the pressure difference between the inlet and outlet more effectively. Moreover, increasing the antechamber volume, of course to a certain extent, also means that the inlet valve doesn't need to stay open for a long period of time to supply working fluid; this effect will be shown later in this section.

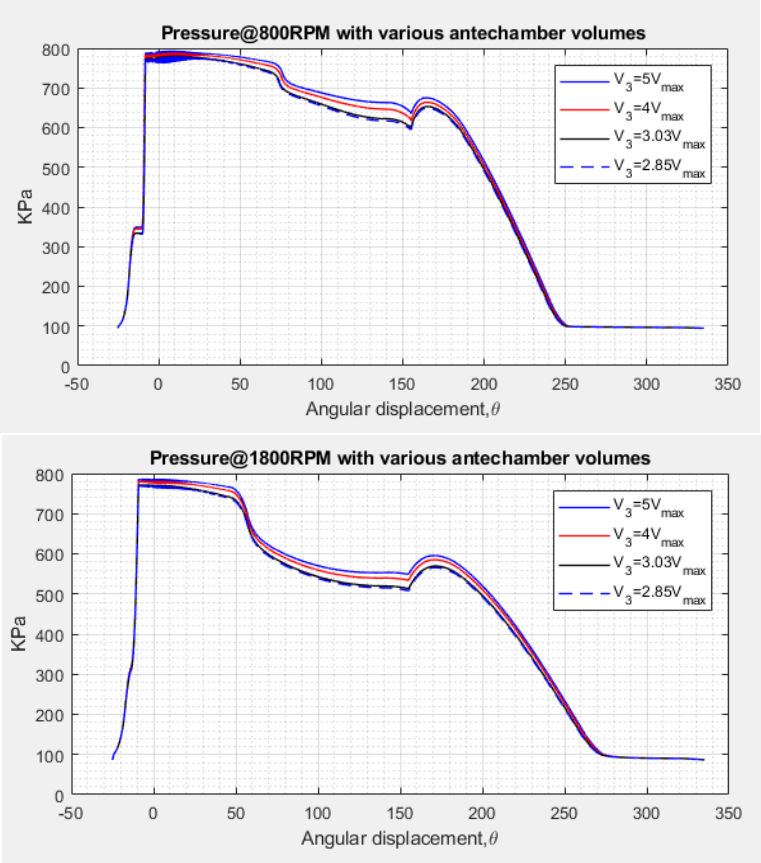

Figure 4-7: The effect of antechamber volume to the working chamber pressure at various RPM

The magnitude of solenoid voltages V_{s_1} and V_{s_2} can be set by the designer based on the operational condition of limaçon machine; here, these voltages were set equal as $V_{s_1} = V_{s_2} = V_s = 75\,Volt$. The valve opening and closing with respect to rotor angular displacement at different RPMs and antechamber volumes are shown in Figure 4-8; of note is that the valve stroke is set at $5\,mm$ (Figure 4-8).

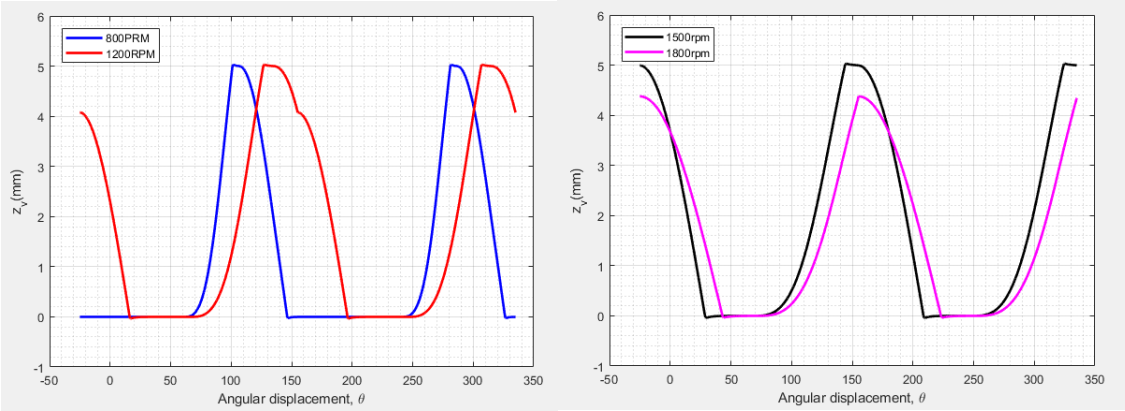

Figure 4-8: Valve opening against rotor angle at various RPM and V_3

In this design, the valve is fully open when valve motion, $z_v = 0$; when $z_v = 5\,mm$, the valve is fully closed. Figure 4-8 shows the valve action with the help from solenoids at various angular velocities. It is worth noting that when voltage is supplied to the coils, the solenoid currents need to build-up before the solenoids can jump into action to close the valve and cut off fluid supply or assist the valve spring in the vale opening phase. Such current build-ups are shown in Figure 4-9. Obviously, the valve displacement, z_v, increases or decreases gradually according to solenoid responses. Figure 4-8 also shows that the valve can stay open for a much longer period at lower RPM – shown as solid blue curve – compared to higher RPM – shown as red or solid black curve. This results in better fluid supply for the antechamber and consequently the machine working chamber. The solid magenta curve shown in Figure 4-8, in particular, is an indication that the inlet valve cannot achieve fully close position. This is due to the relatively slow response time of the solenoids compared to the machine angular velocity. This problem can be easily overcome when faster response time solenoids are used in limaçon machines that operate at higher RPM.

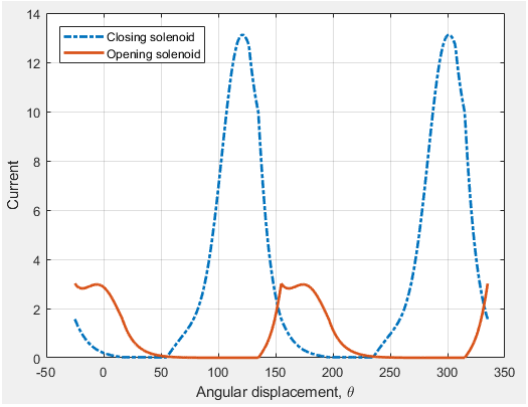

Figure 4-9: Solenoid currents at one particular RPM

Figure 4-10 and Figure 4-11 show linear and angular magnitudes of the seal motion as well as the seal-housing forces at 800 and 1800 RPM, respectively. The forces exerted between the seal and housing when the machine runs at 1800 RPM is significantly higher than that of the 800 RPM. In fact, this behaviour is expected since at lower RPM the difference in pressure between the machine chamber and the outlet is much greater as shown in Figure 4-7. This pressure difference tends to push the seal against one side of the seal groove and help reducing both linear and angular displacement of the seal. At higher RPM, the centrifugal force on the seal together with the lower in pressure difference have seen seal motion inside the seal groove and seal-housing force increasing. Such an increase in seal-housing force will result in higher friction force between the seal tip and the machine housing surface which will adversely affect the machine performance. Hence it is critical to find an optimum seal spring stiffness, inlet valve settings, volume of antechamber, and RPM to maximise the machine output power.

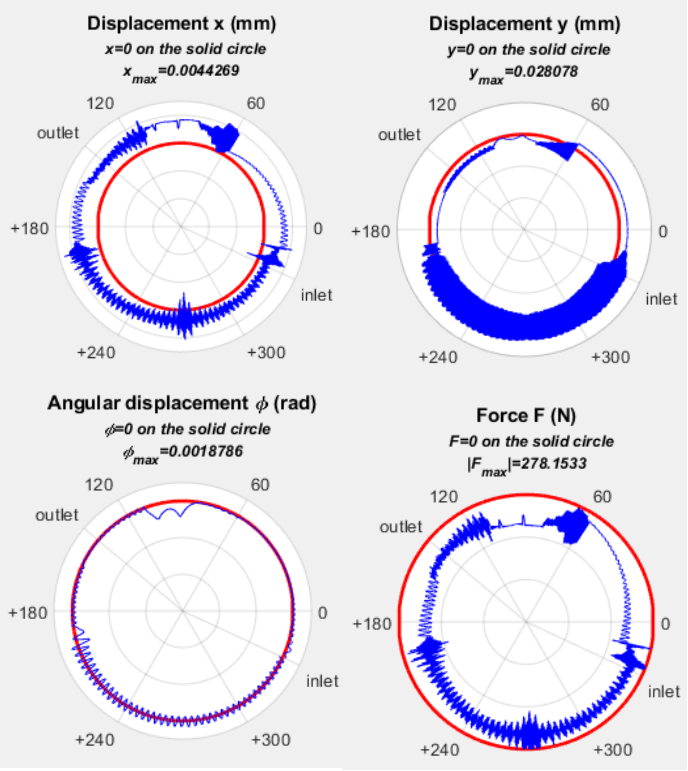

Figure 4-10: Seal displacements and seal-housing force @800 RPM and $V_3 = 2.85\ V_{max}$

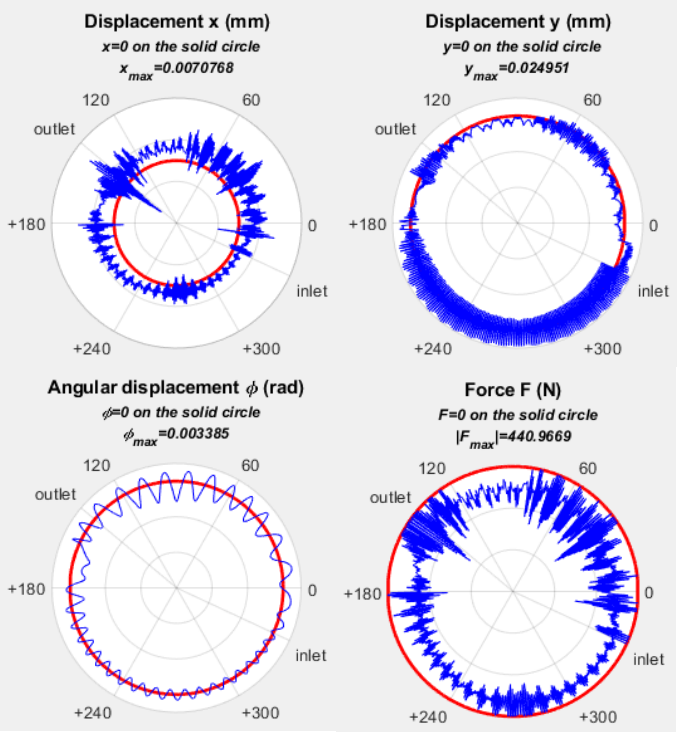

Figure 4-11: Seal displacements and seal-housing force @1800 RPM and $V_3 = 2.85\ V_{max}$

The overall efficiencies of the limaçon machine at different RPM and values of antechamber V_3, as shown in Figure 4-12, can be calculated using equations [4-40], [4-41], and [4-42]. It is worth noting that although the amount of friction loss between seal and housing increases with the increase of RPM, the overall efficiency of the machine improves significantly at higher speed.

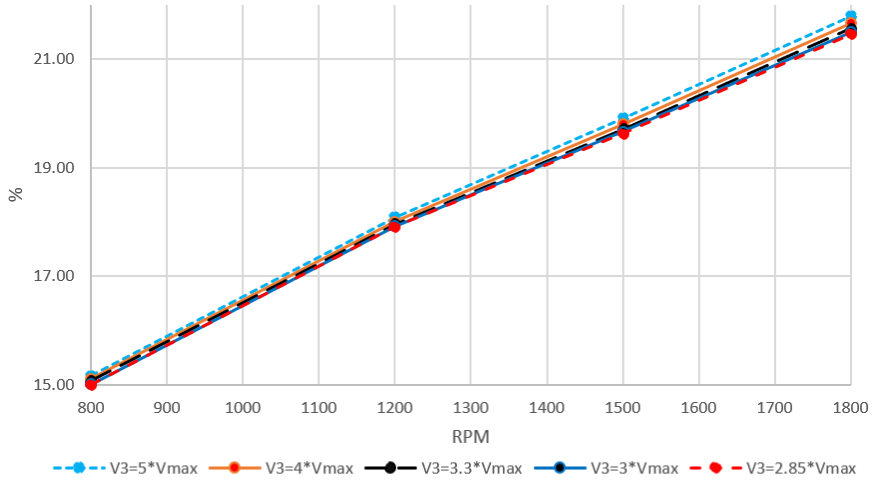

Figure 4-12: Limaçon machine overall efficiencies at different RPM

4.10. Conclusion

This paper investigates the thermodynamic performance of the limaçon-to-circular machines; the inlet and outlet ports' angular positions, angular widths, and lengths of the limaçon-to-circular machines have been previously optimised based on the operational condition. The seal dynamic models as well as the inlet valve dynamics response have been taken into account to demonstrate and compare the effectiveness and efficiency of the machine due to sealing and inlet valve inclusion.

Nomenclatures

$2L$: the limaçon chord length

XY : stationary frame

X_rY_r : moving frame

o : limaçon pole

p_l, p_t : leading and trailing apices

θ : crank angle

r : radius of the base circle

m : centre point of the chord

R : radius of the circular segment

C : clearance value

b : limaçon aspect ratio

V_{net} : volume of the working chamber

H : the expander's housing depth

$\boldsymbol{R}_l, \boldsymbol{R}_t$: position vector of the ports' leading and trailing edges

$\widehat{\boldsymbol{R}}_l, \widehat{\boldsymbol{R}}_t$: leading and trailing unit vectors

θ_l, θ_t : angular positions of the leading and trailing edges

L_p : port length

W : port width

A_f : cross sectional area of the port

A_p : instantaneous value of the port area

$\boldsymbol{P}_l, \boldsymbol{P}_t$: position of the rotor's leading and trailing edges

$\widehat{\boldsymbol{X}}_r$: unit vector along the rotor chord

$\widehat{\boldsymbol{Y}}_r$: unit vector along the axis perpendicular to the rotor chord

s_l, s_t : relative locations of the rotor leading and trailing apices with respect to the port leading and trailing edges

U : velocity of the fluid

h_u, h_d : upstream and downstream isentropic enthalpy

Δh : isentropic enthalpy drop along the flow direction

K_p : the loss coefficient

f : friction factor

Re : Reynolds number

ρ : density of the working fluid

μ : viscosity

x : dryness fraction

$\dot{m}$: mass flow rate

τ : crankshaft torque

ϵ : error expression used to end the cyclical iteration

Φ : design vector

E_{cycle} : total energy per cycle

$\delta\theta$: size of the angular interval

M_{cycle} : total mass flow per cycle

ω : angular velocity of the rotor

m_1, m_2, m_3: mass of the plunger, the lever, and the inlet valve

k_v, k_{stop}, k_{seat}: stiffness of the valve spring, the mechanical stopper, and the seat

c_{seat}, c_{stop}: damping coefficient of the seat and mechanical stopper

δ_v : valve spring initial deflection

I_2 : moment of inertia of the lever about the pivot point

x_v, y_v, z_v: displacement of the plunger, lever, and valve

$\dot{x}_v, \dot{y}_v, \dot{z}_v$: velocity of the pluger, lever, and valve

$\ddot{z}_v$: acceleration of the valve

F_{sl} : force exerted by the solenoids

F_{sur} : contact force that the valve experiences

V_3 : volume of the antechamber

ΔP : difference in pressure between the inlet and antechamber

A_v : area of the vale that is subjected to the effect of pressure difference

i_{s_i} : solenoid currents

V_{s_i} : solenoid supplied voltage

z_{s_i} : displacements of the plunger relative to the solenoids 1 and 2

References

Climate Council. (2015). Climate change 2015: Growing risks, critical choices. Climate Council of Australia Ltd. Australia: Climate Council of Australia Ltd. https://www.climatecouncil.org.au/uploads/301336ea755b13fc4d6e49568e0141b2.pdf

Department of Industry and Science. (2015). Australian Energy Update. Department of Industry and Science. Canberra: Department of Industry and Science. http://www.industry.gov.au/Office-of-the-Chief-Economist/Publications/Documents/aes/2015-australian-energy-statistics.pdf

Dunn, W., & Shultis, J. (2012). Exploring Monte Carlo methods. Amsterdam: Elsevier/Academic Press.

Fairhurst, C. (1983). Component pressure loss during two-phase flow. International conference on the Physical modelling of multi-phase flow, 1-24.

International Energy Agency. (2015). Key world energy statistics. OECD/International Energy Agency. Paris: International Energy Agency.

IPCC. (2015). Climate change 2014 - Synthesis report. Intergovernmental panel on climate change. Switzerland: Intergovernmental panel on climate change. https://www.ipcc.ch/pdf/assessment-report/ar5/syr/SYR_AR5_FINAL_full_wcover.pdf

Lemmon, E. W., Huber, M. L., & McLinden, M. O. (2010). NIST Reference Fluid Thermodynamic and Transport Properties—REFPROP Version 9.0. Gaithersburg, Maryland 20899: U.S. Department of Commerce - Technology Administration - National Institute of Standards and Technology.

Lemort, V., Quoilin, S., Cuevas, C., & Lebrun, J. (2009). Testing and modeling a scroll expander integrated into an Organic Rankine Cycle. Applied Thermal Engineering, 29(14-15), 3094-3102. doi: 10.1016/j.applthermaleng.2009.04.013

Lund, H., & Flatten, T. (2010). Equilibrium conditions and sound velocities in two-phase flows. SIAM Annual Meeting (AN10). Pittsburgh, Pennsylvania, USA.

Massoud, M. (2005). Engineering thermofluids - Thermodynamics, fluid mechanics and heat transfer. Berlin: Springer.

Mathias, J., Johnston, J., Cao, J., Priedeman, D., & Christensen, R. (2009). Experimental Testing of Gerotor and Scroll Expanders Used in, and Energetic and Exergetic Modeling of, an Organic Rankine Cycle. Journal Of Energy Resources Technology, 131(1), 012201. doi: 10.1115/1.3066345

McNeil, D. (2000). Two-phase flow in orifice plates and valves. Proceedings Of The Institution Of Mechanical Engineers, Part C: Journal Of Mechanical Engineering Science, 214(5), 743-756. doi: 10.1243/0954406001523740

Munson, B., Okiishi, T., Huebsch, W., & Rothmayer, A. (2013). Fundamentals of fluid mechanics. Hoboken, NJ: John Wiley & Sons, Inc.

National Institute of Standards and Technology. (2016, 03 02). Linking REFPROP with other applications. http://www.boulder.nist.gov/div838/theory/refprop/LINKING/Linking.htm#MatLabApplications

Phung, T. H., Sultan, I. A., & Boretti, A. (2016). Design of Limaçon Gas Expanders. In R. N. Jazar, & L. Dai (Eds.), Nonlinear Approaches in Engineering Applications, 91-120. Springer International Publishing Switzerland.

Ryley, D. (1964). Property definition in equilibrium wet steam. International Journal Of Mechanical Sciences, 6(6), 445-454. doi: 10.1016/s0020-7403(64)80005-9

Sultan, I. (2005). The Limaçon of Pascal: Mechanical Generation and Utilization for Fluid Processing. Proceedings Of The Institution Of Mechanical Engineers, Part C: Journal Of Mechanical Engineering Science, 219(8), 813-822. doi: 10.1243/095440605x31698

Sultan, I. (2008). A Geometric Design Model for the Circolimaçon Positive Displacement Machine. Journal Of Mechanical Design, 130(6), 062307. doi: 10.1115/1.2901143

Sultan, I. (2012). Optimum design of limaçon gas expanders based on thermodynamic performance. Applied Thermal Engineering, 39, 188-197. doi: 10.1016/j.applthermaleng.2012.01.039

Sultan, I., & Schaller, C. (2011). Optimum Positioning of Ports in the Limaçon Gas Expanders. Journal Of Engineering For Gas Turbines And Power, 133(10), 103002. doi: 10.1115/1.4003195

Tuymer, W. J., & Machu, E. H. (2001). Compressor valves. In P. C. Hanlon (Ed.), Compressor handbook, 20.1-20.29. New York: McGraw-Hill.

Yuan, Q., & Li, P. Y. (2004). Self-calibration of push-pull solenoid actuators in electrohydraulic valves. 2004 ASME International Mechanical Engineering Congress and RD&D Expo, 269-275. California: ASME. doi:10.1115/IMECE2004-62109

Chapter 5: Conclusions and recommendations for future work

In this thesis, a new embodiment of the limaçon machine has been proposed in Chapter 2. This embodiment is referred to as the limaçon-to-circular machine, which reflects the profiles of the machine rotor and housing, respectively. Prior to this, Sultan (2007; 2008) had introduced the details of the limaçon-to-limaçon and circolimaçon designs, which are the other embodiments of this technology. The limaçon-to-limaçon design requires both the rotor and housing to be manufactured to the limaçon curve. Due to the complexity of the limaçon profile, the machine rotor and housing fabrication process has been subjected to technical challenges. The rotor and the housing of the circolimaçon machine are both manufactured of circular arcs, a feature which presents a sealing challenge due to the fact that the clearance between the rotor apex and the machine housing varies periodically as the machine operates. The limaçon-to-circular design developed in this thesis reduces the complexity present in the fabrication of limaçon rotors, hence reducing the production cost associated with the limaçon-to-limaçon design. At the same time, the proposed design maintains excellent sealing efficiency of the limaçon-to-limaçon design.

The limaçon-to-circular design requires an in-depth geometric modelling in relation to the rotor-housing interference and volumetric characteristics. Two mathematical approaches, tangent based and radial clearance based methods, have been developed and utilised to study the rotor-housing interference challenge. Subsequently, in the Chapter 2, the volumetric characteristics of such a design has been discussed in detail. In addition to that, an optimisation procedure has been employed to calculate the optimum dimensions for the machine based on certain operational requirements. The results obtained in that chapter confirmed the validity of the prosed geometric models and their suitability to

produce embodiments optimised for certain operating constraints and capacity requirements.

The examples presented in Chapters 3 and 4 confirm that the dynamic model developed in Chapter 3 to describe the non-linear multidegree of freedom vibration of the apex seal is useful to investigate the seal behaviour as well as the machine thermal performance. The contact forces between the seal and machine housing and between the seal and seal groove, the spring and damping forces as well as the pressure forces from the upper and lower working chambers exert on the seal surfaces have been taken into account in this seal vibration model. From the developed seal dynamic model, the seal-groove interaction has been categorised into nine different cases based on the type of seal-groove back-contact and front-contact. The cases have been labelled as two-digit numbers in which the first digit represents the type of back-contact and the second digit is the type of front-contact as detailed in section 3.5.4. The results obtained from the seal model highlight the potential for modifying some design characteristics in order to ensure more reliable operation for the machine.

In Chapter 4, the seal performance and its influence on the overall performance of the machine has been examined by incorporating the seal dynamic model presented in Chapter 3 to the limaçon-to-circular machine thermodynamic model. Additionally, the dynamic model of inlet valve, which includes its time response to a reference input voltage has also been developed and incorporated into the machine thermodynamic characterisation model. The effectiveness of the seal and response of the inlet valve have been demonstrated in this chapter.

The work presented in the thesis has been successful in answering research questions in relation to the design and characterisation of the limaçon positive displacement gas expander. However, some new questions have emerged, in the process of demonstrating

the results arrived at in the thesis, and these questions present great opportunities for future research projects. For example, the effect of seal vibration on the surface quality and material selection of both the housing and the seal groove stands out as interesting research project to undertake. Since gas expanders are meant to handle gasses at high temperatures, the manner in which the heat transfers from the rotating chambers via the round housing to surrounding should be investigated in a future research project as well. Another interesting future research project is the manner in which the inlet valve can be used reliably to control the expander performance at variable loads and minimise the amount of working fluid needed to achieve a certain outcome. Also the angular locations of the inlet and discharge ports and the effect of these locations on the machine performance are to be investigated. These are only some examples of future research project which were flagged by the outcome of the thesis.

References

Amrouche, F., Erickson, P., Park, J., & Varnhagen, S. (2014). An experimental investigation of hydrogen-enriched gasoline in a Wankel rotary engine. International Journal Of Hydrogen Energy, 39(16), 8525-8534. doi: 10.1016/j.ijhydene.2014.03.172

Aoun, B. (2008). Micro combined heat and power operating on renewable energy for residential building. Engineering Sciences. École Nationale Supérieuredes Mines de Paris.

Banerjee, S., & Chan, A. (1980). Separated flow models—I. Analysis of the averaged and local instantaneous formulations. International Journal Of Multiphase Flow, 6(1-2), 1-24. doi: 10.1016/0301-9322(80)90036-1

Bowman, J. L. (1983). United States Patent No. 4412796.

Çengel, Y., & Ghajar, A. (2011). Heat and mass transfer – Fundamentals and applications. New York: McGraw-Hill.

Chen, H., Goswami, D., & Stefanakos, E. (2010). A review of thermodynamic cycles and working fluids for the conversion of low-grade heat. Renewable And Sustainable Energy Reviews, 14(9), 3059-3067. doi: 10.1016/j.rser.2010.07.006

Chen, Y., Lundqvist, P., Johansson, A., & Platell, P. (2006). A comparative study of the carbon dioxide transcritical power cycle compared with an organic rankine cycle with R123 as working fluid in waste heat recovery. Applied Thermal Engineering, 26(17-18), 2142-2147. doi: 10.1016/j.applthermaleng.2006.04.009

Cheng, K. (2000). Some Observations on Carnot Cycle as the Genesis of the Heat Pipe and Thermosyphon. International Journal Of Mechanical Engineering Education, 28(1), 69-87. doi: 10.7227/ijmee.28.1.6

Climate Council. (2015). Climate change 2015: Growing risks, critical choices. Climate Council of Australia Ltd. Australia: Climate Council of Australia Ltd. https://www.climatecouncil.org.au/uploads/301336ea755b13fc4d6e49568e0141b2.pdf

Department of Industry and Science. (2015). Australian Energy Update. Department of Industry and Science. Canberra: Department of Industry and Science. http://www.industry.gov.au/Office-of-the-Chief-Economist/Publications/Documents/aes/2015-australian-energy-statistics.pdf

DiPippo, R. (2007). Ideal thermal efficiency for geothermal binary plants. Geothermics, 36(3), 276-285. doi: 10.1016/j.geothermics.2007.03.002

Dunn, W., & Shultis, J. (2012). Exploring Monte Carlo methods. Amsterdam: Elsevier/Academic Press.

Fairhurst, C. (1983). Component pressure loss during two-phase flow. International conference on the Physical modelling of multi-phase flow, 1-24.

Feyens, F. (1931, April 28th). US Patent No. 1802887.

Fischer, J. (2011). Comparison of trilateral cycles and organic Rankine cycles. Energy, 36(10), 6208-6219. doi: 10.1016/j.energy.2011.07.041

Frager, M., & Menard, H. (1954). US Patent No. 3029741.

Fukuta, M., Yanagisawa, T., Higashiyama, M., & Ogi, Y. (2009). Performance of Vane-Type CO2 Expander and Characteristics of Transcritical Expansion Process. HVAC&R Research, 15(4), 711-727. doi: 10.1080/10789669.2009.10390859

Iaccarino, G., Ooi, A., Durbin, P., & Behnia, M. (2003). Reynolds averaged simulation of unsteady separated flow. International Journal Of Heat And Fluid Flow, 24(2), 147-156. doi: 10.1016/s0142-727x(02)00210-2

Gao, H., Liu, C., He, C., Xu, X., Wu, S., & Li, Y. (2012). Performance Analysis and Working Fluid Selection of a Supercritical Organic Rankine Cycle for Low Grade Waste Heat Recovery. Energies, 5(9), 3233-3247. doi: 10.3390/en5093233

Ghosh, S. K., Seshaiah, N., Sahoo, R. K., & Sarangi, S. K. (2005). Designs of turboexpander for cryogenic applications. Indian Journal of Cryogenics.

Glavatskaya, Y., Podevin, P., Lemort, V., Shonda, O., & Descombes, G. (2012). Reciprocating Expander for an Exhaust Heat Recovery Rankine Cycle for a Passenger Car Application. Energies, 5(6), 1751-1765. doi: 10.3390/en5061751

Gridin, V., & Mirkin, A. (1971). Study of operating processes of reciprocating expanders. Chemical And Petroleum Engineering, 7(9), 785-788. doi: 10.1007/bf01143302

Grip, R. L. (2009). A mechanical model of an axial piston machine. Stockholm: Royal Institute of Technology.

Guo, C., Du, X., Yang, L., & Yang, Y. (2015). Organic Rankine cycle for power recovery of exhaust flue gas. Applied Thermal Engineering, 75, 135-144. doi: 10.1016/j.applthermaleng.2014.09.080

Handschuh, R. F., & Owen, A. K. (2010). Analysis of Apex Seal Friction Power Loss in Rotary Engines. NASA Glenn Research Center, Cleveland, Ohio. NASA Technical Memorandum No. 2010-216353.

Hou, Y., Zhu, Z., & Chen, C. (2004). Comparative test on two kinds of new compliant foil bearing for small cryogenic turbo-expander. Cryogenics, 44(1), 69-72. doi: 10.1016/j.cryogenics.2003.08.002

House, P. A. (1976). Helical-rotor expander application for geothermal energy conversion. Livermore, California: Lawrence Livermore Laboratory.

Hung, T., Shai, T., & Wang, S. (1997). A review of organic rankine cycles (ORCs) for the recovery of low-grade waste heat. Energy, 22(7), 661-667. doi: 10.1016/s0360-5442(96)00165-x

International Energy Agency. (2015). Key world energy statistics. OECD/International Energy Agency. Paris: International Energy Agency.

IPCC. (2015). Climate change 2014 - Synthesis report. Intergovernmental panel on climate change. Switzerland: Intergovernmental panel on climate change. https://www.ipcc.ch/pdf/assessment-report/ar5/syr/SYR_AR5_FINAL_full_wcover.pdf

Jia, X., Zhang, B., Pu, L., Guo, B., & Peng, X. (2011). Improved rotary vane expander for trans-critical CO2 cycle by introducing high-pressure gas into the vane slots. International Journal Of Refrigeration, 34(3), 732-741. doi: 10.1016/j.ijrefrig.2010.12.005

Jia, X., Zhang, B., Yang, B., & Peng, X. (2009). Study of a Rotary Vane Expander for the Transcritical CO2 Cycle—Part II: Theoretical Modeling. HVAC&R Research, 15(4), 689-709. doi: 10.1080/10789669.2009.10390858

Kawahara, A., Chung, P., & Kawaji, M. (2002). Investigation of two-phase flow pattern, void fraction and pressure drop in a microchannel. International Journal Of Multiphase Flow, 28(9), 1411-1435. doi: 10.1016/s0301-9322(02)00037-x

Kucerija. (1991). United States Patent No. 5003782.

Lemmon, E. W., Huber, M. L., & McLinden, M. O. (2010). NIST Reference Fluid Thermodynamic and Transport Properties—REFPROP Version 9.0.

Gaithersburg, Maryland 20899: U.S. Department of Commerce - Technology Administration - National Institute of Standards and Technology.

Quoilin, S., Lemort, V., & Lebrun, J. (2010). Experimental study and modeling of an Organic Rankine Cycle using scroll expander. Applied Energy, 87(4), 1260-1268. doi: 10.1016/j.apenergy.2009.06.026

Lemort, V., Quoilin, S., Cuevas, C., & Lebrun, J. (2009). Testing and modeling a scroll expander integrated into an Organic Rankine Cycle. Applied Thermal Engineering, 29(14-15), 3094-3102. doi: 10.1016/j.applthermaleng.2009.04.013

Li, M., Ma, Y., & Tian, H. (2009). A Rolling Piston-Type Two-Phase Expander in the Transcritical CO2 Cycle. HVAC&R Research, 15(4), 729-741. doi: 10.1080/10789669.2009.10390860

Lockhart, R. W., & Martinelli, R. (1949). Proposed correlation of data for isothermal two-phase, two-component flow in pipes. Chemical engineering process, 39-48.

Lund, H., & Flatten, T. (2010). Equilibrium conditions and sound velocities in two-phase flows. SIAM Annual Meeting (AN10). Pittsburgh, Pennsylvania, USA.

Massoud, M. (2005). Engineering thermofluids - Thermodynamics, fluid mechanics and heat transfer. Berlin: Springer.

Mathias, J., Johnston, J., Cao, J., Priedeman, D., & Christensen, R. (2009). Experimental Testing of Gerotor and Scroll Expanders Used in, and Energetic and Exergetic Modeling of, an Organic Rankine Cycle. Journal Of Energy Resources Technology, 131(1), 012201. doi: 10.1115/1.3066345

Mazda Motor Corporation. (2014, July 15). What is the Rotary Engine? Retrieved from www.mazda.com: http://www.mazda.com/stories/rotary/about/

McClure, A. W. (1950). United States Patent No. 2529880.

McNeil, D. (2000). Two-phase flow in orifice plates and valves. Proceedings Of The Institution Of Mechanical Engineers, Part C: Journal Of Mechanical Engineering Science, 214(5), 743-756. doi: 10.1243/0954406001523740

McQuillan, K., & Whalley, P. (1985). Flow patterns in vertical two-phase flow. International Journal Of Multiphase Flow, 11(2), 161-175. doi: 10.1016/0301-9322(85)90043-6

Munson, B. R., Rothmayer, A. P., Okiishi, T. H., & Huebsch, W. W. (2013). Fundamentals of fluid mechanics 7th edition. USA: Wiley.

National Institute of Standards and Technology. (2016, 03 02). Linking REFPROP with other applications. Retrieved 03 02, 2016, from http://www.nist.gov/: http://www.boulder.nist.gov/div838/theory/refprop/LINKING/Linking.htm#MatLabApplications

Pennock, G., & Beard, J. (1997). Force analysis of the apex seals in the wankel rotary compressor including the influence of fluctuations in the crankshaft speed. Mechanism And Machine Theory, 32(3), 349-361. doi: 10.1016/s0094-114x(96)00051-1

Persson, J., & Sohlenius, G. (1990). Performance Evaluation of Fluid Machinery During Conceptual Design. CIRP Annals, 39(1), 137-140. doi: 10.1016/s0007-8506(07)61020-8

Peterson, R., Wang, H., & Herron, T. (2008). Performance of a small-scale regenerative Rankine power cycle employing a scroll expander. Proceedings Of The Institution Of Mechanical Engineers, Part A: Journal Of Power And Energy, 222(3), 271-282. doi: 10.1243/09576509jpe546

Phung, T. H., & Sultan, I. A. (2017). Apex seal vibration analysis of limaçon positive displacement machines. 9th Australian Congress on Applied Mechanics (ACAM9), 595-603. Sydney: Engineers Australia, 2017. https://search.informit.com.au/documentSummary;dn=394117366088909;res=IELENG. ISBN: 9781925627022

Phung, T., Sultan, I., & Boretti, A. (2016). Design of Limaçon Gas Expanders. In R. N. Jazar & L. Dai (Eds.), Nonlinear Approaches in Engineering Applications: Advanced Analysis of Vehicle Related Technologies (pp. 91-119). Cham: Springer International Publishing.

Picard, M., Tian, T., & Nishino, T. (2015). Predicting Gas Leakage in the Rotary Engine—Part I: Apex and Corner Seals. Journal Of Engineering For Gas Turbines And Power, 138(6), 062503. doi: 10.1115/1.4031873

Picard, M., Tian, T., & Nishino, T. (2015). Predicting Gas Leakage in the Rotary Engine—Part II: Side Seals and Summary. Journal Of Engineering For Gas Turbines And Power, 138(6), 062504. doi: 10.1115/1.4031874

Planche, B. R. (1920, May 18th). US Patent No. 1340625.

Qiu, G., Liu, H., & Riffat, S. (2011). Expanders for micro-CHP systems with organic Rankine cycle. Applied Thermal Engineering, 31(16), 3301-3307. doi: 10.1016/j.applthermaleng.2011.06.008

Quoilin, S., Aumann, R., Grill, A., Schuster, A., Lemort, V., & Spliethoff, H. (2011). Dynamic modeling and optimal control strategy of waste heat recovery Organic Rankine Cycles. Applied Energy, 88(6), 2183-2190. doi: 10.1016/j.apenergy.2011.01.015

Rose, S., & Yang, D. (2014). Wide and multiple apex seals for the rotary engine. Mechanism And Machine Theory, 74, 202-215. doi: 10.1016/j.mechmachtheory.2013.12.011

Ryley, D. (1964). Property definition in equilibrium wet steam. International Journal Of Mechanical Sciences, 6(6), 445-454. doi: 10.1016/s0020-7403(64)80005-9

Shin, B., Iwata, Y., & Ikohagi, T. (2003). Numerical simulation of unsteady cavitating flows using a homogenous equilibrium model. Computational Mechanics, 30(5-6), 388-395. doi: 10.1007/s00466-003-0414-7

Smith, I. (1993). Development of the Trilateral Flash Cycle System: Part 1: Fundamental Considerations. Proceedings Of The Institution Of Mechanical Engineers, Part A: Journal Of Power And Energy, 207(3), 179-194. doi: 10.1243/pime_proc_1993_207_032_02

Smith, I. K., Stosic, N., & Kovacevic, A. (2005). Screw expanders increase output and decrease the cost of geothermal binary power plant systems. Transactions of Geothermal Resource Council, 25-28.

Steffen, M., Löffler, M., & Schaber, K. (2013). Efficiency of a new Triangle Cycle with flash evaporation in a piston engine. Energy, 57, 295-307. doi: 10.1016/j.energy.2012.11.054

Subiantoro, A., & Ooi, K. (2010). Design analysis of the novel Revolving Vane expander in a transcritical carbon dioxide refrigeration system. International Journal Of Refrigeration, 33(4), 675-685. doi: 10.1016/j.ijrefrig.2009.12.023

Subiantoro, A., & Tiow, O. (2009). Introduction of the Revolving Vane Expander. HVAC&R Research, 15(4), 801-816. doi: 10.1080/10789669.2009.10390865

Sultan, I. (2005). The Limaçon of Pascal: Mechanical Generation and Utilization for Fluid Processing. Proceedings Of The Institution Of Mechanical Engineers, Part C: Journal Of Mechanical Engineering Science, 219(8), 813-822. doi: 10.1243/095440605x31698

Sultan, I. (2008). Inverse geometric design for a class of rotary positive displacement machines. Inverse Problems In Science And Engineering, 16(2), 127-139. doi: 10.1080/17415970601162164

Sultan, I. (2007). A surrogate model for interference prevention in the limaçon-to-limaçon machines. Engineering Computations, 24(5), 437-449. doi: 10.1108/02644400710755852

Sultan, I. (2008). A Geometric Design Model for the Circolimaçon Positive Displacement Machine. Journal Of Mechanical Design, 130(6), 062307. doi: 10.1115/1.2901143

Sultan, I., & Schaller, C. (2011). Optimum Positioning of Ports in the Limaçon Gas Expanders. Journal Of Engineering For Gas Turbines And Power, 133(10), 103002. doi: 10.1115/1.4003195

Sun, F., Chen, W., Chen, L., & Wu, C. (1997). Optimal performance of an endoreversible Carnot heat pump. Energy Conversion And Management, 38(14), 1439-1443. doi: 10.1016/s0196-8904(96)00013-1

Sultan, I. (2012). Optimum design of limaçon gas expanders based on thermodynamic performance. Applied Thermal Engineering, 39, 188-197. doi: 10.1016/j.applthermaleng.2012.01.039

Tamura, I., Taniguchi, H., Sasaki, H., Yoshida, R., Sekiguchi, I., & Yokogawa, M. (1997). An analytical investigation of high-temperature heat pump system with

screw compressor and screw expander for power recovery. Energy Conversion And Management, 38(10-13), 1007-1013. doi: 10.1016/s0196-8904(96)00130-6

F. Tchanche, B., Pétrissans, M., & Papadakis, G. (2014). Heat resources and organic Rankine cycle machines. Renewable And Sustainable Energy Reviews, 39, 1185-1199. doi: 10.1016/j.rser.2014.07.139

Tuymer, W. J., & Machu, E. H. (2001). Compressor valves. In P. C. Hanlon (Ed.), Compressor handbook, 20.1-20.29. New York: McGraw-Hill.

Ozone Secretariat (1987). The Montreal Protocol on Substances that Deplete the Ozone Layer. United Nation Environment Programme. http://ozone.unep.org/new_site/en/Treaties/treaties_decisions-hb.php?sec_id=342&show_all

Wang, H., Peterson, R., & Herron, T. (2009). Experimental performance of a compliant scroll expander for an organic Rankine cycle. Proceedings Of The Institution Of Mechanical Engineers, Part A: Journal Of Power And Energy, 223(7), 863-872. doi: 10.1243/09576509jpe741

Wang, H., Peterson, R., Harada, K., Miller, E., Ingram-Goble, R., & Fisher, L. et al. (2011). Performance of a combined organic Rankine cycle and vapor compression cycle for heat activated cooling. Energy, 36(1), 447-458. doi: 10.1016/j.energy.2010.10.020

Wang, W., Wu, Y., Ma, C., Liu, L., & Yu, J. (2011). Preliminary experimental study of single screw expander prototype. Applied Thermal Engineering, 31(17-18), 3684-3688. doi: 10.1016/j.applthermaleng.2011.01.019

Wang, Z., Wang, C., & Chen, K. (2001). Two-phase flow and transport in the air cathode of proton exchange membrane fuel cells. Journal Of Power Sources, 94(1), 40-50. doi: 10.1016/s0378-7753(00)00662-5

Warren, S., & Yang, D. (2013). Design of rotary engines from the apex seal profile (Abbr.: Rotary engine design by apex seal). Mechanism And Machine Theory, 64, 200-209. doi: 10.1016/j.mechmachtheory.2013.01.015

Wheildon, W. M. (1896, January 14th). United States Patent No. 553086.

Xiaojun, G., Liansheng, L., Yuanyang, Z., & Pengcheng, S. (2004). Research on a Scroll Expander Used for Recovering Work in a Fuel Cell. International Journal of Thermodynamics, 7(1), 1-8.

Yang, B., Peng, X., Sun, S., Guo, B., & Xing, Z. (2009). Study of a Rotary Vane Expander for the Transcritical CO2 Cycle—Part I: Experimental Investigation. HVAC&R Research, 15(4), 673-688. doi: 10.1080/10789669.2009.10390857

Yuan, Q., & Li, P. Y. (2004). Self-calibration of push-pull solenoid actuators in electrohydraulic valves. 2004 ASME International Mechanical Engineering Congress and RD&D Expo, 1-7. California: ASME.

Zamfirescu, C., & Dincer, I. (2008). Thermodynamic analysis of a novel ammonia–water trilateral Rankine cycle. Thermochimica Acta, 477(1-2), 7-15. doi: 10.1016/j.tca.2008.08.002

Zhang, B., Peng, X., He, Z., Xing, Z., & Shu, P. (2007). Development of a double acting free piston expander for power recovery in transcritical CO2 cycle. Applied Thermal Engineering, 27(8-9), 1629-1636. doi: 10.1016/j.applthermaleng.2006.05.034

Zhang, Y., Zuo, Z., Yuan, C., & Wang, D. (2014). Analysis on Performance of Leaf Spring Rotary Engine. Energy Procedia, 61, 984-989. doi: 10.1016/j.egypro.2014.11.1009

Zheng, N., Zhao, L., Wang, X., & Tan, Y. (2013). Experimental verification of a rolling-piston expander that applied for low-temperature Organic Rankine Cycle. Applied Energy, 112, 1265-1274. doi: 10.1016/j.apenergy.2012.12.030